Using ATLAS to Investigate the Associated Production of a Higgs Boson with a Pair of Top Quarks

Lily Asquith

Department of Physics and Astronomy

University College London

A thesis submitted for the degree of

Doctor of Philosophy

22nd December 2009

I confirm that the work presented in this thesis is my own. Where information has been derived from other sources, I confirm that this has been indicated in the thesis.

Lily Asquith

Abstract

This thesis describes the study of the channel $\mathrm{t\bar{t}H^0(H^0 \to b\bar{b})}$ with the ATLAS detector with $30\mathrm{fb}^{-1}$ of data and a center of mass energy of 10 TeV.

Chapter 1 provides a description of the ATLAS detector, followed by a theoretical background in **Chapter 2** and a discussion of phenomenology and event generation in **Chapter 3**. Issues associated with leptons and missing energy are presented in **Chapter 4**, with focus on optimising the preselection cuts to reduce the rate of background processes, including those previously unconsidered for this channel but found to be important as a consequence of this study. In addition, the reconstruction of the leptonically decaying W Boson from lepton and missing energy is described. The treatment of jets is introduced in **Chapter 5**, with the focus being again on the optimisation of preselection cuts. Studies presented here are on corrections for energy lost via both muons and neutrinos in semi-leptonic b-decays and preselection cuts based on the transverse momenta and b-weights of individual jets. The issues associated with combinatorial background and the use of jet charge to reduce it is also introduced here. The choice of jet algorithm is considered of great importance for this channel, thus is presented in detail in **Chapter 6**. **Chapter 7** explores the reconstruction of the Higgs Boson from jet pairs, focusing on the segregation of jets by b-weight. The reconstruction of the $\mathrm{t\bar{t}H^0}$ system is studied with various techniques; an investigation of the use of jet charge to discriminate between b and $\mathrm{b\bar{b}}$ jets is presented as a novel likelihood variable.**Chapter 8** summarises the results obtained using the optimised preselection, jet algorithm and jet charge method. Systematic uncertainties are discussed throughout the thesis where relevant and also summarised.

This thesis is dedicated to my daughter Jessie.

Contents

List of Figures

List of Tables

Introduction

The Large Hadron Collider (LHC) at CERN is the largest particle accelerator ever built. It is currently due to start up in November 2009 at a center of mass energy of up to 7 TeV, increasing to the design center of mass energy of 14 TeV over the subsequent months and years.

The experiment was built with a list of primary goals in mind, one of which is to determine the origin of mass in the universe. One of the current popular candidates for the acquisition of mass by fundamental particles is the process of spontaneous symmetry breaking, governed by a massive scalar particle known as the Higgs Boson.

The Higgs Boson is the only undiscovered particle predicted by the Standard Model of particle physics, and it is with the LHC that we plan to find it, if it exists. Although we have not directly observed the Higgs Boson, we can constrain its properties based on the properties of the other particles in the electroweak sector, principally those of the W and Z Bosons and top quark, which have been measured to high precision at LEP, SLC and the Tevatron.

These measurements suggest that the Higgs Boson is most likely (at 95% C.L.) to have a mass in the range 115-150 GeV, which onfortunately is the most difficult mass range in which to find it. Production of a Higgs in this mass range is dominated by gluon-gluon fusion. The dominant decay is to a pair of b-jets.

This search must be conducted in the context of large backgrounds particularly from QCD processes which dominate at a hadron collider such as the LHC. It is clear that finding such a particle will not be easy.

One of the proposals of the ATLAS Technical Design Report [2] of 1999 was to look for the low mass Higgs when produced in association with a pair of top quarks. It was found that the cross section for this process was quite high, and has the benefit of having a high $\mathrm{p_T}$ lepton in the final state if one considers the case when one of the top quarks decays to a b-quark and a leptonically-decaying W Boson. The presence of one high $\mathrm{p_T}$ lepton makes the event triggerable, an absolutely vital requirement considering the extremely high rate at which we expect to collect with the ATLAS detector.

This thesis presents work undertaken on optimising the event selection procedure for the channel $\mathrm{t\bar{t}H^0(H^0 \to b\bar{b})}$ with an integrated luminosity of 30$\mathrm{fb^{-1}}$ and a center of mass energy of 10 TeV.

Chapter 1

Design and reach of the ATLAS detector

The Large Hadron Collider (LHC) has been constructed within the existing tunnel which housed the Large Electron Positron (LEP) experiment until its closure in November 2000. It has been under construction for more than 14 years, and will be the largest and highest energy collider ever built. The LHC is a circular accelerator, capable of colliding either protons or lead ions. For the majority of the accelerator's lifetime it will collide protons.

At startup the LHC is expected to operate with a center of mass energy ($\sqrt{s}$) of 7 TeV and luminosty ($\mathcal{L}$) of $10^{31}\mathrm{cm}^{-2}\mathrm{s}^{-1}$. It is expected that $200\mathrm{pb}^{-1}$ of data will be gathered at this energy. Thereafter the energy will be increased to $\sqrt{s} = 10$ TeV. At the end of 2010 the LHC will be shut down for the winter while work is done to move the machine towards operating at its nominal $\sqrt{s} = 14$ TeV and $\mathcal{L} = 10^{34}\mathrm{cm}^{-2}\mathrm{s}^{-1}$.

1.1 The Accelerator

Prior to their injection into the LHC, protons are accelerated in four stages (Fig. 1.1):

1. The first stage in the acceleration is linear. **Linac II** strips the electrons from hydrogen atoms to produce protons, which are then linearly accelerated to

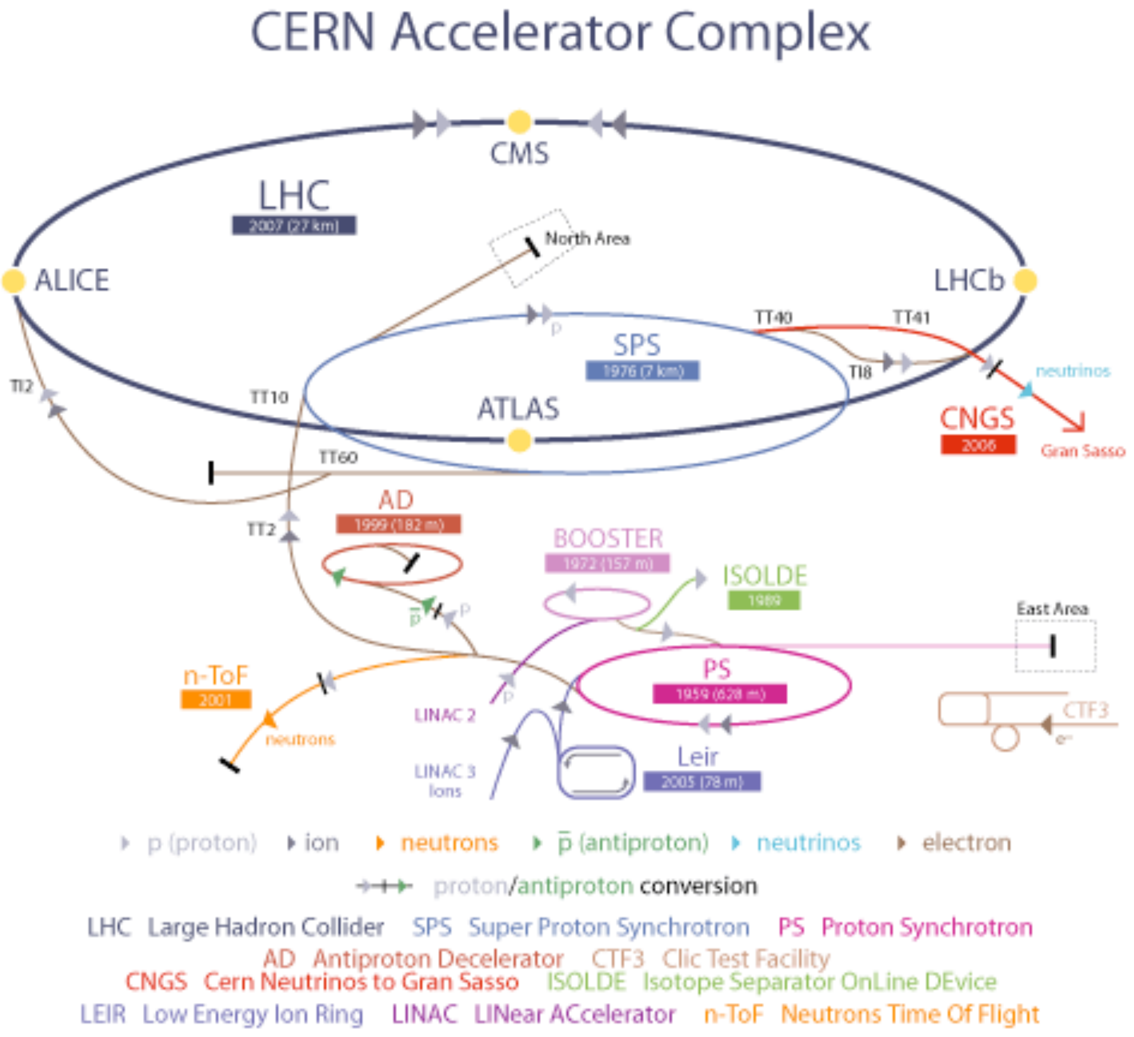

Figure 1.1: The CERN accelerator complex.

approximately one third the speed of light, $\frac{c}{3}$.

2. The protons are then injected into the **booster**. The protons are divided into 4 bunches and circularly accelerated via the use of a pulsing electric field. The booster is 157 m in circumference. It accelerates the protons to $0.916c$.

3. The third stage of acceleration is the **Proton Synchrotron** (PS), a 628 m circumference circular accelerator which increases the protons' speed to $0.999c$ in 1.2 seconds.

4. The final stage of acceleration before injection into the LHC is the **Super Proton Synchrotron** (SPS), which accelerates 25 GeV protons to 450 GeV. The SPS is 7 km in circumference.

After the packets of protons have been accelerated to 450 GeV they are injected into the LHC. The injection of 2808 packets takes around half an hour, then the beams are further accelerated up to 7 TeV per beam. The beams are forced to circulate within two vacuum beampipes, with one beam going clockwise and the other going anti-clockwise. They are bent around the LHC using superconducting magnets operating with a current of 12,000 A. The key specifications of the LHC are shown in Table. 1.1.

When the beams of protons reach the required center-of-mass energy, their paths are crossed at four points around the ring at which the detectors are positioned. The largest LHC detector is ATLAS, a multi-purpose detector, described in Sec. 1.2. The other multi-purpose detector is the Compact Muon Solenoid (CMS), which differs from ATLAS in several aspects of its design, described in detail in[3]. The two specialised detectors are ALICE and LHCb. The ALICE (A Large Ion Collider Experiment) detector will examine the collisions of lead ions in order to gain insight into the properties of the quark-gluon plasma that is believed to have filled the universe moments after the Big Bang. The LHCb (Large Hadron Collider beauty) detector has been designed specifically to examine the decays of b quarks and their antiparticles, with an aim of understanding the asymmetry between matter and anti-matter in the universe.

Particles collided	**Protons**
Circumference	**26,659 m**
Injected beam energy	**450 GeV**
Nominal beam energy	**7 TeV**
Nominal magnetic field	**8.33 T**
Operating temperature	**1.9 K**
Revolution frequency	**11.2455 kHz**
Power consumption	**120 MW**

Table 1.1: Technical specifications of the LHC.

The event rate, n, for any given process at the LHC is a function of the machine luminosity ($\mathcal{L}$) and the cross-section (σ) for that process, $n = \sigma\mathcal{L}$. The cross-sections for all processes are dependent on the center of mass energy ($\sqrt{s}$) of the collision. The luminosity of the machine is dependent on various beam parameters as set out in Eq. 1.1, and described in detail elsewhere[4]. The beam parameters are N: the number of protons per bunch (1.15×10^{11}), t: the time between bunch crossings (25 ns), A_T: the transverse bunch area at the interaction points ($15\mu\text{m}^2$) and f: the fraction of bunches containing protons (~ 0.8).

$$\mathcal{L} = \frac{1}{4\pi}\frac{N^2 f}{tA_T} \tag{1.1}$$

1.2 Design of the Atlas Detector

The ATLAS detector is generally described in terms of the co-ordinate system (η,ϕ). The pseudorapidity (η) is chosen as a close approximation to the rapidity, Y, given by Y$=\tanh^{-1}\beta$, where β is the speed of the particle divided by the

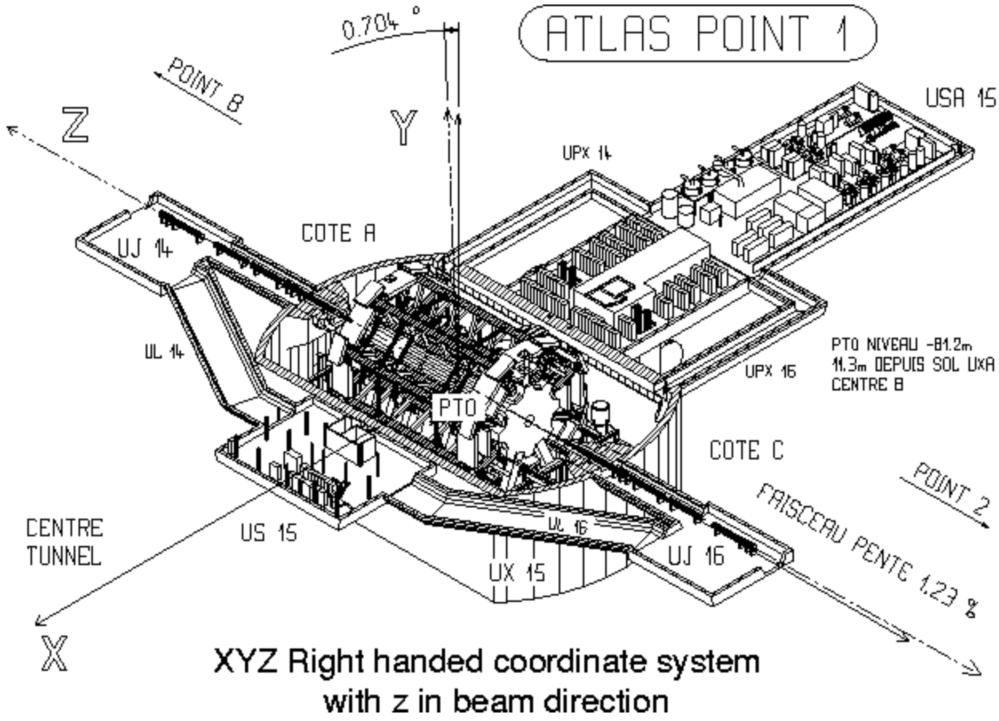

Figure 1.2: The ATLAS co-ordinate system.

speed of light. The relation between η and the polar angle θ is $\eta = -\ln\tan\frac{\theta}{2}$. The azimuthal angle ($\phi$) is measured in the $x-y$ plane.

1.2.1 Inner detector

The inner detector is designed for tracking charged particles with high precision in a very busy environment. At design luminosity, ~1000 charged particles will traverse the tracking detector every 25ns. The ATLAS inner detector comprises three sub-detectors: the pixel detector, the Semi Conductor Tracker (SCT) and the Transition Radiation Tracker (TRT). The barrel section of the inner detector is shown in Fig. 1.3.

Both the pixel and SCT sub-detectors are made from silicon, which has the desirable properties of low ionisation energy (electron-hole pairs are created easily), long absorption length (incident particles are not easily stopped), high mobility (high drift velocity for constant electric field) and low Z (proton num-

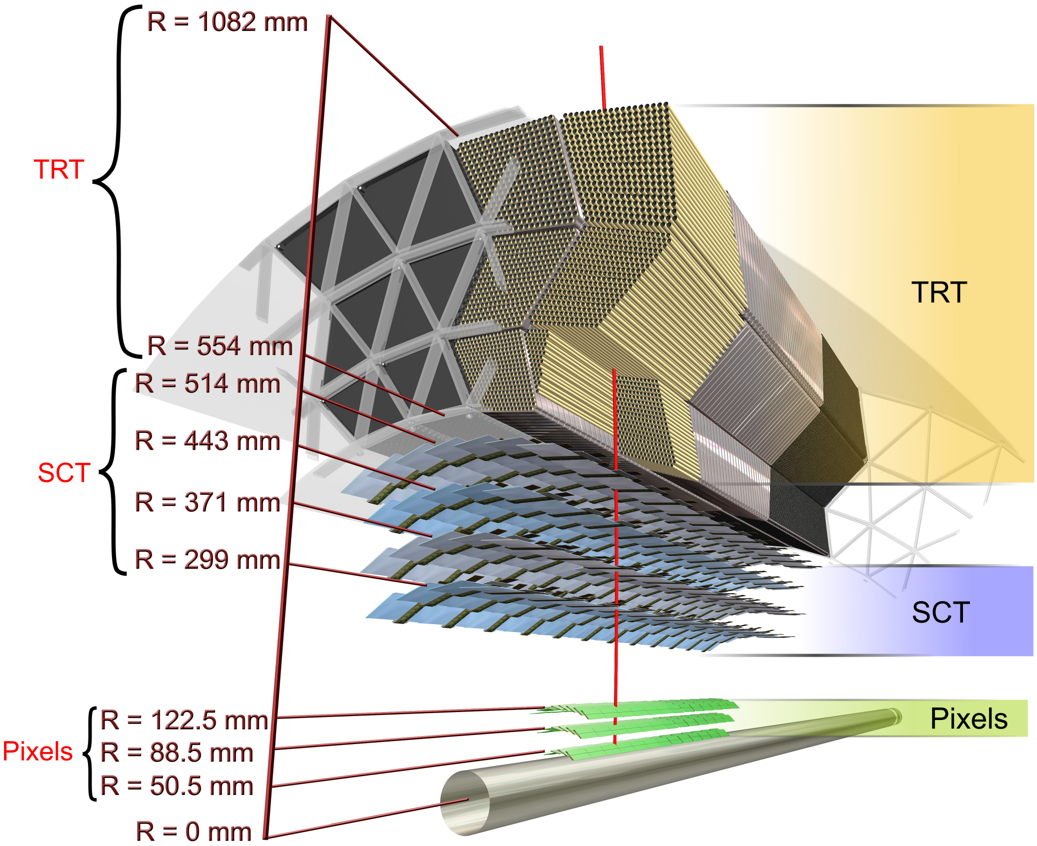

Figure 1.3: The ATLAS inner detector.

Track parameter	$0.25 < \|\eta\| < 0.5$	$1.50 < \|\eta\| < 1.75$
Inverse transverse momentum ($\frac{q}{p_T}$)	$0.34\mathrm{TeV}^{-}1$	$0.41\mathrm{TeV}^{-}1$
Azimuthal angle (ϕ)	72 μ rad	90 μ rad
Polar angle ($\cot\theta$)	0.7×10^{-3}	1.2×10^{-3}
Transverse impact parameter (d_0)	10 μm	12 μm
Longitudinal impact parameter ($z_0 \sin\theta$)	91 μm	71 μm

Table 1.2: Inner detector resolutions.

ber). The combination of these properties means that incident particles can usually traverse the pixel and SCT detectors without being stopped, but will leave maximum evidence of their traversal in the form of 'hits'. The energy lost by charged particles and photons in the inner detector material is understood and is corrected offline. The pixel detector is particularly important for identifying the decays of short-lived particles such as B-hadrons, due to its close proximity to the beam pipe. The innermost pixel layer is known as the b-layer for this reason. The pixels provide excellent vertexing with a spatial resolution of around 10 (115) μm in the transverse (longitudinal) directions. In comparison, the SCT spatial resolutions are 17 (580) μm.

Outside the pixel and SCT detectors is the TRT, which makes use of the radiation emitted by charged particles as they pass through the detector. The emission of radiation is due to the change in dielectric constant between the layers of polypropylene foil and gas. The photons emitted by the charged particles as they traverse the foil are absorbed by the gas mixture inside the 370,000 drift tubes of the TRT. The TRT has a spatial resolution of ~ 130 μm and can be used for discriminating between electrons and pions based on the rate of their photon emission. The spatial and transverse momentum resolutions for tracking parameters using the inner detector as a whole are given in Table. 1.2. The impact parameter is defined as the distance between the interaction point and the point at which the track is at its closest to this point.

1.2.2 Magnet systems

The ATLAS detector incorporates two separate magnet systems, the solenoid and the toroid. These magnet systems are essential for making momentum measurements of charged particles in the inner detector and muon chambers respectively.

The solenoid surrounds the inner detector and creates a magnetic field of 2 T. It is 5.3 m in length and has a diameter of 2.4 m. The field inside the inner detector causes charged particles to move in curved trajectories in the x-y plane, thus enabling their $\mathrm{p_T}$ to be calculated via Eq. 1.2, where $\mathrm{p_T}$ is transverse momentum (transverse to direction of field), q is the particle's charge, R is the radius of curvature of the track, B is the strength of the magnetic field.

$$\mathrm{p_T} = \mathrm{qRB} \tag{1.2}$$

The toroidal air-core magnets are located within the muon system, providing a magnetic field of 4.7 T and cause a deflection of the muon tracks allowing a momentum measurement.

1.2.3 Calorimetry

The design and performance of the calorimeters are described in detail in[1], [3]. Two calorimeters are used for measuring energy deposits in the ATLAS detector. Both the ATLAS calorimeters are non-compensating, meaning that the response to hadrons is lower than that to electromagnetically interacting particles.

The electromagnetic calorimeter (ECAL) is positioned outside the solenoid and shares the same vacuum casing, thus reducing the amount of material traversed by a particle entering the calorimeters. It is a sampling calorimeter made from layers of lead (the absorber) and liquid Argon (the sampler). The ECAL is divided into three parts; the barrel section covering the region $|\eta| < 1.5$ and the two endcaps covering $1.4 \leq |\eta| \leq 3.2$. The granularity in η, ϕ in the main ECAL is $\Delta\eta = 0.025$ and $\Delta\phi = 0.025$ in both the barrel and endcaps. The energy resolution is $\frac{\sigma_E}{E} = \frac{10\%}{\sqrt{E}} + 0.2\%$ in the barrel and $\frac{\sigma_E}{E} = \frac{12\%}{\sqrt{E}} + 0.35\%$ in the endcaps.

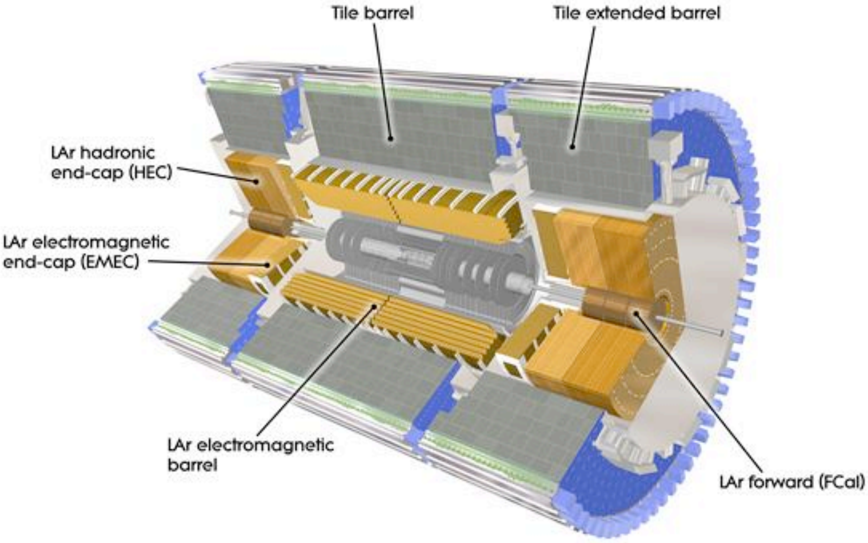

Figure 1.4: The ATLAS calorimeters

The hadronic calorimeter (HCAL) comprises three sections. The tile calorimeter is a sampling calorimeter comprising layers of steel (the absorber) and scintillating plastic (the sampler). The hadrnic LAr calorimeter covers the range $1.5 < \eta < 3.2$ and the LAr forward calorimeter (FCAL) covers the range $3.1 < \eta < 4.9$. The granularity in η, ϕ ranges from $(0.1, 0.1)$ to $(0.2, 0.2)$. The wide coverage in η is essential for a good measurement of the missing energy in the detector, $\not{E}_{\mathrm{T}}$.

1.2.4 Muon chambers

Muons with energy below $O(500)$ GeV lose energy almost entirely through ionisation rather than by bremsstrahlung, which is the case for electrons of comparable energy. The muon detectors are positioned outside the calorimeters, making it unlikely that particle other than muons will be incident upon them.

There are four separate muon sub-detectors, as can be seen in Fig. 1.5. The Cathode Strip Chambers (CSC) and Monitored Drift Tubes (MDT) are precision detectors while the Resistive Plate Chambers (RPC) and Thin Gap Chambers

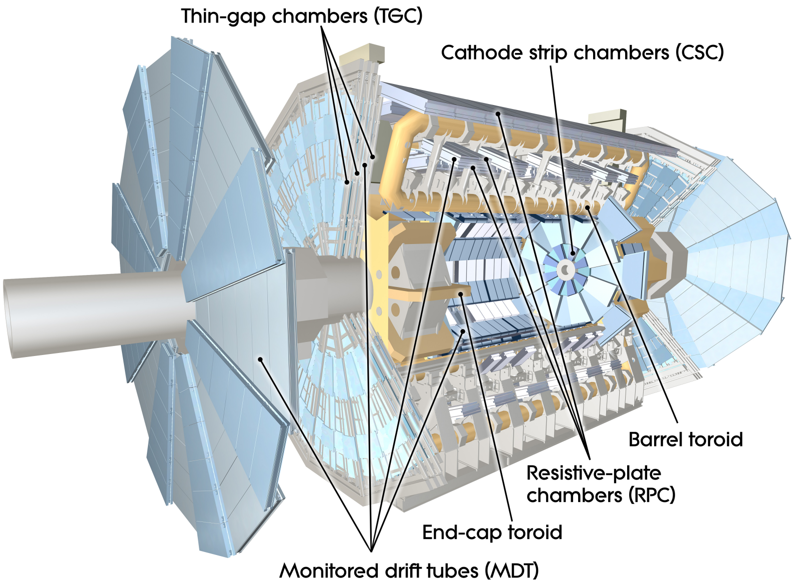

Figure 1.5: The muon chambers.

(TGC) are used for triggering in the barrel and endcap regions respectively.

The spatial and time resolutions of the muon sub-detectors are given in Table. 1.2.4. The triggering detectors have an excellent time resolution while the precision detectors have a good spatial resolution, used for precise reconstruction of the muons' trajectories and momenta.

Sub-detector	**Z**	ϕ	Time
MDT	$35\mu m$	–	–
CSC	$40\mu m$	5mm	7ns
RPC	10mm	10mm	1.5ns
TGC	$2-6$mm	37mm	4ns

Table 1.3: Muon detector resolutions.

1.3 The Trigger and Data Acquisition

The beam crossing rate at the LHC is 40 MHz, such that the ATLAS detector will see the products of up to 10^9 collisions per second. The event rate that can be stored offline for analysis is $\sim$ 200 Hz, meaning that the trigger system must allow an average of just one event in every 200,000 to be accepted when the LHC is operating at full luminosity. In order to satisfy these demands with optimal efficiency the ATLAS trigger is implemented in three stages or levels. The first level (L1) is a hardware-based trigger and levels two (L2) and three (the Event Filter or EF) are collectively known as the High Level Trigger or HLT, and are software-based triggers.

Hardware Trigger: The L1 trigger uses coarse granularity calorimeter and muon chamber information. The latency at L1 is 2.5 μs. The L1 trigger must reduce the rate from 40 MHz to a maximum of 75 kHz and it utilises all data from the calorimeter and muon systems.

Software Trigger The L2 trigger has an average processing time of 40 ms and must reduce the rate to 2 kHz. The L2 trigger only uses information from certain areas of the detector known as Regions of Interest (RoI). These are defined by L1. Using RoI means that approximately 1-4 % of the data is examined. The EF has

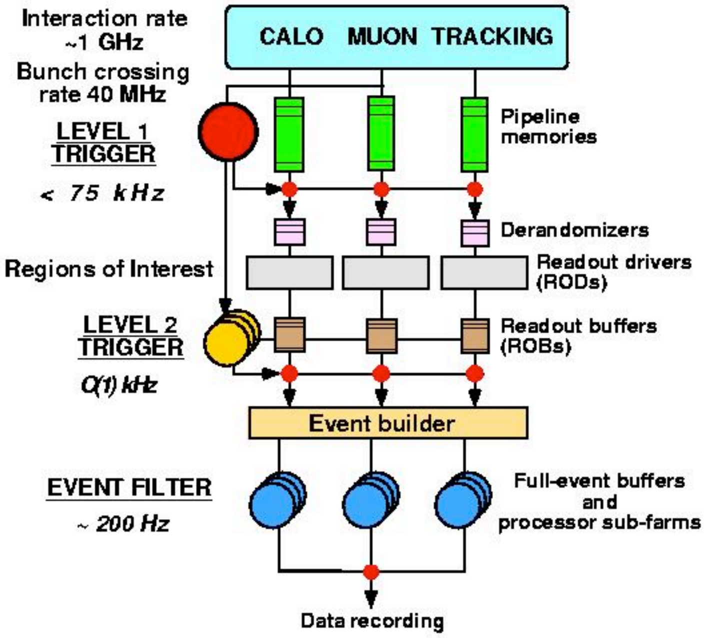

Figure 1.6: Schematic diagram of the ATLAS trigger system.

an execution time of $\sim$1 s, thus making it possible to use offline reconstruction algorithms. The full offline reconstruction is performed on the complete event.

Prescales are applied at each trigger level to reduce the number of events passing a certain trigger, and so reduce the dead time. A schematic of the ATLAS trigger system is shown in Fig. 1.6.

Chapter 2

The Standard Model Higgs Boson

The Standard Model (SM) of particle physics is the model which best describes the observed interactions of fundamental particles. All of the fundamental particles and forces shown in Fig. 2.1 can be successfully described by Quantum Field Theories (QFT), with the notable exception being gravity, which is not included in the current Standard Model.

Although field theories have existed for a long time in descriptions of classical mechanics, the first QFT developed was that of Quantum Electrodynamics (QED). Field theory was needed in order to unify the two great innovations of the twentieth century, quantum mechanics and special relativity.

In quantum mechanics the uncertainty principle states that energy can fluctuate by an amount ΔE over a very short period of time Δt given by $\Delta E \Delta t \geq \frac{\hbar}{2}$. According to special relativity, energy and mass are equivalent. Combining these two theories provides us with a mechanism by which massive particles can be created for a short time out of 'nothing', i.e. the vacuum.

The discovery of the quantisation of light by Max Planck in 1900 led physicists to understand that the electromagnetic field had associated quanta, photons, which could then be described as particles as well as electromagnetic waves.

Electrons differ from photons in several ways. They are charged, they are massive, and they have spin $\frac{1}{2}$. The half integer spin of an electron puts it into a class of particles known as fermions, which is made up of all the fundamental particles which obey Fermi-Dirac statistics, hence the name fermions. As can be seen in Fig. 2.1, the fermions comprise all the matter particles in the Standard

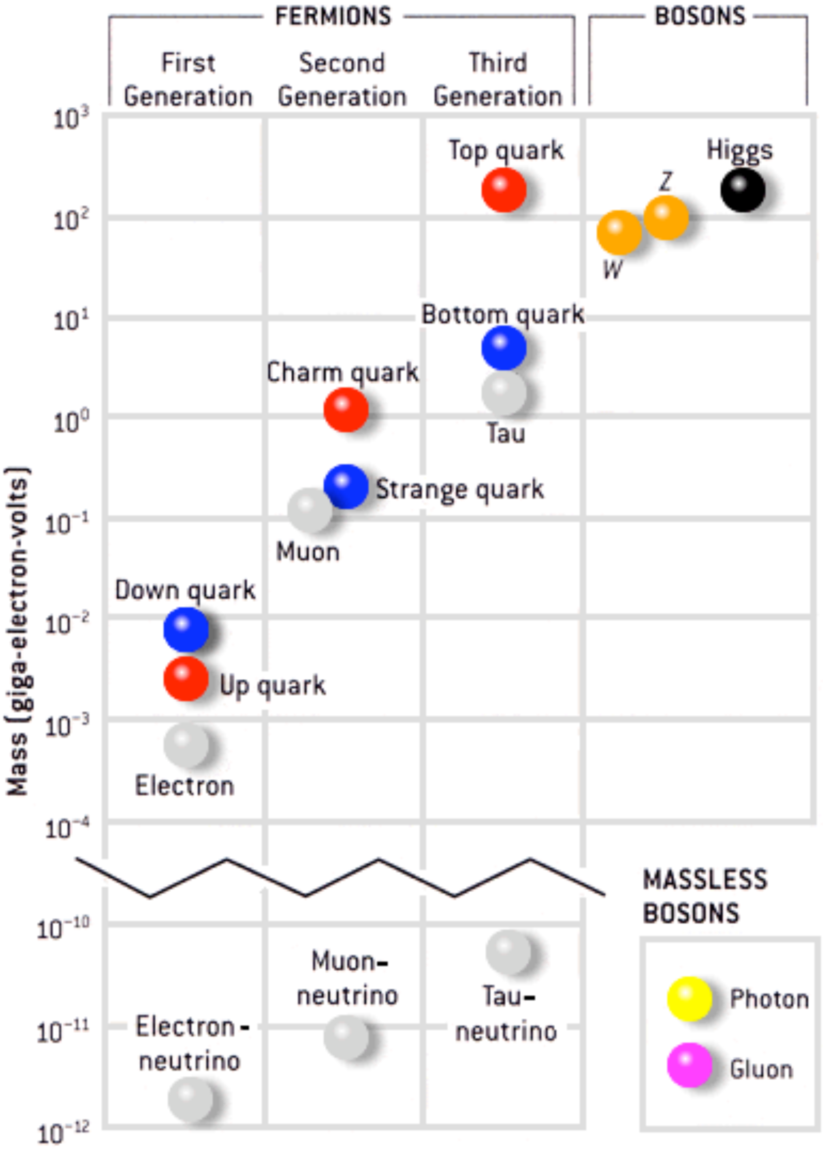

Figure 2.1: The standard model.

Model. Photons are, on the other hand, without any charge or mass, and have a spin of 1. The integer spin of the photon places it in the other class of particles, Bosons, as it obeys Bose-Einstein statistics.

The electron and photon do, however, have one important feature in common. They are both assumed to be fundamental particles, meaning that they have no deeper structure; they are made of nothing but themselves down to a scale of $\sim 10^{-19}$ m. So the acceptance that photons could be described as quantisations of a field inevitably led to the idea that electrons may also be explained in such a way.

2.1 Symmetry

The proof by Emmy Noether in 1915 that every symmetry has an associated conserved quantity made it imperative that any formalism claiming to describe the nature of fundamental particles must possess such a symmetry and give the same result wherever or whenever one chooses to test it. The Lagrangians we formulate to describe the dynamics of fundamental particles must, therefore, be shown to describe *gauge fields*; fields that have such properties of causality and locality that enable one to calculate them at any point in space-time without altering the results. There is a problem with this requirement for symmetry, in that it is not what we observe in the real world. We observe three distinct forces with different strengths. Hadrons and leptons interact differently. The carriers of the weak force (weak vector bosons) and residual strong force (pions) are massive, hence their ranges are finite. Reconciling these observed non-symmetries with the desire for an underlying theoretical symmetry requires some process by which the symmetry can be broken spontaneously, i.e. without the application of some external field. The Lagrangian can then be symmetric, but its ground state solution can be non-symmetric, corresponding to the observations made regarding the non-symmetric world in which we live.

The theory of Quantum Electro Dynamics (QED) successfully incorporated gauge invariance into the field theory describing electromagnetic interactions by replacing the quantum mechanical momentum operator ∂^μ

Term	Definition
ψ	The particle wavefunction.
γ^μ	The Dirac Gamma matrices, $\mu = 1, 2, 3, 4$.
∂_μ	The QM momentum operators, $\mu = 1, 2, 3, 4$.
m	The particle mass.
q	The particle charge.
A_μ	The electromagnetic vector field.

Table 2.1: Definitions of the terms in the Lagraingian for QED.

with the covariant derivative $\mathcal{D}^\mu = \partial^\mu + iqA^\mu$. The Lagrangian of QED is $\mathcal{L} = \bar{\psi}(i\gamma^\mu\partial_\mu - m)\psi - q\bar{\psi}\gamma^\mu\psi A_\mu$, which described the interaction of the fermion (ψ) with the electromagnetic field (A_μ), and results in:

1. A description of the electron which is locally gauge invariant under the transformation $\psi(x) \rightarrow e^{-iq\theta(x)}\psi(x)$.
2. An independent quantum mechanical confirmation of the classical Maxwell equations.

The terms in the Lagrangian of QED are described in Table. 2.1.

The vector fields A_μ in QED are massless, corresponding to the physical observation of the massless photon. The weak interaction, however, is known to be mediated by massive vector fields, as the observed weak interactions of fermions are of very short range. The presence of a massive A_μ field would introduce an additional mass term to the QED Lagrangian, violating gauge invariance.

2.2 The Higgs mechanism

For a complex scalar field $\phi = \frac{1}{\sqrt{2}}(\phi_1 + i\phi_2)$, one can write the gauge invariant Lagrangian as Eq. 2.1, where the constant coefficient of the mass term, μ^2 is real

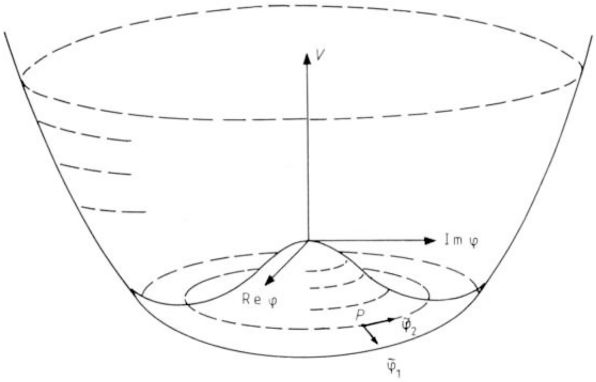

Figure 2.2: The potential V(ϕ) of a complex scalar field $\phi(x)$.

and the constant coefficient of the interaction term λ is both real and positive. The term containing $F_{\mu\nu} = \partial_\mu A_\nu - \partial_\nu A_\mu$ is the kinetic term of the electromagnetic field A_μ.

$$\mathcal{L} = -\frac{1}{4}F_{\mu\nu}F^{\mu\nu} + D_\mu\phi^* D_\mu\phi - \left(\mu^2\phi^2 + \lambda(\phi)^4\right) \tag{2.1}$$

The potential V(ϕ) $= \mu^2\phi^2 + \lambda(\phi)^4$ has a minimum when the field $\phi(x) = \sqrt{\frac{-\mu^2}{2\lambda}}$. Providing μ^2 is positive, the potential V(ϕ) is minimised to zero when the field $\phi = 0$. However, there is no requirement that μ^2 be positive. A negative value of μ^2 results in V(ϕ) being maximised to zero when $\phi = 0$, and the minimum value of the potential corresponds to non-zero ϕ. This non-zero value of the field is known as the vacuum expectation value $\phi(V_{min}) = \frac{v}{\sqrt{2}} = \sqrt{\frac{-\mu^2}{2\lambda}}$. The complex scalar field potential is illustrated in Fig. 2.2.

As the potential is completely symmetric about $\phi = 0$, all points on the circle defined by $\phi = \frac{v}{\sqrt{2}}$ are equivalent. Choosing the point $\phi_1 = \frac{v}{\sqrt{2}}$, $\phi_2 = 0$, one can then expand ϕ around its minimum by adding a real field, $h(x)$ to the expectation value v.

Expanding the field about this minimum $\phi(x) = \frac{v+h(x)}{\sqrt{2}}$ and exploiting the phase symmetry with the substitutions $\rho(x) = \phi(x)e^{-i\theta(x)}$ and $B_\mu = A_\mu - \frac{\partial_\mu\theta}{e}$ one can write the Lagrangian as Eq. 2.2.

$$\begin{aligned}\mathcal{L} = -\frac{1}{4}F_{\mu\nu}F^{\mu\nu} + \frac{1}{2}(ev)^2 B_\mu^2 + e^2 vhB_\mu^2 + \frac{1}{2}e^2h^2B_\mu^2 \\ + \frac{1}{2}(\partial h)^2 - \mu^2 h^2 - \sqrt{\lambda}\mu h^3 - \frac{\lambda}{4}h^4 + \frac{\mu^4}{4\lambda} \qquad (2.2)\end{aligned}$$

The complex scalar field doublet ϕ and massless gauge Boson A^μ in Eq. 2.1 have been replaced by a real scalar field, h, and the gauge Boson A^μ has acquired mass via the second term, $\frac{1}{2}(ev)^2B_\mu^2$.

Eq. 2.2 is just Eq. 2.1 written in terms of the ground state of the field. Expressing the field in terms of its ground state via the addition of the real scalar field h results in the spontaneous breaking (or hiding) of the symmetry in the Lagrangian; one starts out with a perfectly symmetric Lagrangian, finds its ground state, perturbs it a little bit and ends up with something that looks like it might describe the physical world. This way of allowing the symmetry to hide itself is known as the Higgs mechanism.

The third and fourth terms in Eq. 2.2 are interaction terms with hB_μ^2 and $h^2B_\mu^2$. These terms can be measured experimentally. They describe the coupling of the Higgs field h to the vector gauge bosons B_μ.

The vacuum expectation value, v, is determined by the mass of the gauge Boson, and this value also occurs in the mass term for the Higgs, $-\mu^2h^2 = -\lambda v^2h^2$. The λ parameter, however, is a parameter associated purely with the scalar field, and thus cannot be known without knowledge of the scalar field itself. This means that the Higgs mass cannot be predicted from theory and must be measured experimentally.

The Higgs mechanism for this U(1) theory can be extended to the electroweak SU(2)x U(1) case if one considers exactly the same procedure for three weak gauge Bosons W^a. We then replace $-\frac{1}{4}F_{\mu\nu}F^{\mu\nu}$ with $-\frac{1}{4}W^a_{\mu\nu}W_a^{\mu\nu} - \frac{1}{4}A_{\mu\nu}A^{\mu\nu}$ to describe the interaction of three weak gauge bosons W^a with the single electromagnetic gauge boson A and each other.

This results in a physical-world, broken-symmetry Lagrangian similar to Eq. 2.2 but with a single, physical massless vector boson corresponding to the photon, and three physical, massive vector bosons. At the time this theory was formulated, the three massive vector Bosons had not been observed. They were not confirmed experimentally until the Super Proton Synchrotron (SPS) experiment in 1983 at CERN. The confirmation of the existence of these weak vector bosons gave great weight to the Higgs mechanism, and left only one remaining Standard model particle to be discovered, the Higgs boson. The vacuum expectation value ν has been determined from the measurement of the masses of the W and Z bosons to be 246 GeV.

The addition of an interaction term between the complex scalar doublet of fields $\phi = \begin{pmatrix} \phi^\dagger \\ \phi^0 \end{pmatrix}$ and a lepton field doublet $\psi^{\mathrm{lep}} = \begin{pmatrix} \psi_{\nu_l} \\ \psi_l \end{pmatrix}$ will account for the generation of lepton masses providing the term is renormalizable and invariant under SU(2)× U(1) gauge transformations. The interaction term that satisfies this requirement is the Yukawa interaction given by $\mathcal{L}_y = -G_l[\bar{\psi}^l_R \phi^\dagger \psi^l_L] + [\bar{\psi}^l_L \phi \psi^l_R]$ where ψ_{R}, ψ_{L} correspond to right-handed and left-handed fermion fields respectively.

Substituting the unitary gauge form of ϕ into $\mathcal{L}_y$ results in

1. a mass term $\frac{G_l \nu}{\sqrt{2}} \bar{l} l$ such that $m_l = \frac{G_l \nu}{\sqrt{2}}$
2. a coupling term between the Higgs and the electron $\frac{G_l}{\sqrt{2}} \bar{l} h l$ such that the coupling between Higgs and lepton fields is proportional to the mass of the lepton.

Quark masses are generated by Yukawa couplings to the Higgs field in a similar way as the leptons, such that the masses of all the fermions can be generated by this mechanism. The Higgs mechanism does not provide any insight into the mass values of the fermions, as the coupling parameters it introduces are arbitrary. The top quark Yukawa coupling is considered particularly interesting, as $G_{top} = \sqrt{2} \frac{m_{top}}{\nu} \approx 1$.

2.3 Expected properties of a Standard Model Higgs boson

As mentioned in Sec. 2.2, it is not possible to make an exact prediction regarding the mass of the Higgs Boson from theory, as the mass term for the Higgs is determined in part by a parameter λ whose value is associated only with the

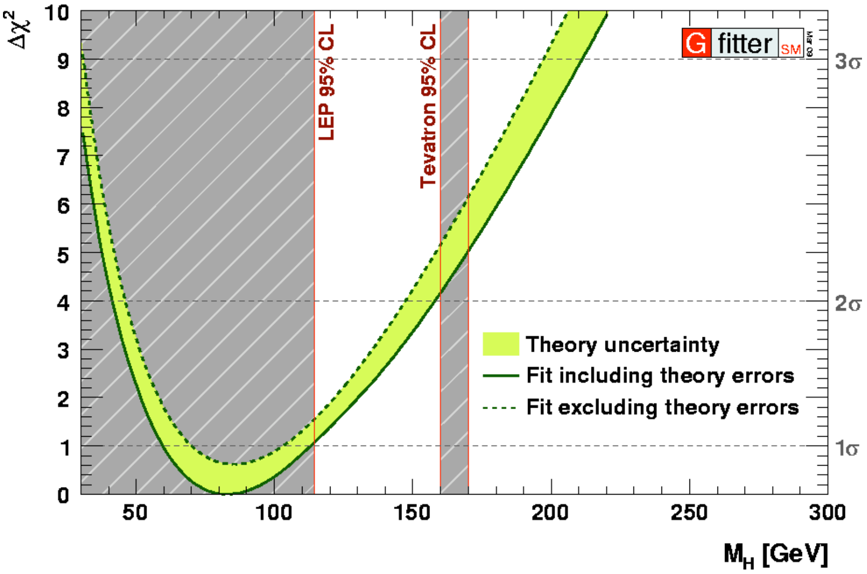

Figure 2.3: The χ^2 probability based on electroweak prescision measurements as a function of Higgs mass[6].

Higgs field. This means that the mass of the Higgs Boson is determined by the Higgs Field.

We are not completely in the dark, however. The masses of the weak vector Bosons and top quark have now been measured to extremely high precision, enabling the contributions to their masses from loops involving Higgs Bosons to be determined. These measurements are combined with other precision measurements such as the widths of the gauge Bosons and the weak mixing angle, $\sin\theta_W$. Collectively these measurements are known as the electroweak precision data,[5] and they are used as parameters in a χ^2 fit to determine the probability of the Higgs existing at a certain mass. The current best fit from this data is shown in Fig. 2.3. The shaded regions of Fig. 2.3 are excluded due to direct searches for the Higgs Boson, with the large region ≤ 114 GeV having been excluded with 95% confidence by the LEP experiment and the thin band at ~ 160 GeV being excluded more recently by the Tevatron experiments[6]. The Tevatron results are shown in more detail in Fig. 2.4. The combined electroweak precision and experimental exclusion data from LEP and Tevatron favour a low mass Higgs Boson in the region 114-154 GeV.

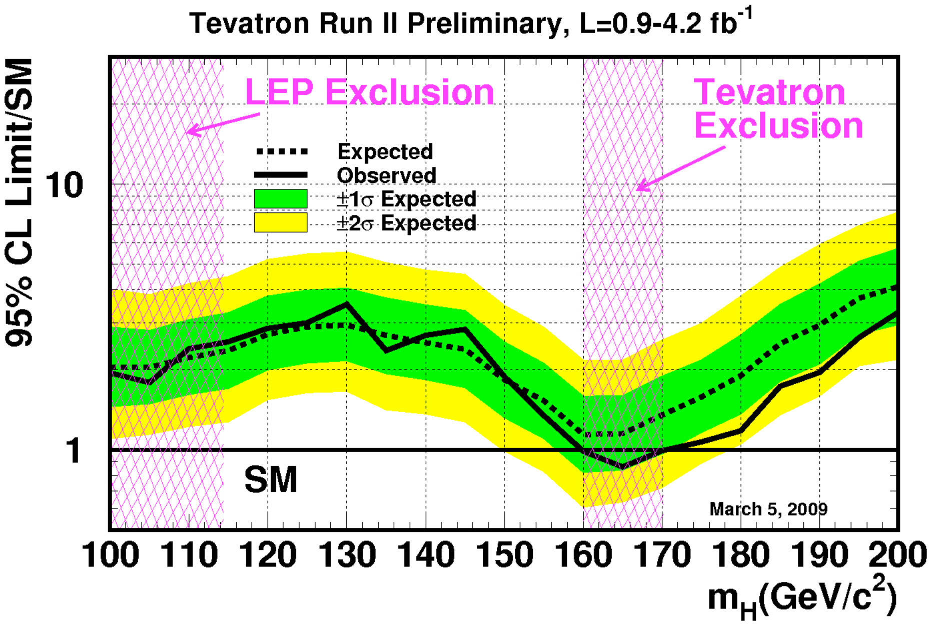

Figure 2.4: Higgs mass exclusion at 95% confidence level, from the combined results of all Tevatron Higgs searches [6].

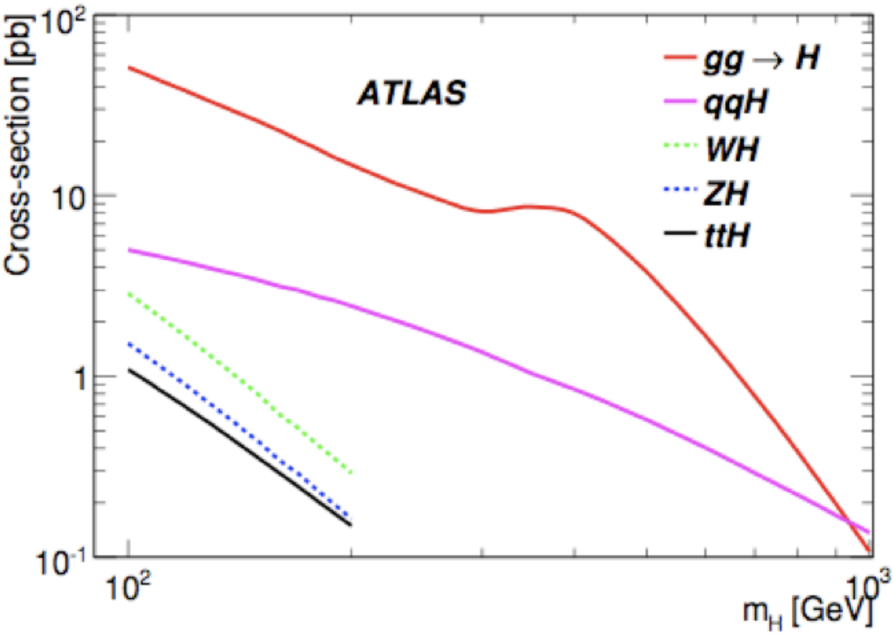

Figure 2.5: Production cross sections for a SM Higgs Boson at the LHC with $\sqrt{s} = 14$TeV[1]

Within the Standard Model, the Higgs coupling to Gauge Bosons and fermions (Yukawa couplings) are strongly dependent on the Higgs mass. This means that the production and decay modes of the Higgs are usually considered as a function of the Higgs mass, as in Fig. 2.5 and Fig. 2.6.

For $M_H \leq 130$ GeV the Higgs decays predominantly to a $\mathrm{b\bar{b}}$ pair. At higher masses the decays to W^+W^- and $\tau^+\tau^-$ become dominant. There are different challenges associated with each production/decay mode. For the currently favoured low-mass region, the Higgs is most likely to decay to a $\mathrm{b\bar{b}}$ pair, which makes it extremely challenging to find at a hadron collider.

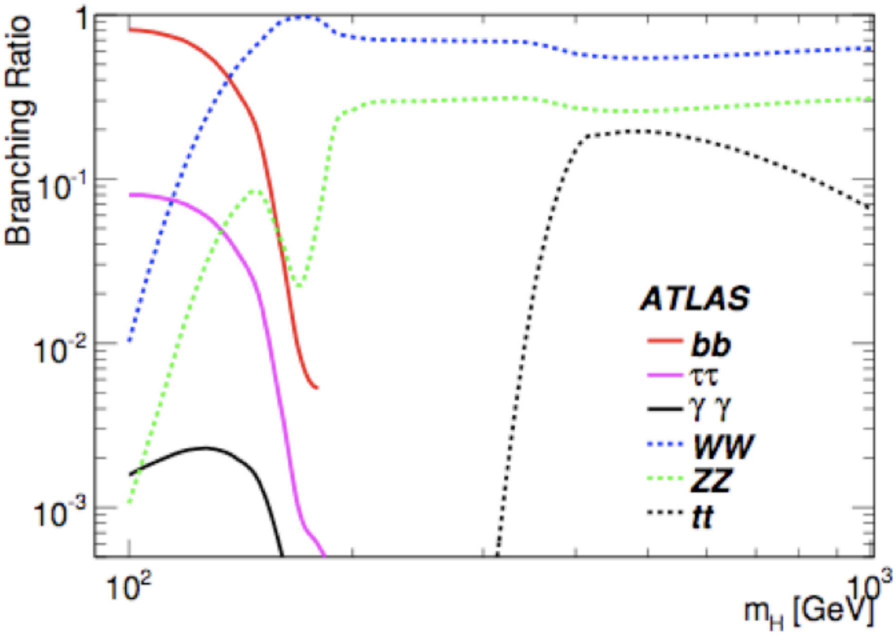

Figure 2.6: Branching ratios for a SM Higgs Boson at the LHC as a function of the Higgs mass, $\mathrm{m_H}$[1]

Chapter 3

Event Generation and Phenomenology

At the time of writing, the LHC has not yet seen any collisions. The analysis presented in this thesis is therefore based entirely on simulated data. Simulated data is produced via a chain of necessary approximations relating to the structure of the proton and the mechanism via which the particles produced in a collision will transform into measurable quantities. These processes are described briefly below and in much greater detail elsewhere [7], [8]. In addition is a summary of the steps taken to generate the data samples used in this analysis.

3.1 The proton

Parton Distribution Functions (PDFs) describe the structure of the proton in terms of its parton content. To calculate a cross-section one must determine the probability of an interaction occurring. The hard scatter may occur via a $\mathrm{q\bar{q}}$, gg or gq interaction. To calculate the probability of any such interaction one must know the fraction of the proton's momentum (x) carried by the partons involved, and also the momentum transfer (Q) between the incoming and outgoing partons. The PDF $f_i^a(x, Q^2)$ parameterises the probability of finding a parton i with a fraction x of the beam energy when the beam particle a is probed by a hard scattering of virtuality Q^2.

PDFs are currently determined from fits to experimental data and are subject to uncertainty. Because the LHC will collide protons at much higher center-of-mass energies than any previous experiment, we are extending the kinematic range in x and Q to the point where the uncertainty on the PDFs may be one of the largest sytematics some analyses will have to deal with. Various measurements will be made with early data at ATLAS in order to constrain the PDFs; the PDFs for sea-quarks can be constrained by examining the invariant mass distribution of Drell-Yan lepton pairs and the rapidity distribution of the Z boson. Measurements of the standard model W boson and $\gamma +$ jet events will be used to improve the gluon PDFs.[9]. The uncertainty on a cross-section due to the PDF is usually given as a measure of the difference between values obtained with different PDF sets.

3.2 Collision kinematics

There are a number of different ways in which two beam protons can scatter off one another at the LHC. As the total center of mass energy of the protons increases, the number of parton constituents increases, such that the total momentum fraction carried by each parton will decrease. A consequence of this is that in the very high energy collisions such as those that we will see at the LHC, a large fraction ($\gtrsim 20\%$) of collisions will be **elastic**, leaving the protons intact. The collisions we are interested in for this study are those of the inelastic, non-diffractive type, as is expected to be the case in $\gtrsim 50\%$ of collisions.

An inelastic collision is expected to produce some interesting events, along with a lot of less interesting debris. Fig. 3.1 shows a visual representation of an inelastic collision at the LHC. The interesting part (in terms of the production of particles such as the Higgs boson) is known as the hard process. This is accompanied by the underlying event in the form of initial state radiation from the incoming protons, final state radiation from the debris, multiple interactions ocurring when there are either multiple hard processes or if there are collisions between inital/final state radiation and partons. Pile-up is an issue because of the extremely high rate at which the collisions take place; left over debris from

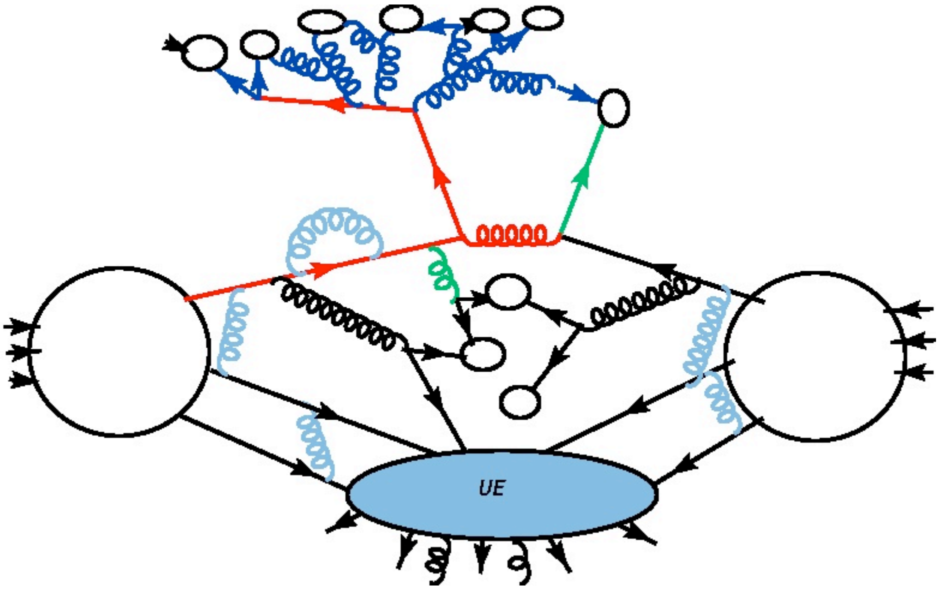

Figure 3.1: An inelastic, non-diffractive collision. The hard process is shown in red. The white blobs represent color-neutral hadrons. The green parton lines represent radiation emitted from the partons involved in the hard process that do not have time to be re-absorbed before the scatter takes place. The dark blue parton lines represent final state radiation before the clustering into color neutral hadrons. The pale blue lines are virtual gluons, holding the proton together. The black gluon lines are initial state radiation that becomes involved in the scatter, thus forming hadrons rather than being reabsorbed.

a previous collision is a real possibility, particularly at high luminosity. All of these contributions must be considered when modelling an ATLAS event. The kinematics of collisions are described in detail in [10].

3.3 Cross-section calculations

Cross-sections for the hard processes are in principle calculable from theory using matrix elements (ME) and Feynman rules, and cross-sections for most of the interesting processes expected at the LHC have been calculated at least to leading order (LO). It is known that the cross-sections for many of the interesting hard processes, particularly in the Higgs sector, are rather dependent on the order at which they are calculated. The general trend is that leading order cross-sections are increased by a k-factor when moving to higher order (NLO, NNLO) calculations. This k-factor generally takes values between 1 and 2; the k-factor for $\mathrm{t\bar{t}H^0}$ is ~ 1.25 when moving from LO to NLO. Most of the generators used for the ATLAS experiment use leading order matrix elements, leaving any correction to the physics analysis end of the process.

Monte Carlo generators allow several other parameters to be varied by the user when generating events. The most important ones to consider are those which have a large effect on either the size of the cross-section or the kinematics of the final state. The generator parameters considered here are the scale Q^2 of the hard process, the mass m_t of the top quark and the available kinematic range (in η and $\mathrm{p_T}$) for the outgoing partons in the hard process. Many other parameters can be set in the different generators, which are described in the manuals for Pythia[11], Alpgen[12], AcerMC[13], Herwig[14] and Jimmy[15]. All five of these generators are utilised at some stage in the making of the samples used in this analysis.

3.3.1 Choice of Q^2 scale in event generation

It has been found [16], [13] that the cross-sections for particular processes with high jet multiplicities, including $\mathrm{t\bar{t}H^0}$, $\mathrm{t\bar{t}b\bar{b}}$ and $\mathrm{t\bar{t}X}$, that the choice of the scale Q^2 used to generate the event has a very large effect on the size of the cross-section obtained. It is common for the same Q^2 scale to be used for the factorisation and renormalisation cut-off scales in the calculation. The full cross-section of any process is completely independent of the scale chosen but the approximations one uses on the way to an all-orders calculation can be strongly dependent on the scale chosen. A sensible choice of Q^2 when generating events to LO is therefore of great importance. The value of Q^2 should reflect the energy scale of the physical final state, and is generally chosen to be around half the transverse mass of the final state, for example Eq. 3.1 in the case of a $\mathrm{t\bar{t}H^0}$ event.

$$Q^2 = \frac{1}{2} \sum_{i=ttH} m_i^2 + p_{Ti}^2 \tag{3.1}$$

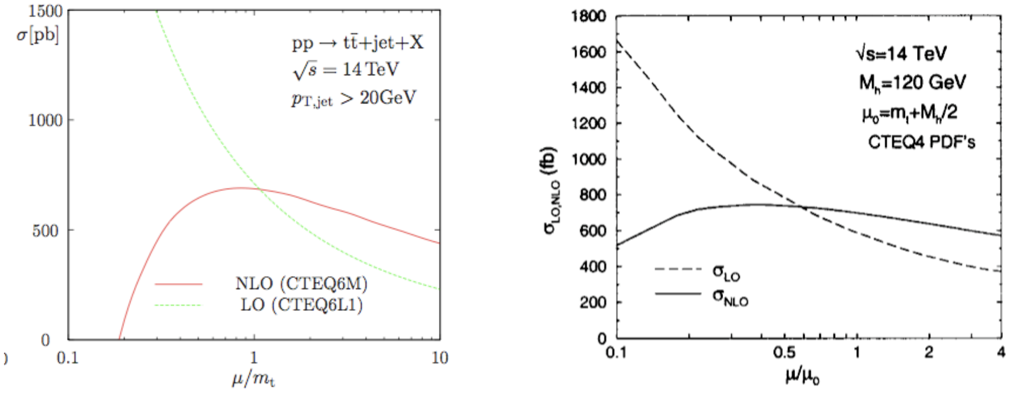

(a)

(b)

Figure 3.2: The running of σ_{LO} and σ_{NLO} with Q^2 for (a) the $\mathrm{t}\bar{t}$+ jets process [8] and for (b) the $\mathrm{t\bar{t}H^0}$ process [16].

The reason for halving the transverse mass is an empirical one; it is noticed that lower values of Q^2 result in a LO cross-section that is closer in magnitude to that obtained at higher orders. This is illustrated in Fig. 3.2(a) for $\mathrm{t\bar{t}X}$ and in Fig. 3.2(b) for $\mathrm{t\bar{t}H^0}$.

3.3.2 Top quark mass

The mass of the top quark is also known to have an effect on the size of the cross-section of processes involving top production. One can see from Fig. 3.3 that passing the generator a top mass of 172.5 GeV will result in a $\mathrm{t}\bar{t}$ cross-section $\sim 10\%$ higher than if the generator is given a top mass of 175 GeV. All the samples used in this analysis are generated with $m_t = 172.5$. This is consistent with the current world average of 173.1±1.3 GeV[17].

3.3.3 Phase space for hard process

The phase space is limited by the generator in that the outgoing partons from the hard process are confined to be within a certain range in η and $\mathrm{p_T}$. The default values in Pythia are to make no kinematic cuts. In Alpgen the default is to have $|\eta| \leq 5$ for the outgoing hard partons. In order to avoid generating large numbers

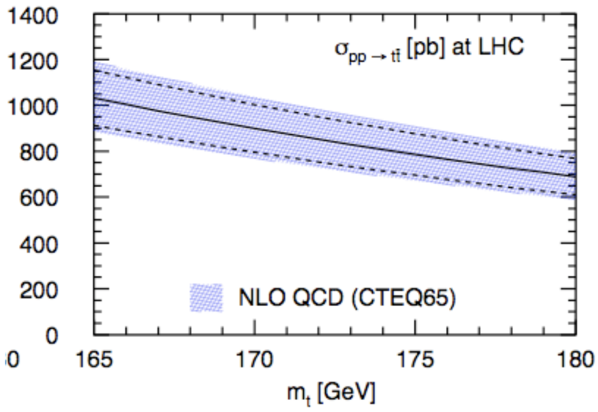

Figure 3.3: Variation of the $t\bar{t}$ cross-section with mass of the top quark[8]. The shaded blue band is the PDF uncertainty. The upper and lower dashed lines correspond to varying Q between half and twice the mass of the top.

of events that will not get past even the preliminary stages of preselection, it is common to apply filters at the generator level. All of the background samples used in this analysis have been generated with the TTbarPlusJets filter described in Sec. 3.5. The $\mathrm{t\bar{t}H^0}$ signal was generated with the lepton filter, which simply requires at least one lepton with $\mathrm{p_T} \geq 10$ GeV and $|\eta| \leq 2.7$.

All samples include only events where one top decays to bjj and the other decays to b$e\nu_e$ or b$\mu\nu_{mu}$. This is implemented at generator level in the $\mathrm{t\bar{t}H^0}$ and $\mathrm{t\bar{t}b\bar{b}(ew)}$ samples. The $\mathrm{t\bar{t}b\bar{b}(qcd)}$ sample was generated to contain all decays, including those where both tops decay to bjj. This is discussed in Sec. 4.4. Descriptions of the samples $\mathrm{t\bar{t}b\bar{b}(ew)}$ and $\mathrm{t\bar{t}b\bar{b}(qcd)}$ referred to here are given in Sec. 3.5.

3.3.4 Parton Showering

Quarks and gluons are colored, thus radiate gluons when accelerated. The gluons that are radiated will also then radiate themselves, producing a cascade of color charge, or a parton shower.[18]. Generally, the evolution of the parton shower is parameterised by some scale which is representative of the *hardness* of the process. There are two ways in which a generator can take the ME for the hard process and turn it into something which will become physically observable. In the event generator Pythia[11], which is used for the generation of the signal sample in this analysis, the parton shower is done by the generator. Another generator, used for the production of the background sample in this analyis, is AlpGen. AlpGen just produces the ME, leaving the complex task of parton showering to an external generator such as Herwig which is used in this analysis. Herwig generates the parton shower directly and the Herwig partons are then matched back to the hard process produced by AlpGen. The matching procedure is described in [19]. Much work has been done on validating these generators with respect to one another and with respect to Tevatron data for example [20], [21].

3.3.5 Hadronisation

Although the process of hadronisation is not well understood, some choice of hadronisation model must be used to confine generated partons into observable hadrons. Two popular models for this are the Lund string model[11] and the cluster modell[14]. Both implement the color confinement introduced by the presence of gluon self-interaction in QCD events.

The Lund string model describes the hadronisation of a light $\mathrm{q\bar{q}}$ pair by the presence of a 'string' between them. As the $\mathrm{q\bar{q}}$ move apart from one another the string increases in length and remains at constant tension, absorbing the kinetic energy of the quarks into potential energy at a rate of ~ 1 GeV fm^{-1}. Eventually the kinetic energy of the $\mathrm{q\bar{q}}$ approaches zero and the process is reversed, with the $\mathrm{q\bar{q}}$ moving together in space while eating up the potential energy in the string. The strong chromomagnetic field within the string means that the probability of pulling further $\mathrm{q\bar{q}}$ pairs out of the vacuum in the region between the original $\mathrm{q\bar{q}}$ pair is constant and non-zero. When this happens the string between the new $\mathrm{q\bar{q}}$ is oppositely polarised and thus cancels out the chromomagnetic field. The string model has been a very successful model for hadronisation based on fits to e^+e^- data, but is complex, having one free parameter per hadron.

The cluster model[14] describes hadronisation following the structure of the parton shower and using the fact that 'perturbative' quarks remember their direction to some extent. Color-singlet pairs are followed through the shower and any loose ends are decayed into $q\bar{q}$ pairs. These color singlets are then assumed to form clusters which decay to pairs of hadrons. There is some difficulty with this model when the clusters are very massive, which may result in inadequate suppression of heavy flavour and baryon production.

3.4 Underlying event and pileup

At design luminosity there will be bunch crossings every 25 ns. For every bunch crossing the number of minimum bias events will be ∼23 on average, although the number of interactions per bunch crossing will follow a Poisson distribution, meaning that there will often be many more than 23 interactions.

An interesting ATLAS event will therefore include multiple parton interactions from (i) interactions between partons coming from the proton-proton interactions that contains the hard scatter, (ii) other proton-proton interactions within the bunch crossing and (iii) remnants from prior and subsequent bunch crossings. The background introduced by (i) is part of the Underlying Event (UE), while the background from (ii) is known as in-time pileup and (iii) is out-of-time pileup.

In ATLAS the UE is best described as everything that happens in a collision that is not described by the ME. The strategy for dealing with UE is based on the approximate separation of hard and soft processes.

Much work has been done on attempting to compare UE predictions from different models (such as Pythia, Herwig and Jimmy) with data from the Tevatron and to extrapolate to LHC energies, but there are large uncertainties due to our limited understanding of physics at such high energies: parton distribution functions, initial and final state radiation and multiple parton interactions are all too poorly understood to make firm predictions at this stage.[22]. All the samples used in this analysis are inclusive of UE provided by either Herwig or by Jimmy.

The Eikonal model: (Jimmy) The UE in the samples produced for this study are provided by Jimmy. Jimmy looks at the distribution of matter within the hadron in impact parameter space, thus making it independent of the momentum fraction x carried by the partons. At low p_T and high energy the hard parton-parton cross-section is very large, larger in fact than the total proton-proton cross-section. This leads to a model of multiple parton interactions (MPI).

The 'soft underlying event' model: (Herwig) This model is based on the fact that the soft parton-parton interaction cross-section is so large that the remnants of the proton always undergo collisions themselves. This is the model used by Herwig. The issue with this model is that it does not reproduce energy flow accurately and also fails to take into account the relatively rare production of higher $\mathrm{p_T}$ particle production.

3.5 Samples used in this analysis

All of the samples used in this analysis were produced via central ATLAS production with $\sqrt{s}$ =10 TeV. This is not the nominal center of mass energy but is the energy at which we expect to take the first sizeable amount of data. A short study of the differences we expect when moving from 10 TeV to 14 TeV is given in Sec. 3.7.

The nature of the analysis presented in this thesis is such that it is considered vital to have internal consistency between the data samples used, as conclusions regarding the optimisation of the analysis are based on the quality criteria of *significance* (S), which is defined in Eq. 3.2 and is clearly completely controlled by the cross-sections of signal and background processes relative to one another. Here s= Number of signal events with reconstructed Higgs boson in mass window and b= Number of background events with reconstructed Higgs boson in mass window.

$$\mathrm{S} = \frac{s}{\sqrt{\Sigma b}} \tag{3.2}$$

As a result of this, all the background samples have their cross-sections normalised to those that would have been obtained using the internally consistent set of generator parameters listed in Table. 3.1. The cross-sections before and after these corrections are shown in Table. 3.2.

The high center of mass energy at the LHC means that production of heavy final states such as $\mathrm{t\bar{t}H^0}$ and $\mathrm{t\bar{t}X}$ can proceed using a small fraction of the protons' momenta, i.e. small x. At small x the gluon PDF dominates[23], so a large fraction of these events are produced via gluon fusion.

3.5.1 The $\mathrm{t\bar{t}H^0}$ signal sample

The $\mathrm{t\bar{t}H^0}$ signal sample used in this analysis was generated with Pythia 6.4. The samples contain only those decays where one of the top quarks decays 'hadronically' (to Wb→jjb) and the other decays to a b quark and either an electron or muon and corresponding neutrino. This was achieved by applying a lepton filter, requiring that $\mathrm{p_{T,l}} \geq 15$ GeV and $|\eta| \leq 2.7$.

Issues:

1. The sample was generated at LO with $Q^2 = m_t^2 + max(p_{T,t}^2, p_{T,\bar{t}}^2)$. This choice of Q^2 is considered reasonable as Fig. 3.2(b) shows the $\mathrm{t\bar{t}H^0}$ cross-section to be fairly stable in the vicinity of this value.

3.5.2 The $\mathrm{t\bar{t}b\bar{b}}$ (ew) background

The $\mathrm{t\bar{t}b\bar{b}}$ (ew) background sample was generated with AcerMC+Pythia. The top quarks are forced to decay 'semi-leptonically' to e/μ and hadrons.

Issues:

1. This sample was produced with $Q^2 = \hat{s}$. This is the AcerMC default value of Q^2, but is unfortunately not an appropriate one, as it does not describe the physical final state and results in a very small cross-section for this process. A temporary solution for this analysis was decided on to simply scale up the cross-section to that obtained by setting $Q^2 = \frac{m_H}{2} + m_t$.
2. The sample was generated for the process gg→$\mathrm{t\bar{t}b\bar{b}}$ only. To correct for the additional process of $q\bar{q}$ →$\mathrm{t\bar{t}b\bar{b}}$ and gq →$\mathrm{t\bar{t}b\bar{b}}$ the cross-section is scaled up by 8%[1].

#	Parameter	Value
1	m_t	172.5 GeV
2	m_H	120 GeV
3	Q^2	$(\frac{m_H}{2} + m_t)^2$
4	BR	semi-leptonic to e/μ
5	Kinematics cuts on quarks	none
6	production mode	gg, qg and q$\bar{\mathrm{q}}$

Table 3.1: Parameter set used for consistent cross-sections.

3.5.3 The $\mathrm{t\bar{t}b\bar{b}}$ (qcd) background

The $\mathrm{t\bar{t}b\bar{b}}$ (qcd) background was generated with Alpgen+Herwig for the process gg/q$\bar{\mathrm{q}}$ $\rightarrow$ $\mathrm{t\bar{t}b\bar{b}}$ where the top quarks can then decay in any way. The UE is provided by Jimmy.

3.5.4 The $\mathrm{t\bar{t}X}$ background

The $\mathrm{t\bar{t}X}$ background was generated with Alpgen+Herwig, with the UE provided by Jimmy.

Issues:

1. The sample was generated at LO with $Q^2 = m_T^2$ (the sum of the transverse mass of the final state particles). This is corrected for by scaling up to the cross-section obtained when running event generation with $Q^2 = (\frac{m_H}{2} + m_t)^2$.
2. There is some overlap between the $\mathrm{t\bar{t}X}$ and $\mathrm{t\bar{t}b\bar{b}(qcd)}$ samples, which is removed via the technique descibed in Sec. 3.6.

The TTbarPlusJets filter is applied (with modifications) to all background processes at the generator level. It requires at least 6 jets with $\mathrm{p_T} \geq 15$ GeV and at least 3 b-jets within the ID acceptance $|eta| \leq 2.7$. In addition isolated electrons from W or τ decays are removed from the jet list if $\Delta R(j,e) < 0.4$ and $\frac{\Delta pt}{pt} < 0.1$. The jet algorithm used in this filter is the ATLAS Cone algorithm with a radius $R = 0.4$.

Process	σ_{eff} (fb)	Scaled σ_{eff} (fb)	Scalings applied
$t\bar{t}H^0$	42	**42**	none
$t\bar{t}b\bar{b}$(ew)	46	**80.3**	3(+27fb) and 6(+7.3fb)
$t\bar{t}b\bar{b}$(qcd)	420	**420**	none
$t\bar{t}X$	31500	**37300**	3(+5800fb)

Table 3.2: Effective cross-sections used in this analysis.

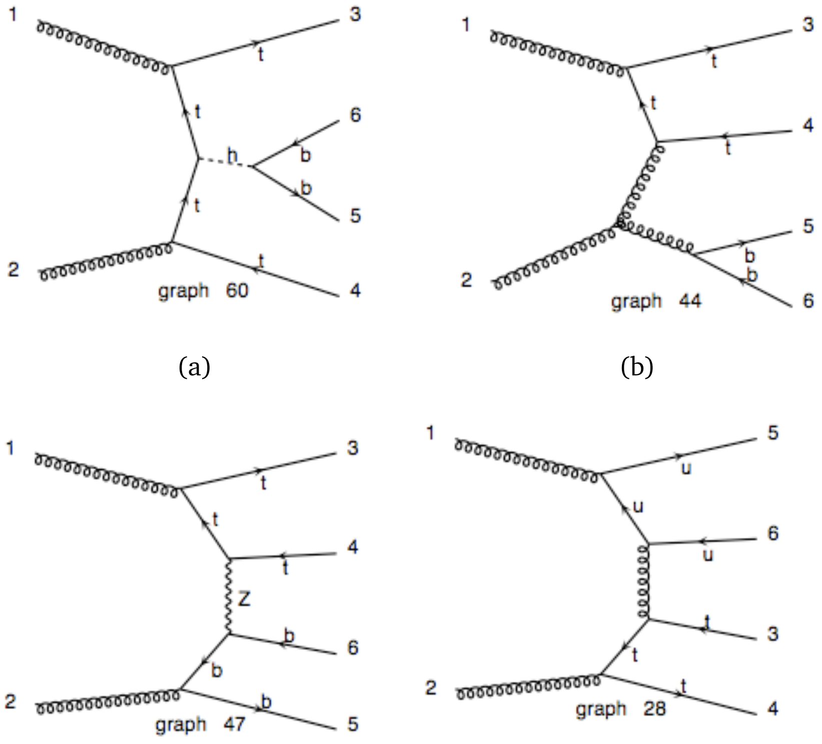

(a) (b)

(c) (d)

Figure 3.4: Selected Feynman diagrams for the signal process (a), the $t\bar{t}b\bar{b}$ background where the decay is via QCD (b) and via EW (c) and the $t\bar{t}X$ background for the case where X=jj, (d).

Sample	$\mathcal{L}$ (fb^{-1})	σ (fb)	N events generated
$\mathrm{t\bar{t}H^0}$	1048	42	44,007
$\mathrm{t\bar{t}b\bar{b}(ew)}$	623	80.3	50,000
$\mathrm{t\bar{t}b\bar{b}(qcd)}$	536	420	225,000
$\mathrm{t\bar{t}X}$	53.63	37300	2,000,622

Table 3.3: Generated luminosities in fb^{-1}.

The luminosities generated for each sample are given in Table. 3.3. Samples are scaled down to reflect the 30 fb^{-1} of data used in the study presented here.

3.6 Overlap between $\mathrm{t\bar{t}X}$ and $\mathrm{t\bar{t}b\bar{b}}$ samples

A dedicated $\mathrm{t\bar{t}b\bar{b}}$ sample is produced because the Alpgen generator settings do not allow for a fully inclusive $\mathrm{t\bar{t}X}$ sample to be produced. An example of the $\mathrm{t\bar{t}b\bar{b}}$ processes availble via Alpgen production of $\mathrm{t\bar{t}X}$ are shown in Fig. 3.5.

The $\mathrm{t\bar{t}b\bar{b}}$ sample contains all possible diagrams, therefore there is an overlap between the $\mathrm{t\bar{t}X}$ and $\mathrm{t\bar{t}b\bar{b}(qcd)}$ samples which must be removed. This is discussed firther in Sec. 7.1.

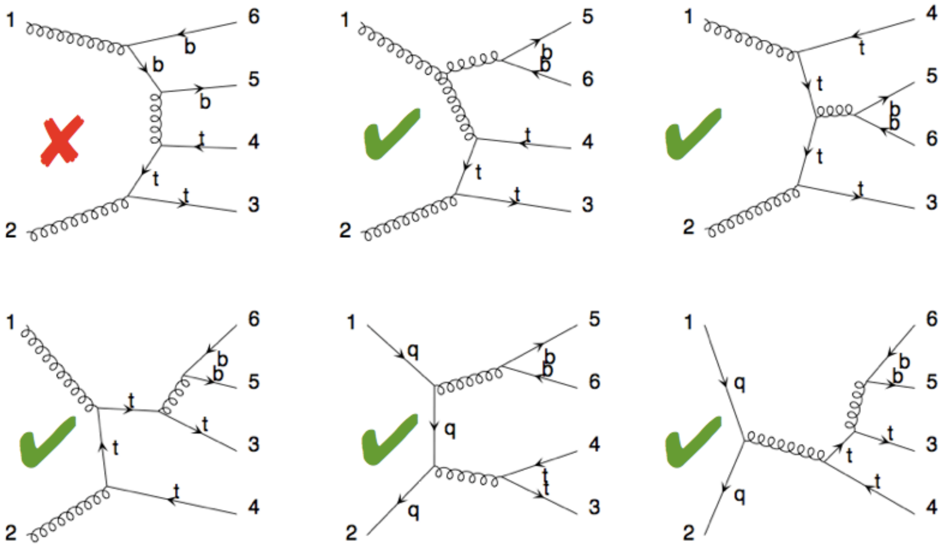

Figure 3.5: Example Feynman diagrams for the $t\bar{t}b\bar{b}$ processes included in the $t\bar{t}X$ sample (green ticks) and for the process not included in $t\bar{t}X$ (red cross).

3.7 Center of mass energy considerations

The nominal center of mass energy at the LHC is 14 TeV. However, it is expected that at startup a center of mass energy of 7 TeV will be used, followed by a longer run with 10 TeV. The analysis in this thesis is based on simulated data which was generated for a center of mass energy of 10 TeV. To move from 10 TeV to 14 TeV various cross-checks were carried out to understand how the kinematics of a $t\bar{t}H^0$ event may change, in addition to the obvious change in cross-section for the signal and all relevant background processes.

Two $t\bar{t}H^0$ samples containing 20,000 events were generated with Pythia, identical but for the center of mass energy and the mass of the $t\bar{t}H^0$ final state was calculated. The mean number of events in each bin is counted and the resulting graph in Fig. 3.6 shows the ratio per bin of the number of events with the 10 TeV sample divided by the number of events with the 14 TeV sample. This is shown as the ratio of parton luminosities as a function of the mass of the $t\bar{t}H^0$ system. The ratio of luminosities can be interpreted as the fraction of

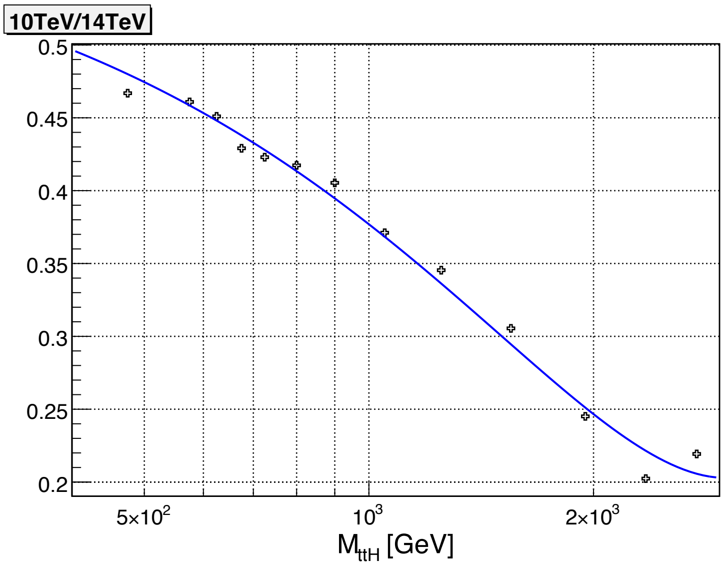

Figure 3.6: Ratio of parton luminosities as a function of the total mass of the $t\bar{t}H^0$ final state.

events with a certain final state mass that are retained when moving from 14 TeV to 10 TeV. A 10 TeV collision will produce the same final state mass as a 14 TeV collision 50% of the time if $m_{ttH} = 400 GeV$, but a 10 TeV collision will only produce a $m_{ttH} = 2$ TeV final state at 25% the rate of a 14 TeV collision. Fig. 3.7 shows the theoretical expectation for this ratio in the case of gluon gluon fusion.

Kinematical distributions for the generator level particles are shown in Fig. 3.8 and Fig. 3.9. The distributions are very similar when moving from $\sqrt{s}$ =14 to 10 TeV. There is some reduction in the mean p_T of the Higgs and top quarks with lower $\sqrt{s}$, as would be expected due to the lower phase space available. The reduced phase space is also visible as a slight narrowing of the η distributions of all the generated objects. These small changes in the final state kinematics are not considered an issue in formulating an optimal set of analysis techniques for this channel.

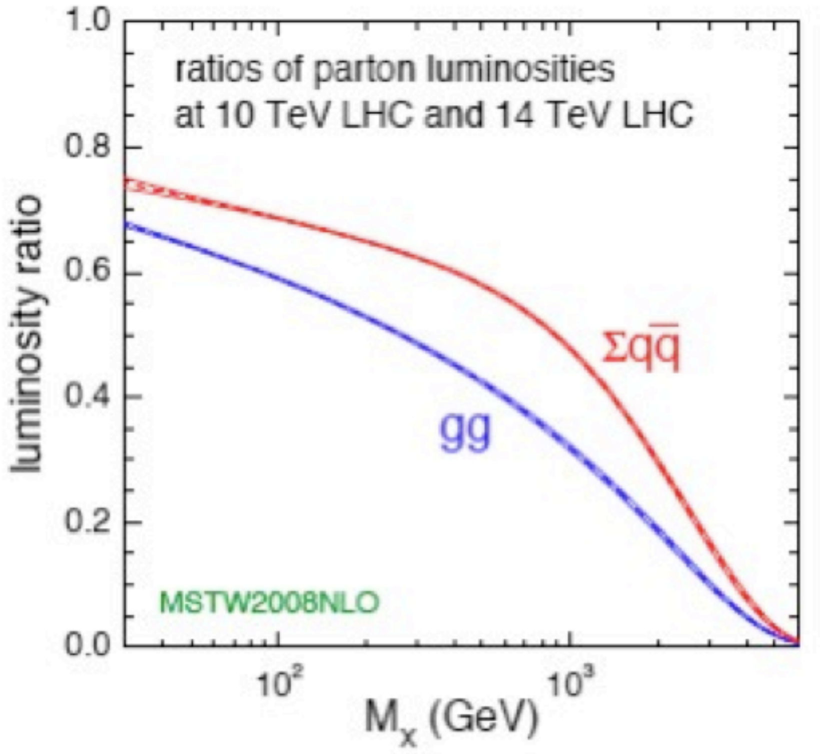

Figure 3.7: Ratio of parton luminosities at 10 TeV compared with 14 TeV at the LHC[23].

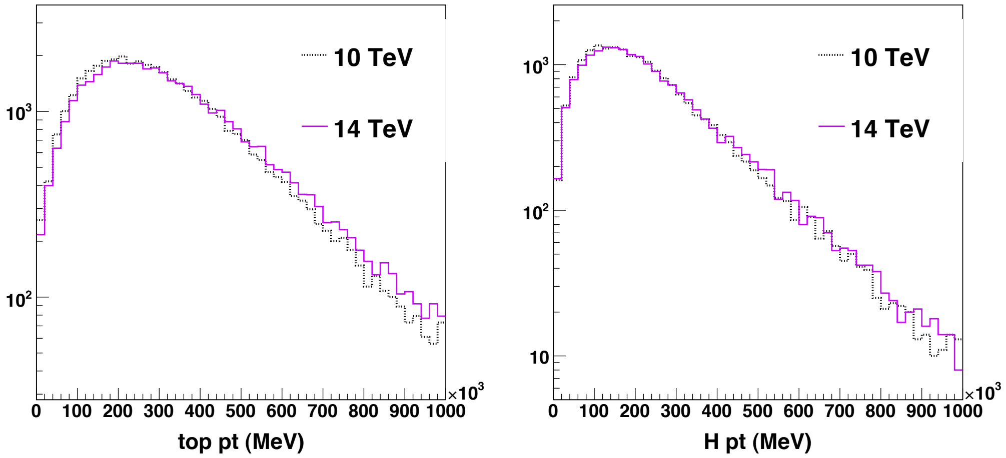

(a) top quarks (b) Higgs boson

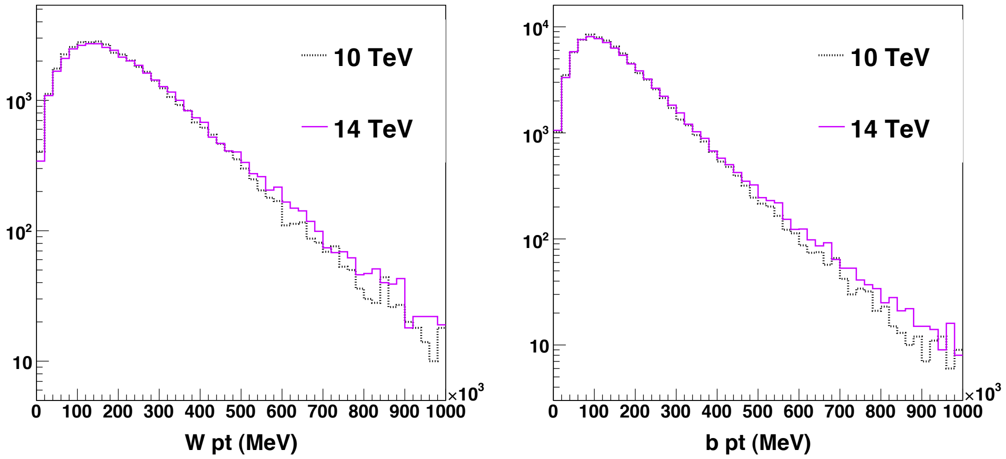

(c) W bosons (d) b quarks

Figure 3.8: $\mathrm{p_T}$ of final state particles in the $\mathrm{t\bar{t}H^0}$ sample. Samples were generated with Pythia at $\sqrt{s}$=10 TeV and $\sqrt{s}$=14 TeV.

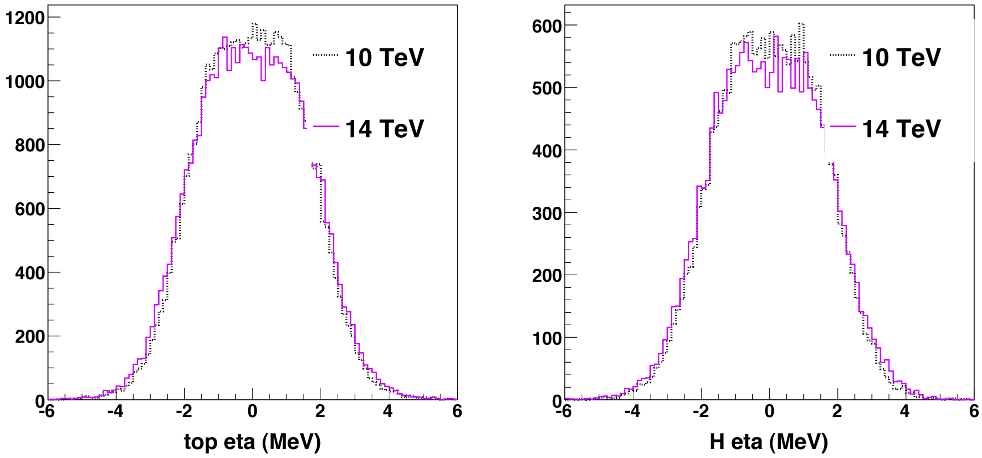

(a) top quarks

(b) Higgs boson

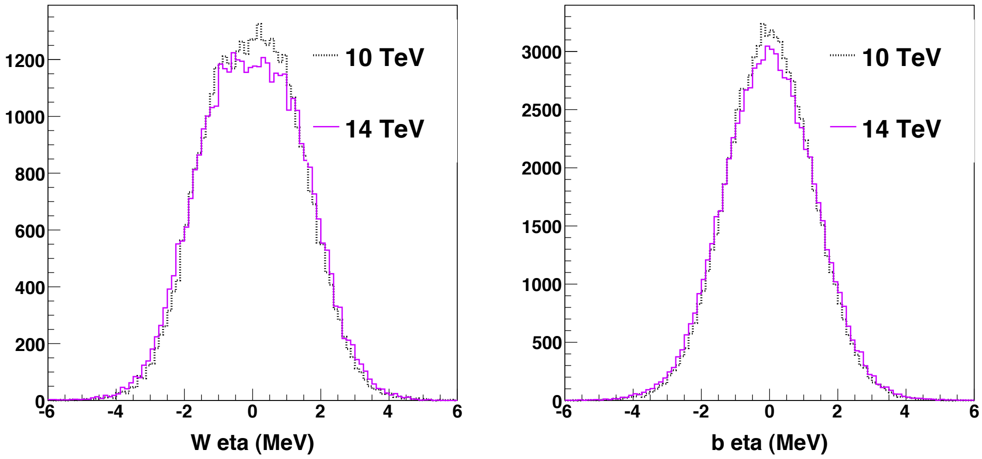

(c) W bosons

(d) b quarks

Figure 3.9: pseudorapidity η of final state particles in the $\mathrm{t\bar{t}H^0}$ sample. Samples were generated with Pythia at $\sqrt{s}$=10 TeV and $\sqrt{s}$=14 TeV.

3.8 ATLAS detector simulation

The simulation of the generated particles interactions with the ATLAS detector can be done in two ways. One way is to run the truth particles through a full Geant 4 (G4)[24] detector simulation, thus providing fully-simulated events for analysis.

G4 takes the generator level objects and propagates them through a model of the detector. Each part of the detector traversed by a generator object records its time offset and energy deposition and modifies the generator object accordingly. The full detector simulation includes a description of the detector geometry (inclusive of any misalignments) and the magnetic fields generated by both the toroid and solenoid. It also includes interactions with the dead material in the detector, such as the cooling system, wiring, support structure and shielding.

As the modelling of the entire detector is very time consuming ($\sim$ 10 minutes per event), a fast simulation of the detector has been developed, AtlFast, which uses a slightly simplified version of the detector and only concentrates on those regions considered interesting. AtlFast is described in detail elsewhere[25] and has been widely validated for a large number of physics processes.

Chapter 4

Leptons and Missing Energy

A detailed study has been made of the prospects for the channel $\mathrm{t\bar{t}H^0}$, the results of which are presented in [1]. During 2006-2008 there was an experiment-wide Computing System Commissioning (CSC), culminating in the publication of the CSC note [1], which details the status and prospects of the entire experiment at the time of publication. Here the study is re-examined in order to define areas in which the analysis could be improved. Ths CSC study was made with fully simulated data at 14 TeV.

4.1 Final state topology

According to precision electroweak measurements and direct searches (Sec. 2.3), the most probable mass range for a standard model Higgs Boson is around 120 GeV. At this mass, a Higgs Boson decays predominantly to a $\mathrm{b\bar{b}}$ pair, making it a very difficult signature to spot amongst the very busy QCD events we expect to see with ATLAS. A partial solution to this difficulty is found by looking at the case where the Higgs is produced in association with a $\mathrm{t\bar{t}}$ pair, with one of the tops decaying semi-leptonically, via $\mathrm{t} \rightarrow \mathrm{bW} \rightarrow \mathrm{bl}\nu$. If the lepton in this decay is an electron or a muon then one can exploit the high efficiency of the triggers for high $\mathrm{p_T}$ electrons and muons.

The preference for a final state topology containing only one lepton (e/μ) is due to the difficulties in reconstructing an event with two neutrinos, and

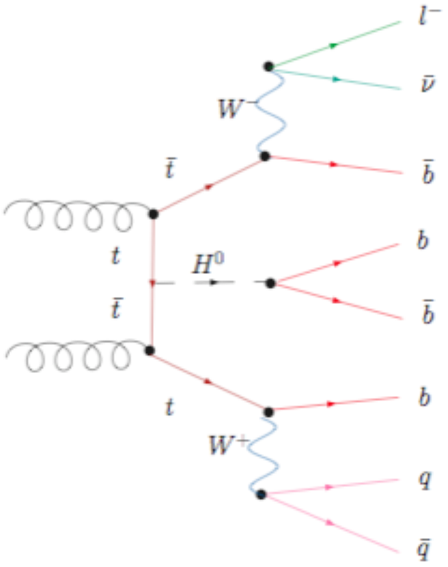

Figure 4.1: Feynman diagram for Higgs production in association with $\mathrm{t\bar{t}}$, where one top decays semi-leptonically and the Higgs decays to $\mathrm{b\bar{b}}$

so the decays where both tops decay via $t \rightarrow bW \rightarrow bl\nu$ are not considered in this study. There is thought to be some promise in considering events where both tops decay hadronically, via $t \rightarrow bW \rightarrow blq\bar{q}$, with use of a combination of multi-jet triggers [26], [27]; however the fully hadronic decay is not explored in this analysis. This analysis focuses purely on the subset of Higgs events where one of the top quarks decays semi-leptonically and the other decays hadronically. A Feynman diagram for this process is shown in Fig. 4.1

In addition to having promise as a low-mass discovery channel, $\mathrm{t\bar{t}H^0}$ is particularly interesting as a measure of the top Yukawa coupling. A standard model Higgs Boson is not expected to be of high enough mass to decay to $\mathrm{t\bar{t}}$, so one must measure the coupling at the Higgs production vertex. The channel $\mathrm{t\bar{t}H^0}$ is considered the single most promising candidate for this measurement as it is the only tree-level process by which this coupling can be measured [28].

4.2 Trigger

The presence of a single high p_T lepton in the final state makes this topology a promising one. If the lepton is an electron or muon then it is possible to trigger on the event with a high efficiency of $\sim 82\%$[1].

The triggers considered in the CSC analysis for the $\mathrm{t\bar{t}H^0}$ signature are a logical OR of the signatures **e22i** (an isolated electron, $\mathrm{p_T} \geq 22$ GeV), $\mu 20$ (a muon, $\mathrm{p_T}$ ≥ 20GeV) and **e55** (a non-isolated electron, $\mathrm{p_T} \geq 55$GeV). These triggers are described in detail in [29] and [30].

Many final state topologies other than the $\mathrm{t\bar{t}H^0(H^0 \rightarrow b\bar{b})}$ process will satisfy the trigger requirement of a high $\mathrm{p_T}$ electron or muon and the number of events passing these triggers will be very large as there are no plans to apply prescales to these signatures even at high luminosity. For this reason it is necessary to apply a set of preselection cuts to those events passing the trigger. Only those events passing preselection will be considered in the analysis, thus it is more meaningful to define the trigger efficiency in terms of preselection efficiency than in terms of the total event rate. The trigger efficiency is defined with respect to the preselection efficiency in Eq. 4.1.

$$\epsilon_{trig} = \frac{\text{N events passing trigger and preselection}}{\text{N events passing preselection}} \tag{4.1}$$

4.3 Background Processes

There are several processes with final states that could mimic $\mathrm{t\bar{t}H^0(H^0 \rightarrow b\bar{b})}$. The processes considered most relevant to this channel are described briefly in Sec. 3.5 and here in more detail. The high center of mass energy at the LHC means that $\mathrm{t\bar{t}}$ production can occur well above threshold. This means that in addition to the large $\mathrm{t\bar{t}}$ cross-section there will be a large phase space available, thus a sizeable fraction of the $\mathrm{t\bar{t}}$ cross-section will come from higher order processes. This is referred to as $\mathrm{t\bar{t}X}$, where the X is representative of some number of additional partons. The LHC will produce a $\mathrm{t\bar{t}}$ pair every second at full luminosty, making this the largest background we need to consider. The

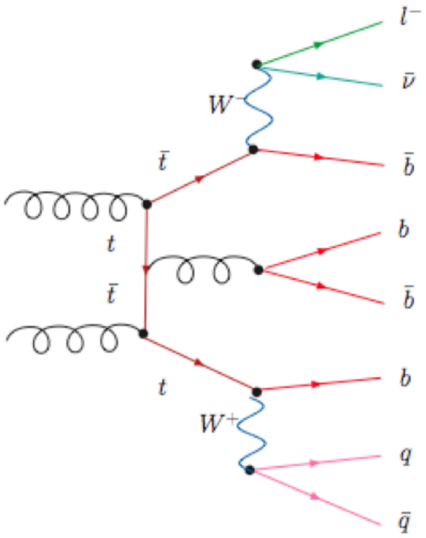

Figure 4.2: Feynman diagram for $\mathrm{t\bar{t}b\bar{b}_{SL}}$ production, which constitutes the irreducible background to $t\bar{t}H^0_{SL}(H^0 \to b\bar{b})$. This process is referred to as the *irreducible* background because it has an identical final state to the signal.

$\mathrm{t\bar{t}X}$ background is reducible in the sense that it will only very rarely mimic the $\mathrm{t\bar{t}H^0}$ final state exactly, when the X contains a $\mathrm{b\bar{b}}$. Because of this, the $\mathrm{t\bar{t}b\bar{b}}$ background is considered separately from the rest of the $\mathrm{t\bar{t}X}$. A dedicated $\mathrm{t\bar{t}b\bar{b}}$ sample is generated, as discussed in Sec. 3.5 so that all possible diagrams are included in the sample. An example diagram for this process is shown in Fig. 4.2.

The top quark decays almost exclusively ($BR \sim 99\%$)[17] to a W Boson and a b quark via the electroweak process $t \to Wb$, making it possible to classify a top quark by the decay mode of the W. In this thesis, $\mathrm{t\bar{t}X_{SL}}$ (Semi-Leptonic) refers to the case where a W from one top decay decays to a lepton and neutrino, $W \to l\nu$, and the W from the other top decays to a quark and anti-quark $W \to q\bar{q}$. By the same logic, $\mathrm{t\bar{t}X_{FH}}$ refers to the case where both Ws decay hadronically.

In the CSC analysis the dangerous backgrounds to $\mathrm{t\bar{t}H^0}$ were considered to be made up of the semi-leptonic fractions of the $\mathrm{t\bar{t}X}$ and $\mathrm{t\bar{t}b\bar{b}}$ processes. The $\mathrm{W + jets}$ background was found to be negligible after implementing the tight b-tagging requirements deemed necessary to reduce the $\mathrm{t\bar{t}X}$ to a manageable

Process	σ_{LO}	ϵ_{filt}	**BR(W→eμ, W→q$\bar{q}$)**	**BR(H→ b$\bar{b}$)**	σ_{eff}
$t\bar{t}H^0$	537	0.953	0.289	0.675	**100**
$t\bar{t}b\bar{b}$ QCD	8700	0.946	0.289	-	**2371**
$t\bar{t}b\bar{b}$ EW	940	0.943	0.289	-	**255**

Process	$\sigma_{\text{NLO}}\times$ **BR(eμ)**	ϵ_{filt}	$t\bar{t}b\bar{b}$ **removal**	σ_{eff}
$t\bar{t}_{filt}$	833000	0.146	0.9	**109487**

Table 4.1: Calculation of the effective cross-sections at 14 TeV σ_{eff} used in the CSC analysis. Cross-sections are in femtobarns.

level. The signal and background cross-sections considered in the CSC analysis are listed in Table. 4.3. The cross-sections are inclusive of all filter efficiencies and branching ratios. The generator filters applied are the same as in Sec. 3.5. The Q^2 values used in generation are $m_t^2+\text{max}(p^2_{Tt}, p^2_{T\bar{t}})$ for $t\bar{t}H^0$, $(\frac{m_H}{2}+m_t)^2$ for $t\bar{t}b\bar{b}$ and $m_t^2+\frac{p^2_{Tt},p^2_{T\bar{t}}}{2}$ for $t\bar{t}_{filt}$. The masses used in the Q^2 calculations are $m_t = 172.5$ GeV and $m_H = 120$GeV. The effective cross-section is obtained by multiplying the generator cross-section by the filter efficiency ϵ_{filt} and the relevant branching ratios BR(W→eμ) and BR(H→ b$\bar{b}$). The $t\bar{t}_{\text{filt}}$ was $t\bar{t}X$ generated at NLO with BR(W→eμ) already included. For the $t\bar{t}b\bar{b}$ backgrounds the generators used were AcerMC (hard process) and Pythia (PS, hadronisation, UE). The $t\bar{t}X$ background was produced with MC@NLO (hard process) interfaced with Herwig (PS, hadronisation) and Jimmy (UE).

4.4 Reassessment of backgrounds

The serendipitous discovery that the **fully hadronic** $t\bar{t}b\bar{b}$ was passing the preselection cuts in this analysis prompted a full reassessment of the backgrounds considered dangerous for this channel. The two most obvious exclusions in the CSC study were the cases where the $t\bar{t}X$ /$t\bar{t}b\bar{b}$ decays either (1) semi-leptonically via a τ lepton or (2) fully hadronically. These cases are reconsidered in this analysis, along with a fresh look at the $\mathrm{W+jets}$ background, which was found previously to be reduced to a negligible level by the requirement of four b-tagged jets. It is considered of interest to reassess the $\mathrm{W+jets}$ background because adjustments in b-tagging criteria are considered in this analysis.

4.4.1 Semi-leptonic decays to τ

In both the CSC analysis and the study presented here, the only semi-leptonic decays considered are those involving electrons and muons. There will also be the semi-leptonic top decays t$\rightarrow$ Wb $\rightarrow \tau\nu$ b in both the signal and background processes; they are not considered as part of the promising $\mathrm{t\bar{t}H^0_{SL}}$ processs because the τ does not share the high trigger efficiency of the e/μ. We can, however, expect some of these events to pass the e/μ triggers and $\mathrm{t\bar{t}H^0}$ preselection on the basis that they will contain an e/μ from the τ decay.

Because of the similar final state topologies of the signal and background processes one would expect the proportion of τ decay events passing preselection cuts to be the same for $\mathrm{t\bar{t}H^0}$ and for $\mathrm{t\bar{t}X}$ /$\mathrm{t\bar{t}b\bar{b}}$. This implies that the total signal and total background will increase by the same amount, thus improving the final significance on the basis that it is calculated as $\frac{s}{\sqrt{b}}$. At the time of writing no samples of either signal or background containing τ decays are available to determine how significant this effect will be, but there are no reasons to think it will have a negative effect on the final significance of this channel.

4.4.2 Fully hadronic decays

The $\mathrm{t\bar{t}b\bar{b}}$ background generated for this analysis is inclusive of all top decays rather than the purely semi-leptonic sample considered in the CSC study. The fully hadronic subset of the sample was run through the CSC-style preselection and it was discovered that a significant number of fully hadronic $\mathrm{t\bar{t}b\bar{b}}$ events were not being rejected by the cuts listed in Table. 4.3. This is considered further in Sec. 4.5. This was an important observation, although not a very surprising one in hindsight; the fully hadronic sample contains 8 jets, any one of which is highly likely to contain fake electrons, and 4 b-jets, which will contain electrons and muons from the semi-leptonic decay of the B-hadrons in them. A full summary of the final states of the backgrounds considered here is given in Table. 4.2.

Background	**Final state particles**									σ_{eff}**(fb)**
	l	ν	b	$\bar{b}$	b	$\bar{b}$	j	j	other	
$t\bar{t}H^0_{FH}$			✓	✓	✓	✓	✓	✓	jets	~ 67
$t\bar{t}H^0_{SL}$	✓	✓	✓	✓	✓	✓	✓	✓		~ 42
$t\bar{t}H^0_{FL}$	✓	✓	✓	✓	✓	✓			$l\nu$	~ 14
$t\bar{t}X_{FH}$			✓	✓			✓	✓	2-6j	$\sim$ 59,200
$t\bar{t}X_{SL}$	✓	✓	✓	✓			✓	✓	jets	$\sim$ 37,300
$t\bar{t}X_{FL}$	✓	✓	✓	✓					$l\nu$+ jets	$\sim$ 12,900
$t\bar{t}b\bar{b}_{FH}$			✓	✓	✓	✓	✓	✓	jets	~ 800
$t\bar{t}b\bar{b}_{SL}$	✓	✓	✓	✓	✓	✓	✓	✓		~ 500
$t\bar{t}b\bar{b}_{FL}$	✓	✓	✓	✓	✓	✓			$l\nu$	~ 170
$W + \text{jets}$	✓	✓					✓	✓	jets	$\sim$ 1,900,000

Table 4.2: Final state content of signal and backgrounds at $\sqrt{s}$= 10 TeV. The cross-sections here are approximate. Only the $t\bar{t}b\bar{b}_{SL}$ process exactly mimics the $t\bar{t}H^0_{SL}$ final state. All other backgrounds must fake b-jets, light jets or e/μ.

The $W + \text{jets}$ cross-section at the LHC is $\sim$ 950 pb per lepton flavour at 10 TeV[31]. The majority of this background does not contain the 6 jets needed to satisfy the preselection criteria of this analysis. The $\sim$ 10 pb per lepton flavour that does have a high enough jet multiplicity has previously been dismissed based on b-tagging preselection criteria.

To test this in the context of this analysis, preselection has been run on a small sample of $W + \text{jets}$ in order to ascertain the fraction of events passing a fairly loose b-weight cut. Ten thousand events each of filtered W plus 2,3,4 and 5 jets were considered. The samples were filtered such that the W decay is always to an electron or muon with p_T greater than 20 GeV and all the jets have p_T greater than 20 GeV.

None of the samples contained four jets with a b-weight ≥ 2.5. Unfortunately the sample size available for this study was not large enough to state categorically that no danger is posed from the $\mathrm{W} + \mathrm{jets}$ background, but neither does it raise any concern, particularly considering the very strong filter (mimicking the event selection implemented in the $\mathrm{t\bar{t}H^0}$ analysis presented here) applied to these samples.

4.5 Lepton and missing energy preselection

The baseline lepton preselection for this channel consists of a requirement that there be exactly one lepton, either an electron or a muon, satisfying the criteria in Table. 4.3

In reassessing the lepton preselection, the first thing considered here is the background contribution from fully hadronic $\mathrm{t\bar{t}X}$ and $\mathrm{t\bar{t}b\bar{b}}$ processes, as mentioned in Sec. 4.4.2. It was found that roughly the same number of events fromthe $\mathrm{t\bar{t}b\bar{b}_{FH}}$ and $\mathrm{t\bar{t}b\bar{b}_{SL}}$ were surviving the full lepton and jet preselection cuts, Table. 4.4, doubling the size of the $\mathrm{t\bar{t}b\bar{b}}$ background considered previously [1].

A data sample of $\mathrm{t\bar{t}X_{FH}}$ was not available for this study, however there are certain things we can say about the prospect of the already vast $\mathrm{t\bar{t}X}$ background doubling in size; There are two mechanisms via which a fully hadronic event can pass the lepton preselection cuts listed in Table. 4.3:

1. **The b-jets in the event may contain a B-hadron that decays semi-leptonically, producing a real lepton.** The decay of a b quark is almost always via b→cW(c→dW), thus there will be an e/μ from W decay in $\sim 36\%$ of b-jets. The $\mathrm{t\bar{t}b\bar{b}_{FH}}$ contribution contains twice as many b-jets as the $\mathrm{t\bar{t}X_{FH}}$, suggesting that the proportion of $\mathrm{t\bar{t}X_{FH}}$ passing preselection with a lepton from such a decay will be half that coming from $\mathrm{t\bar{t}b\bar{b}_{FH}}$ via the same mechanism.

2. **The lepton can be faked.** Pions and kaons can cause inner detector tracks that are reconstructed as electrons. The fake rate due to these particles can be reduced by utilising the TRT detector's ability to distinguish between

Parameter	**Electron**	**Muon**
$\mathrm{p_T}$ (GeV)	≥ 25	≥ 20
$\lvert\eta\rvert$	≤ 2.5	≤ 2.5
author	softe or egamma	staco
splash	≤ 0.15	0.3
$\mathrm{E_T}$ in cone R=0.2	-	10 GeV
isEM quality	LooseElectron	-
$\frac{\chi^2}{d.o.f}$	-	≤ 30
d0	-	≤ 0.05

Table 4.3: Lepton preselection criteria in the CSC analysis.

	ϵ_{lep}	$\epsilon_{lep+jet}$
$\mathrm{t\bar{t}b\bar{b}_{SL}}$	66%	3%
$\mathrm{t\bar{t}b\bar{b}_{FH}}$	5%	2%

Table 4.4: Percentage of $\mathrm{t\bar{t}b\bar{b}_{SL}}$ and $\mathrm{t\bar{t}b\bar{b}_{FH}}$ events passing lepton preselection and lepton+jet preselection.

eletromagnetic and hadronic particles, and by demanding some isolation of the EMCAL energy deposit. A fake electron will not be accompanied by the $\not\!\!E_\mathrm{T}$ associated with the production of a real electron. The fake rate for muons is much lower than for electrons due to the requirement of a well reconstructed track in the muon chambers as well as the inner detector.

4.5.1 Missing energy

In light of the danger presented by $\mathrm{t\bar{t}b\bar{b}_{FH}}$ (and by inference from $\mathrm{t\bar{t}X_{FH}}$), it was considered necessary to explore the effect of applying a $\not\!\!E_\mathrm{T}$ cut at preselection stage. Fig. 4.3 show the $\not\!\!E_\mathrm{T}$ distributions for $\mathrm{t\bar{t}b\bar{b}_{FH}}$ and the $\mathrm{t\bar{t}H^0}$ signal. Although a cut at ~ 30 GeV appears optimal from these distributions, one must also keep in mind the unknown $\mathrm{t\bar{t}X_{FH}}$ $\not\!\!E_\mathrm{T}$ distribution. It is felt that a $\mathrm{t\bar{t}X_{FH}}$ event will contain, on average, a slightly lower $\not{E}_T$ than $t\bar{t}b\bar{b}_{FH}$ due to there being fewer b-jets available for semi-leptonic decay. It is therefore felt that a good place to cut on $\not{E}_T$ is at 20 GeV. The addition of this cut on $\not{E}_T$ was found to reduce the $t\bar{t}b\bar{b}_{FH}$ contribution by a factor ~ 2, while leaving the signal largely untouched. However, with the $\not{E}_T$ cut applied there was some concern that 2.7% of $t\bar{t}b\bar{b}_{FH}$ events were still passing lepton preselection. It was considered that this could translate into a rather large problem, for the following reasons:

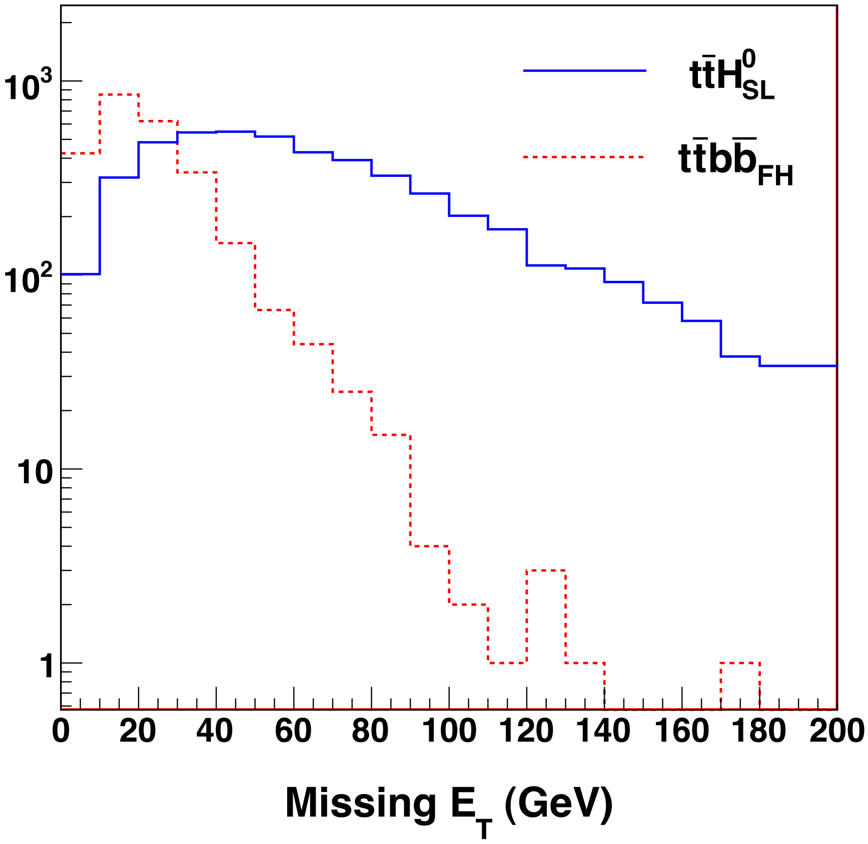

Figure 4.3: Missing transverse energy in the semi-leptonic $t\bar{t}H^0$ and fully hadronic $t\bar{t}b\bar{b}$ samples.

1. The $t\bar{t}b\bar{b}_{FH}$ has a final state with 8 jets, making any events passing lepton preselection more dangerous than the $t\bar{t}b\bar{b}_{SL}$ when it comes to reconstructing the final state objects. This combinatorial background arising from

having many jets available for the reconstruction of the $\mathrm{t\bar{t}H^0}$ system is discussed further in Sec. 5.5.

2. Although 2.7% of the $\mathrm{t\bar{t}b\bar{b}_{FH}}$ cross-section is not unmanageably large, when one considers that a similar fraction of the $\mathrm{t\bar{t}X_{FH}}$ cross-section will also be passing preselection the effect from the fully hadronic backgrounds becomes very large, and as mentioned in point (1), more dangerous than $\mathrm{t\bar{t}X_{SL}}$ from a combinatorial point of view.

The decision was made to explore how the fully hadronic background could be reduced further via adjustment of the lepton preselection cuts shown in Table. 4.3.

4.5.2 Electrons

Electron Identification: The preselection reads in a container of reconstructed electrons that have a certain author assigned to them. The electron author refers to the algorithm that reconstructed the electron. Only those electrons reconstructed with author ‘Egamma’ or author ‘soft e’ are accepted.

Quality criteria: An electron’s quality is defined by the isEM bitwise operator which contains information on the shape of the shower in the calorimeter, thus enabling a decision to be made on how electron-like it is. The various isEM definitions are shown in Table. 4.5.

Isolation A cone is drawn around the electron track, forming a circle of radius R in (η, ϕ). Here the splash is defined as the $\mathrm{E_T}$ in a cone of R=0.2 divided by the $\mathrm{p_T}$ of the electron track, as defined in Eq. 4.2.

$$\text{splash} = \frac{E_T(R = 0.2)}{p_T} \tag{4.2}$$

Geometrical acceptance Electron reconstruction is limited in η by the acceptance of the barrel section of the inner detector, which extends to $|\eta| < 2.5$.

isEM flag	**Definition**
ElectronLoose	middle layer of calo and hadronic leakage
ElectronMediumNoIso	+ calo strips and tracking (no b-layer)
ElectronMedium	+ cluster isolation and track matching in η
ElectronTightNoIsolation	+ b-layer, track match E/p $+\phi$, non iso TRT ratio
ElectronTight	+ isolation in calorimeter and TRT

Table 4.5: Basic definitions of quality requirement isEM flags for electron reconstruction.

Transverse momenta The $\mathrm{p_T}$ of an electron is measured from the curvature of its track in the inner detector.

4.5.3 Muons

The set of selection criteria applied to muons are similar to those for electrons, with some clear differences based on the reconstruction of these objects. Muons are reconstructed using tracks found in the muon chambers and matched back to inner detector tracks. A χ^2 variable is determined from the combined fit between inner detector and muon chamber tracks. It is this χ^2 that is used to define the quality of the reconstructed muon. In addition, a cut is applied on the maximum value for the transverse impact parameter, d_0, of the muon track. This is done in order to exclude those muons originating from b decays.

4.5.4 Discriminating between fake and real leptons

The discovery that a significant proportion of fully hadronic background was passing preselection even after application of an $\not{E}_\mathrm{T}$ cut prompted a study of the lepton selection cuts applied with respect to reducing the fake rate. Fig. 4.4 shows the electron isolation, $\mathrm{p_T}$ and η distributions for reconstructed electrons after they have been ΔR matched to different Monte Carlo truth objects.

A trigger electron must be matched to a true electron, and in addition the true electron must come from the decay chain $t \to W \to e\nu_e$. **A fake electron** is a reconstructed electron that has been matched to a truth particle other than an electron. These are usually charged pions and kaons. **A conversion electron** is one which has been truth matched to a true electron coming from photon conversion, i.e. pair production in the detector. The electrons labeled **'other'** in these figures are matched to true electrons from other sources. An example of this is electrons produced in semi-leptonic decays of b-hadrons.

It is clear from Fig. 4.4(b) that the η cut applied in Table. 4.3 is redundant, as would be expected; the electron reconstruction algorithms work with tracks, and the ATLAS tracking extends only to $\eta \leq 2.5$, the acceptance of the inner detector. The $\mathrm{p_T}$ cut favoured in the CSC study was 25 GeV. This is considered reasonable based on Fig. 4.4(c). The cut on the electron 'splash', or ratio of $\mathrm{E_T}$ in cone 0.2 divided by electron $\mathrm{p_T}$, provides optimum rejection of non-trigger electrons at value ≤ 0.15. This is in agreement with the cut implemented in the CSC analysis and shown in Table. 4.3.

The same distributions for muons are shown in Fig. 4.5 with the addition of the χ^2 track quality distributions. All the distributions show agreement with the cuts used in the CSC analysis. In the case of muons there does appear to be some small benefit in applying the $\eta \leq 2.5$ cut, as it removes the small number of fake muons that fall outside the region of inner detector acceptance. The χ^2 distribution in Fig. 4.5(d) indicates that a cut on $\chi^2 \leq 30$ will have no effect on the reduction of fake or 'other' muons passing preselection. A cut at $\chi^2 \leq 5$ will result in maximising the number of trigger muons with respect to fakes.

The $\mathrm{t\bar{t}b\bar{b}_{FH}}$ events passing lepton preselection were found to be almost exclusively electron rather than muon events. The electron isEM parameter favoured in the CSC study was ElectronLoose, meaning that no tracking is used in the determination of the electron quality. The basic definitions of the isEM flags are shown in Table. 4.5.

The isEM flag was varied to determine which electron quality cut provides the greatest reduction in $\mathrm{t\bar{t}b\bar{b}_{FH}}$ background, while preserving the $\mathrm{t\bar{t}H^0_{SL}}$. The cut flow for $\mathrm{t\bar{t}b\bar{b}_{SL}}$, $\mathrm{t\bar{t}b\bar{b}_{FH}}$ and $\mathrm{t\bar{t}H^0}$ is shown in Table. 4.6. Use of reduced calorimeter information and tracking in the electron isolation provides a factor $\sim$ 5 reduction in the background contribution from $\mathrm{t\bar{t}b\bar{b}_{FH}}$ with respect to that achieved by applying the $\not{E}_\mathrm{T}$ cut alone. The same cut reduces the $\mathrm{t\bar{t}H^0}$

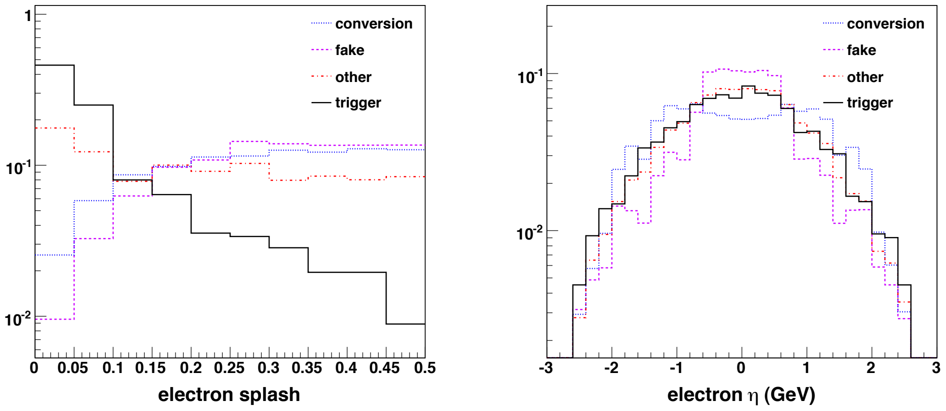

(a) electron isolation (b) electron η

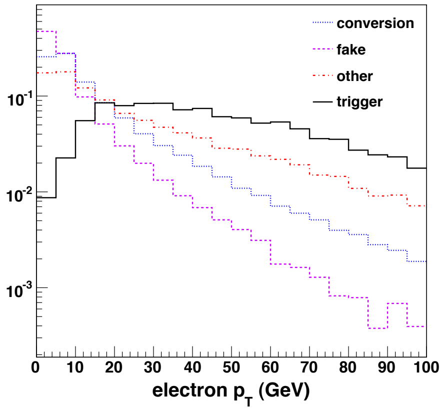

(c) electron p_T

Figure 4.4: Kinematic distributions for electrons designated as trigger, fake, conversion or 'other'. See text for explanation.

preselection efficiency by just 5%. The MediumElectronNoIso flag is therefore considered to be the best choice for this analysis.

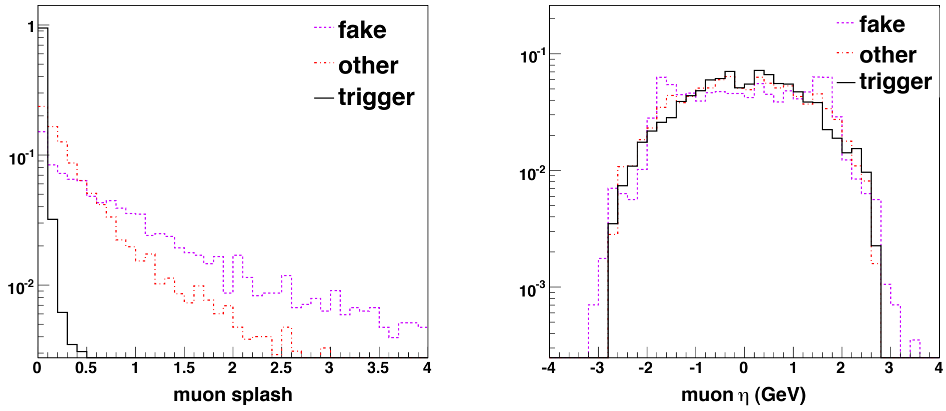

(a) muon isolation (b) muon η

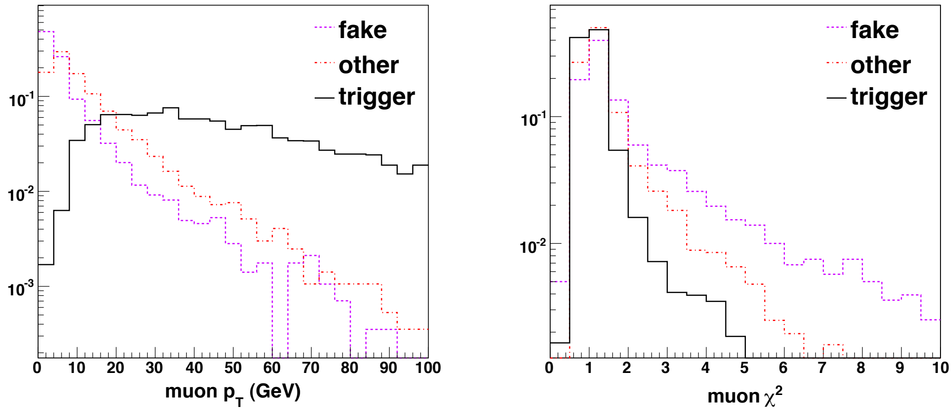

(c) muon p_T (d) muon χ^2

Figure 4.5: Kinematic distributions for muons designated as trigger, fake or 'other'. See text for explanation.

Lepton preselection	$t\bar{t}b\bar{b}_{\mathrm{FH}}$	$t\bar{t}b\bar{b}_{\mathrm{SL}}$	$t\bar{t}H^0$
standard CSC-style	5.3%	65.9%	68.7%
+ME_T20	2.7%	61.3%	62.1%
+MediumElectronNoIso	0.5%	56.1%	59.1
+MediumElectron	0.4%	55.9%	58.7
+TightElectronNoIso	0.4%	54.2%	57.3
+TightElectron	0.4%	53.2%	56.5

Table 4.6: Cut flow with variation of the isEM (electron isolation) flag for $t\bar{t}b\bar{b}$ backgrounds and $t\bar{t}H^0$. Also shown is the effect of including an $\not{E}_T$ cut of 20 GeV.

4.6 Corrections to $\not{E}_{\mathrm{T}}$

The treatment of jets will be discussed in the following chapter, Sec. 5.2, part of which concentrates on the corrections made to jets for the semi-leptonic decays of B Mesons. A semi-leptonic decay will result in the loss of part of the jet's energy as it is carried off by one or more neutrinos produced in the decay. An illustration of this is shown in Fig. 4.6. The energy carried by the muon is, in principle, detectable but some of this energy can also be lost.

The missing energy read into this analysis has been corrected and refined such that it should accurately reproduce the energy of the neutrino(s) in the event. The correction made to a jet for semi-leptonic decay involves increasing the energy of the b-jet to account for the energy lost to the neutrino. This energy should then be subtracted vectorially from the total missing energy to avoid double counting the $\not{E}_{\mathrm{T}}$. This is done in the jet preselection stage of the analysis. The corrected missing energy $\not{E}_{\mathrm{T}_{\mathrm{cor}}}$ is what is then passed on to be used in the reconstruction of the leptonically decaying W, $W_{l\nu}$.

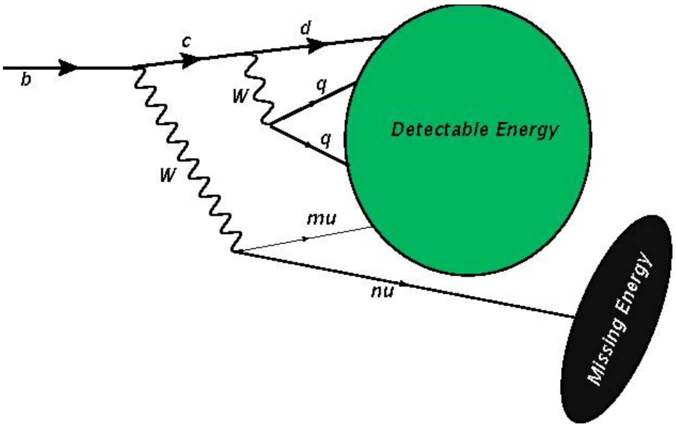

Figure 4.6: An illustration of the $\not{E}_{\mathrm{T}}$ in a semi-leptonic b decay.

4.7 Reconstructing the $\mathrm{W}_{\mathrm{l}\nu}$

The leptonically decaying W, $\mathrm{W}_{\mathrm{l}\nu}$, is reconstructed from the trigger lepton and the $\not{E}_{\mathrm{T}_{\mathrm{cor}}}$ in the event. There is a difficulty in this reconstruction due to our inability to accurately determine the component of the neutrino's momentum in the direction $\hat{z}$, along the beam pipe. This is because we equate the neutrino momentum to be the missing energy in the event, and we are only able to calculate the missing **transverse** energy, $\not{E}_{\mathrm{T}}$. Energy lost down the beam pipe is not recoverable as we have no detector coverage in this region.

$$M_W^2 = \left(E^\nu + E^l\right)^2 - \left(p_z^\nu + p_z^l\right)^2 - \left(p_y^\nu + p_y^l\right)^2 - \left(p_z^\nu + p_z^l\right)^2 \tag{4.3}$$

One can make a quadratic equation in p_z^ν (Eq. 4.4) for which a solution is found as long as the lepton neutrino invariant mass does not fluctuate above the nominal W mass M_W.

$$M_W^2 = m_l^2 - 2\left(p_x^l p_x^\nu + p_y^l p_y^\nu\right) + 2E_l\sqrt{\not{E}_T^2 + \left(p_z^\nu\right)^2} - 2\left(p_z^l p_z^\nu\right) \tag{4.4}$$

In the cases where this fluctuation above M_W does occur, no solution can be found using Eq. 4.4. This is the case in $\sim 28\%$ of $\mathrm{t\bar{t}H^0}$ events. This translates as the quadratic equation having no real solution and is a result of the limited resolution on the $\not{E}_{\mathrm{T}}$ [1]. In these cases one can estimate the $\not{E}_{\mathrm{T}}$ using the

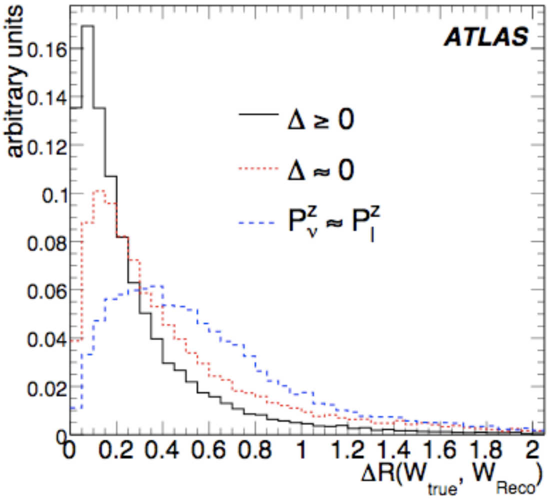

Figure 4.7: The angular separation ΔR between the true and reconstructed $\mathrm{W}_{\mathrm{l}\nu}$ where the $\mathrm{W}_{\mathrm{l}\nu}$ is reconstructed using the p_z solution and the collinear ($p_z^\nu = p_z^l$) and $\Delta = 0$ approximations. Figure from[1].

collinear approximation, in which the further approximation is made that $p_z^\nu = p_z^l$. This gives a resolution of 54 GeV. Another possibility is to use the $\Delta = 0$ **approximation**: we take the complex roots of the equation and just drop the imaginary part. For this we get a resolution of 40 GeV.

The mass obtained using these methods is shown in Fig. 4.8 [1]. The difference in direction ΔR between the true and reconstructed $\mathrm{W}_{\mathrm{l}\nu}$ is shown in Fig. 4.7 for the three methods discussed here.

The $\mathrm{W}_{\mathrm{l}\nu}$ will have the nominal M_{W} by design, and so the reconstructed mass cannot be used as a quality measure for selecting the 'best' $\mathrm{W}_{\mathrm{l}\nu}$. Only one leptonic W candidate is reconstructed for each event. In both the approximate methods the mass constraint on the W is lost, so we must apply a cut of 160 GeV on the mass of the leptonic W.

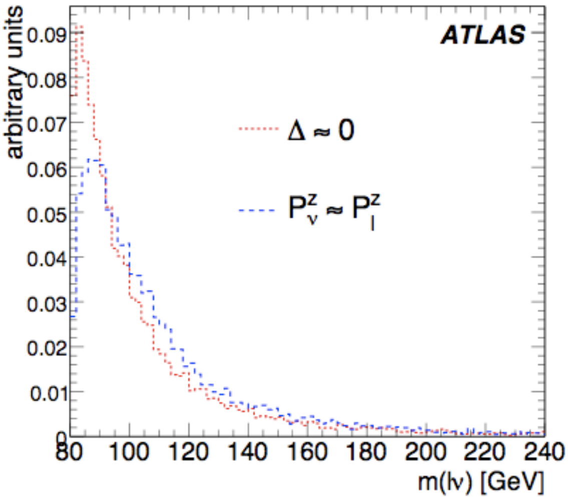

Figure 4.8: The reconstructed $\mathrm{W}_{l\nu}$ mass obtained using the collinear ($p_z^\nu = p_z^l$) and $\Delta = 0$ approximations. Figure from[1].

4.8 Systematic Uncertainties

The systematic uncertainties associated with leptons and $\not{E}_\mathrm{T}$ are consequences of an imperfect detector or an imperfect understanding of the detector. A detailed study has been made on these systematics as part of the experiment-wide CSC study[32]. The systematics listed here are for an integrated luminosity of 10 fb^{-1} and are assumptions which can be tested and modified from data with the tag-and-probe method for known resonances such as $\mathrm{Z} \to \mathrm{ee}$[33].

1. **Lepton identification efficiency:** The systematic uncertainty on the efficiency for reconstructing an electron(muon) is expected to be $0.2\%(0.1\%)$.
2. **Lepton energy scale**: The systematic uncertainty is expected to be 0.1% for both electrons and muons.
3. **Lepton fake rate**: The systematic uncertainty on the electron fake rate is expected to be around 10%.
4. $\not{E}_\mathrm{T}$ **scale:** The systematic uncertainty on the missing energy scale is expected to be around 10%.

Chapter 5

Preselection of Events Based on Jet Properties

The final state of the channel $t\bar{t}H^0(H^0 \to b\bar{b})$ is complex, with at least 6 jets, a lepton and missing energy (the neutrino). The task of successfully discriminating this signal from the enormous QCD background is reliant on concentrating on the unusual aspects of the final state topology, such as the presence of four b-jets in the final state.The possibility of tagging these jets with one of the many available b-tagging algorithms[1] makes this an interesting focus for any $t\bar{t}H^0$ analysis.

Presented in this chapter is a short review of the jet preselection procedure employed in the CSC study, followed by a discussion of jet energy corrections, p_T requirements and flavor tagging. Systematic uncertainties relating to these measurements and procedures are also summarised. The issues related to the choice of jet algorithm for this study are considered to be of great importance and are explored in detail in the next chapter.

5.1 Treatment of jets in the CSC analysis

In the CSC study, preselection cuts are applied to jets made from calorimeter towers (energy deposits) using the ATLAS Cone algorithm with cone radius R=0.4. At least six jets are required to have $p_T \geq 20$ GeV and at least four jets must have an IP3D+SV1 b-tag weight ≥ 5.5. All of the jet preselection cuts and corrections are optimised with respect to jets defined with the ATLAS cone algorithm, which was the standard at the time the CSC analysis was undertaken. A detailed study on the optimum jet algorithm for this channel is presented in this thesis, Chapter(6).

No corrections are made to the jets prior to preselection. Following the preselection cuts, the 4-momenta of all the jets are corrected. The first correction is the addition of soft muons to jets. Jets identified as having a muon carrying $\mathrm{p_T}$ ≥ 6GeV within Δ R $\leq$ 0.4 of the jet axis, where the muon is not the trigger lepton, have the muon added into the jet to correct for energy losses from semileptonic b-hadron decays. This correction is made *after* the jet preselection cuts are applied. In addition to the soft muon correction, a $\mathrm{p_T}$ dependent 'out-of-cone' correction is applied to all jets, also after preselection. This correction is determined by comparing the reconstructed jet $\mathrm{p_T}$ to that of the associated (truth-matched) quark over a range of quark $\mathrm{p_T}$. Following these corrections (and if the event is triggered by an electron) a check is made to see if the preselected 'trigger' electron overlaps with any of the jets. If the electron is within Δ R≤ 0.2 of the jet axis and carries greater than 75% of the jet's $\mathrm{p_T}$, then the jet is discarded. This step is taken to remove jets faked by electrons. All of the preselection cuts are chosen in order to optimise the significance of the $\mathrm{t\bar{t}H^0}$ signal with respect to the backgrounds considered in the CSC note: the semi-leptonically decaying $\mathrm{t\bar{t}X}$ and $\mathrm{t\bar{t}b\bar{b}}$. The reconstruction of the final state as implemented in the CSC study is described in Chapter (7).

5.2 Jet energy corrections

A b-quark decays almost exclusively via the chain b$\rightarrow$ $\mathrm{cW(c \rightarrow dW)}$[17]. The probability for a b-jet to decay semi-leptonically is therefore determined by the branching ratio for W$\rightarrow$ lν, which is approximately 10% per lepton flavour. When cascade decays are taken into consideration (Fig. 5.19(a)) this translates to an 18% probability that a b-jet will contain a muon, and a 1% probability that it will contain 2 muons.

Muons with $\mathrm{p_T} \lesssim$ 500 GeV lose energy primarily by ionisation. As a jet is made from energy deposits in the calorimeter, and muons do not tend to shower in the calorimeter, the momentum carried by the muon is not included in the jet. Missing the muon therefore results in the jet being reconstructed with significantly underestimated momentum and with its direction affected. In addition to this, the muon is accompanied by a neutrino which can further reduce the jet's energy. The presence of the neutrino alone has been found to reduce the jet's energy by an average of $\sim 10\%$[34]. The addition of soft muons and the correction for neutrino energy are both considered important corrections to the semi-leptonically decaying b-jets.

Two methods for such corrections are investigated here. The first method is that employed in the CSC study, in which any muons found within the ΔR≤ 0.4 of the jet direction are considered for addition into the jet. The second method is that employed in a recent study [34], which corrects semi-leptonic b-jets for both muon and the neutrino.

Fig. 5.1 shows the b-jet $\mathrm{p_T}$ resolution (true b-quark $\mathrm{p_T}$ - jet $\mathrm{p_T}$ divided by true b-quark $\mathrm{p_T}$) for jets reconstructed with the AntiKt algorithm with a distance parameter R=0.4, for the cases where the jets are uncorrected, corrected for μ and corrected for both $\mu + \nu$. The tail to the right of the plot contains the large number of b-jets with underestimated $\mathrm{p_T}$. It is clear that neither of the corrections have a significant positive impact on the b-jet resolution, and that a more sophisticated study is necessary to explore the improvements to b-jet $\mathrm{p_T}$ resolution that may be possible. These corrections are not considered further in this analysis.

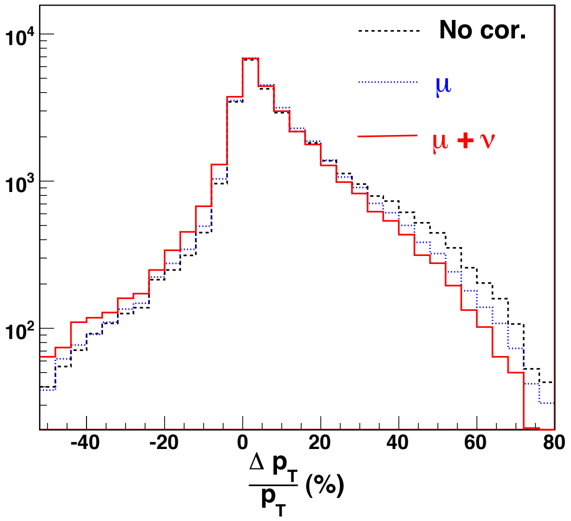

Figure 5.1: The effect of semi-leptonic corrections on the p_T resolution of b-jets in the $t\bar{t}H^0$ sample. The dotted (blue) histogram shows the resolution obtained when applying a CSC-style correction for muons only. The dashed (red) histogram shows the resolution when the b-jets are corrected for both muon and neutrino p_T losses. The large shoulder indicates that there are many jets with underestimated p_T , as is expected in the case b-jets containing semi-leptonic decays to muons and neutrinos.

5.3 Jet p_T cuts

The requirement of a final state with at least six jets reconstructed with $p_T \geq 20$ GeV places the jet p_T cut in a region where the resolution is poor according to Eq. 5.1. Because of the inverse realtionship between the resolution and the jet E_T , it is considered preferable to make the jet p_T cuts as high as possible without losing too much signal. The p_T resolution for jets in the $t\bar{t}H^0$ sample is shown in Fig. 5.2 as a function of the truth-matched quark p_T , where one can clearly see the improvement in resolution that could be obtained by considering jets with p_T >40 GeV in comparison with jets >20 GeV.

$$\frac{\sigma E_T}{E_T} = \frac{a}{\sqrt{E_T}} \oplus \frac{b}{E_T} \oplus c \tag{5.1}$$

This analysis relies heavily on the good mass reconstruction of the W_{jj} and both top quarks, all of which are constructed in some way from the jet p_T . Because of this it is considered important to select events with enough jets in a p_T region where a good resolution can be obtained. An example of the knock-on effect of jet resolution is the case of the W_{jj} mass; the mass of the W_{jj} is obtained according to Eq. 5.2, where the dependence on good jet energy reconstruction can clearly be seen.

$$m_W^2 = m_1^2 + m_2^2 + 2\left(E_1E_2 - \sqrt{E_1^2 - m_1^2}\sqrt{E_2^2 - m_2^2}\cos\theta_{12}\right) \tag{5.2}$$

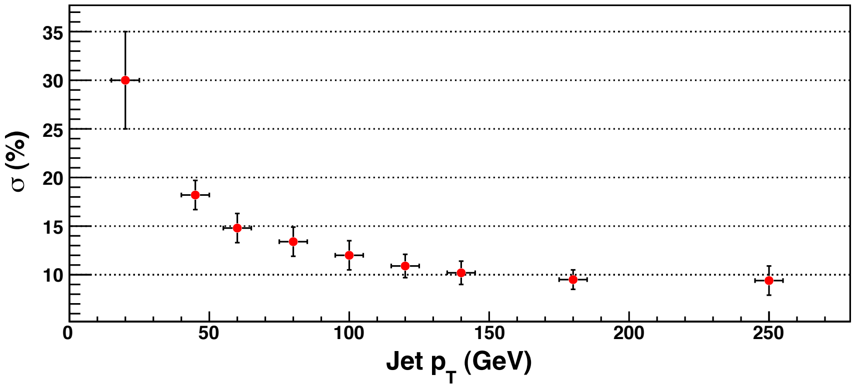

Figure 5.2: Jet p_T resolution as a function of truth-matched quark p_T , where the quark is within ΔR<0.2 of the jet axis.

An equally important factor in deciding where to cut on a jet's p_T is the amount of activity around the cut region. Any change in efficiency due to varying the p_T cut is translated into a systematic error on the analysis and the jet energy scale (JES) systematics have been found to be particularly pernicious when reconstructing multi-jet final states such as the signal and background processes considered here. The systematic uncertainties associated with the JES are discussed further in Sec. 5.3.1.

By ordering the jets in an event based on their p_T , one can make staggered p_T cuts in place of the standard single cut of 20 GeV that was favoured in the CSC study. The p_T distributions for each jet are shown in Fig. 5.3 for semi-leptonically decaying $\mathrm{t\bar{t}H^0}$, $\mathrm{t\bar{t}X}$ and $\mathrm{t\bar{t}b\bar{b}}$ events. Fig. 5.4 shows the preselection efficiency as a function of the $\mathrm{p_T}$ cut imposed on the four hardest jets in the event. Staggered $\mathrm{p_T}$ cuts of 60 GeV, 40 GeV and 30 GeV on the hardest three jets in the event leave the $\mathrm{t\bar{t}H^0}$ signal intact while reducing the background, in particular the $\mathrm{t\bar{t}X}$. The remainder of the jets required in preselection are left with with the minimum $\mathrm{p_T}$ cut of 20 GeV as no benefit is seen in cutting harder on these softer jets.

5.3.1 Effect of $\mathrm{p_T}$ cuts on JES uncertainty

It is of utmost importance to try to understand and control the systematic uncertainties relating to this channel.

The largest contribution to the systematic uncertainty comes from the JES, which is a measure of how accurately the ATLAS detector can measure a jet's energy. To determine the systematic uncertainty for this analysis resulting from the uncertainty on the JES all jets have their $\mathrm{p_T}$ varied up and down by 1σ. The current recommendation from calorimeter experts is to use $\sigma = 7\%$ for all jets, independent of their energy. The event selection efficiency is then calculated using the jets shifted up and down by 1σ and the difference in the efficiency obtained using the shifted jets gives the uncertainty on event selection efficiency. Because the only effect on this uncertainty comes from jets lying in the region of the $\mathrm{p_T}$ cut $\pm 1\sigma$, it is preferable to choose a cut in a region which is not too heavily populated. This is kept in mind when choosing the $\mathrm{p_T}$ cuts described in the previous section and is explored further in Sec. 7.3.1.

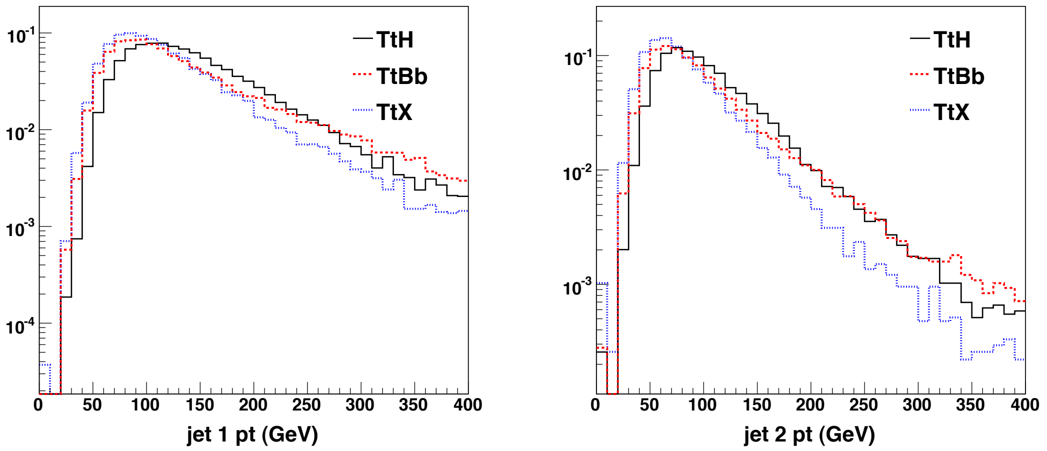

(a) Hardest jet p_T .

(b) 2^{nd} hardest jet p_T .

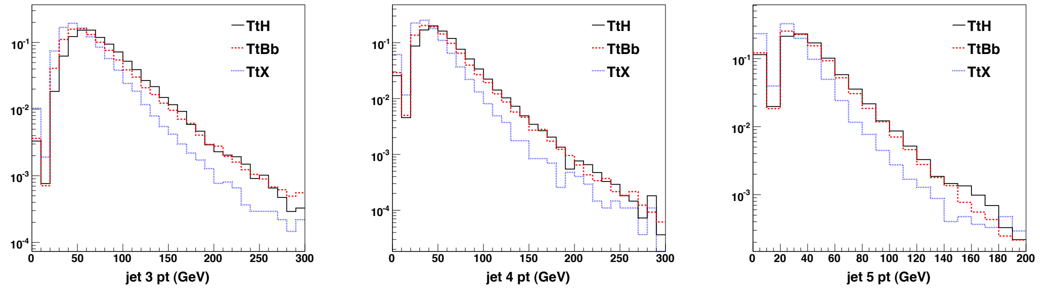

(c) 3_{rd} hardest jet p_T .

(d) 4^{th} hardest jet p_T .

(e) 5_{th} hardest jet p_T .

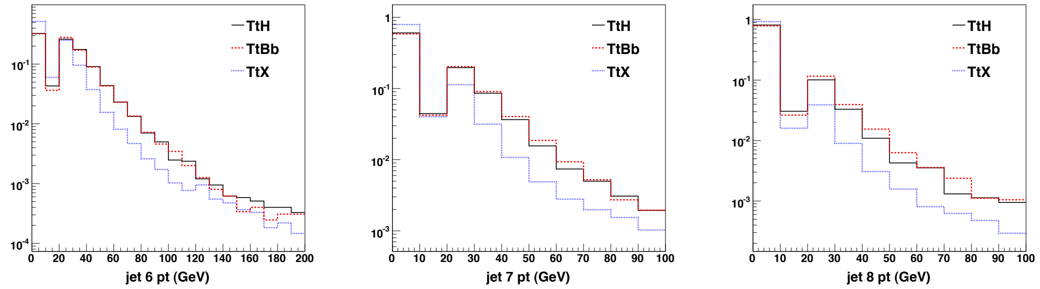

(f) 6^{th} hardest jet p_T .

(g) 7_{th} hardest jet p_T .

(h) 8^{th} hardest jet p_T .

Figure 5.3: Jet p_T distributions for the hardest and each subsequent jet in signal and background. The $t\bar{t}b\bar{b}$ sample in the (red) dashed histogram contains both the $t\bar{t}b\bar{b}(ew)$ and $t\bar{t}b\bar{b}(qcd)$ processes. No preselection cuts are applied to the events in these distributions.

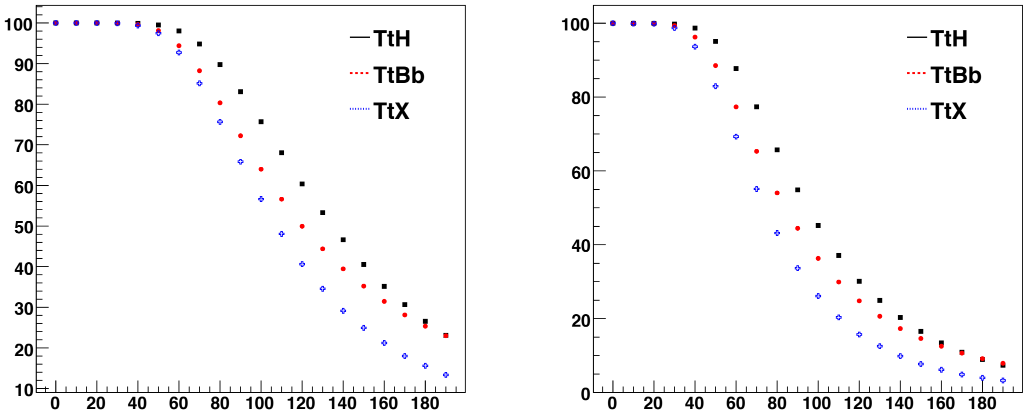

(a) Preselection efficiency as $f(\mathrm{p_T}$ cut) for the hardest jet.

(b) Preselection efficiency as $f(\mathrm{p_T}$ cut) for the 2^{nd} hardest jet.

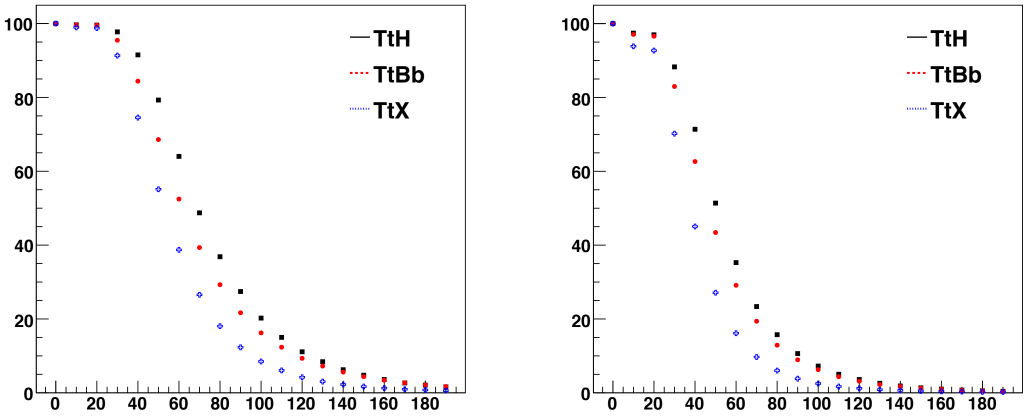

(c) Preselection efficiency as $f(\mathrm{p_T}$ cut) for the 3^{rd} hardest jet.

(d) Preselection efficiency as $f(\mathrm{p_T}$ cut) for the 4^{th} hardest jet.

Figure 5.4: Percentage of events passing individual jet $\mathrm{p_T}$ cuts for the hardest and each subsequent jet in signal and background. The $\mathrm{t\bar{t}b\bar{b}}$ sample in the (red) dashed histogram contains both the $\mathrm{t\bar{t}b\bar{b}(ew)}$ and $\mathrm{t\bar{t}b\bar{b}(qcd)}$ processes.

5.4 B-tagging

There are various flavor-tagging algorithms one can use to tag a jet's hadronic content as being light (originating from up, down or strange quark), charm or bottom. The basic principle is to assign a jet with a probability of containing heavy flavour decays, known as its b-weight, based on one or more criteria used to distinguish heavy from light flavour jets. The methods available for flavor-tagging jets are described in detail in[1]. The method utilised in this analysis uses a combination of significances calculated from the 3 dimensional (transverse+longitudinal) impact parameter and the secondary vertex, known as the IP3D+SV1 b-tagger.

5.4.1 Overview of methods for b-tagging

The most obvious technique is to use some form of **lifetime tag**, which makes use of the fact that B hadrons have a longer lifetime (~ 1.5 ps) than non-B hadrons. This is due to the high mass of the b quark in addition to the limited phase space for decay brought about by the low values of the CKM matrix elements $\mathrm{V_{cb}}$ and $\mathrm{V_{ub}}$, meaning that decay via any process is heavily suppressed. The consequence of this long lifetime means that a b quark will travel some distance (typically a few millimetres) in the detector before its subsequent decay.

Using the tracking detector one can reconstruct the primary vertex (PV) of the jet (the interaction point, z_0) and then look for secondary vertices within the jet, where a track appears to come not from the interaction point but from some other point along the jet axis. The transverse distance between the PV and track perigee is the (signed) transverse impact parameter, d_0. If the impact parameter is negative then the track originated at a point on the jet axis located *prior* to the PV, so there is no secondary vertex to be found. If d_0 is positive, then a secondary vertex exists. There are two kinds of secondary vertexing; two dimensional involving only the transverse impact parameter d_0, and three dimensional which also includes the longitudinal impact parameter z_0. The calculation of the transverse impact parameter is illustrated in Fig. 5.5[35]. In the two dimensional case the significance is then given as the impact parameter d_0 divided by its resolution $s_{d_0} = \frac{d_0}{\sigma_{d_0}}$.

Tracks from the decay of a B-hadron have an average $d_0 \sim 400 \mu m$. The resolution on d_0 is defined by the intrinsic spatial resolution of the inner detector, which is dependent on the $\mathrm{p_T}$ and direction of the track $\sigma(d_0) = 11 + \frac{60}{p_T}\sqrt{\sin\theta}$.

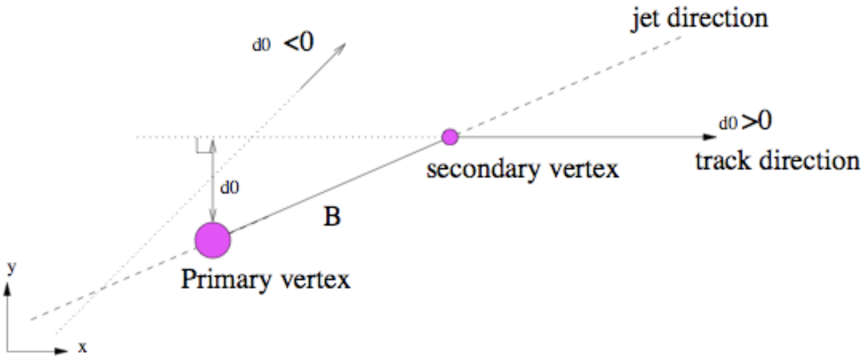

Figure 5.5: The signed transverse impact parameter d_0. Figure taken from[35].

Fig. 5.6(a) shows the d_0 distribution for b-jets, c-jets and light jets and the significance s_{d_0} is shown in Fig. 5.6(b) [1]. The impact parameter significance s_{d_0} is higher on average for tracks coming from b-jets than from light(uds) and gluon jets, and so can be used to distinguish between them.

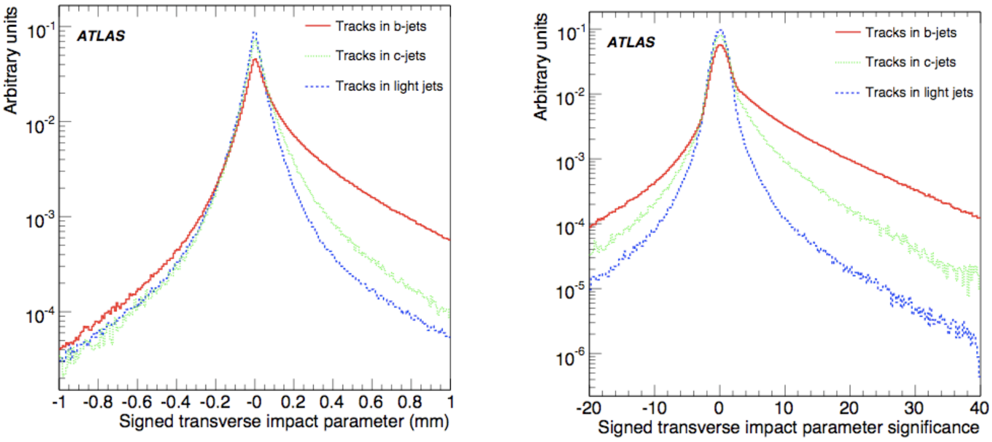

(a) Transverse impact parameter d_0 (b) Transverse significance s_{d_0}

Figure 5.6: The transverse impact parameter(a), and the significance (b). These distributions are used to calculate the IP3D b-weight. Figure from[1].

The IP3D b-weight of a jet is calculated by dividing the significance probability function for a b-jet by that for a light jet as shown in Eq. 5.3.

$$W_{jet}^{3D} = \sum_{i}^{N_{tracks}} ln\frac{b(s_{d0i}, s_{z0i})}{u(s_{d0i}, s_{z0i})} \tag{5.3}$$

The **secondary vertex** (SV) weight is calculated according to Eq. 5.4, where N is the number of two-track SVs, M is the mass of the SV and F is the fraction of the jet's energy contained in the SV. The distributions of these variables are shown in Fig. 5.7[1]. The probability distributions b(N,F,M) are obtained from calibration histograms of Monte Carlo data.

$$W_{jet}^{SV} = ln\frac{b(N, F, M)}{u(N, F, M)} \tag{5.4}$$

The IP3D+SV1 b-weight used for tagging jets in this analysis is then obtained by adding the weights from the IP and SV calculations, $W_{ip3d+sv1} = W_{jet}^{3D} + W_{jet}^{SV}$. This will be referred to simply as the b-weight from here on. The b-weight distributions of jets in the $\mathrm{t\bar{t}H^0}$ sample are shown in Fig. 5.8.

Soft lepton tagging is described extensively elsewhere[36], but basically relies on the semi-leptonic decay of B-hadrons. Although soft leptons are not used for b-tagging in this analysis, the principal behind the method is relevant to the technique used for calculating the jet charge, which is discussed in Sec. 5.5.1. The lepton produced in a $b \to cl\nu$ decay will, due to the high mass of the b quark, be produced over a larger range of directions transverse to the jet axis. Because of this, the $\mathrm{p_T}$ of the lepton relative to the jet direction (p_T^{rel}) will be higher on average than the p_T^{rel} of a lepton from some other source. The p_T^{rel} caculation is given in Eq. 5.5, where θ is the angle between the jet axis and the μ.

$$p_T^{rel} = p \times \sin\theta_{\mu-j} \tag{5.5}$$

5.4.2 Choosing a b-weight cut for $\mathrm{t\bar{t}H^0}$

When choosing a b-weight to cut on, one must consider the efficiency and purity of the tagging algorithm at that working point. The efficiency of a b-tagging

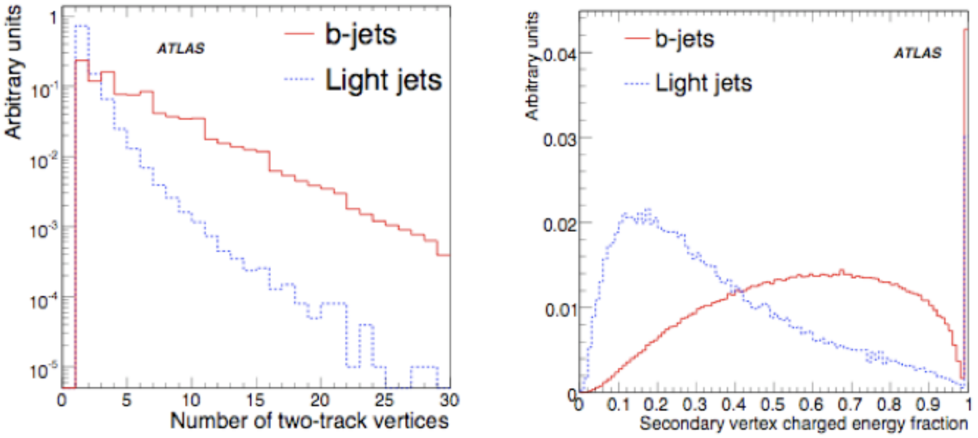

(a) Number of vertices (b) Energy fraction in vertex

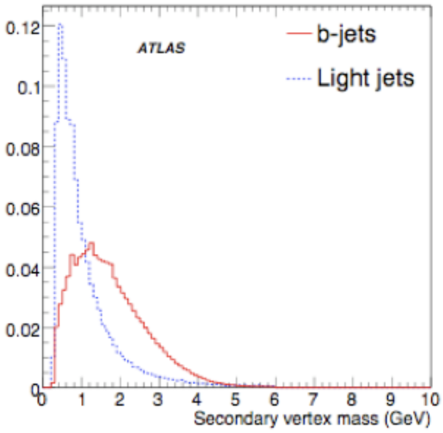

(c) Mass in vertex

Figure 5.7: The (a) Number of track pair vertices, (b) Fraction of jet's energy in vertex and (c) mass of vertex. These distributions are used to define the SV1 b-weight, W_{jet}^{SV}. Figure from[1].

algorithm is defined in Eq. 5.6 and the purity in Eq. 5.7.

$$\epsilon_b = \frac{\text{Number of jets tagged as b-jets}}{\text{Number of b jets}} \tag{5.6}$$

$$p_l = \frac{\text{Number of jets not tagged as b jets}}{\text{Number of light jets}} \tag{5.7}$$

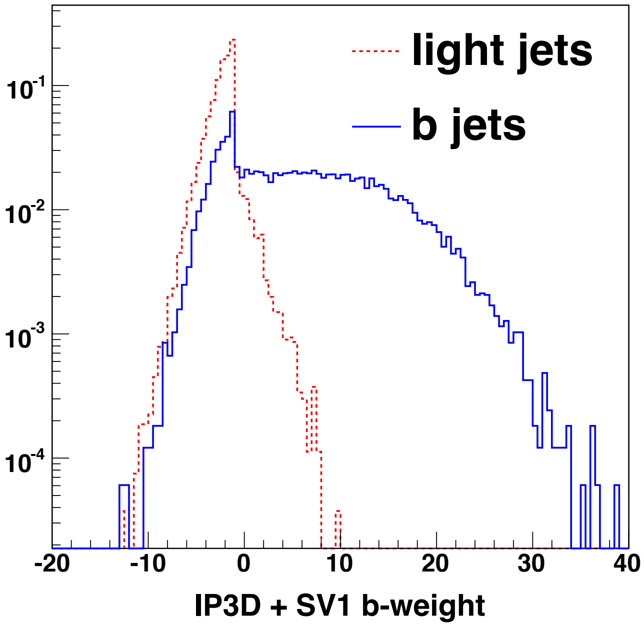

Figure 5.8: The IP3D+SV1 b-weight of b-jets (matched with $\Delta R \leq 0.3$ to b-quarks) and light jets (not matched to τ, b or c).

It is common for the light jet rejection to be used in place of the purity. The light jet rejection is the inverse of (1- purity), such that a rejection of 100 translates as one light jet in a hundred being mistagged as a b-jet.

Fig. 5.9 shows the efficiency versus purity for truth-matched b-jets in the $t\bar{t}H^0$ sample. Two different algorithms are used to reconstruct the jets, AntiKt and Cone, both with R=0.4. The b-tagging algorithm itself always uses a fixed cone with radius R=0.4 to define which tracks to use in the calculation of the jet b-weight. All tracks passing certain quality cuts and lying within this cone are considered in the calculation. It is interesting that jets made with the AntiKt algorithm appear to have a better light jet rejection than jets made with the Cone algorithm. Initially this was thought to be due to the better directional resolution of the AntiKt algorithm resulting in a slightly different jet direction, such that a slightly improved set of tracks was considered in the cone used for b-tagging. It is still felt that this may contribute a little to the difference in performance, but it is in fact considered more likely that the apparent improvement in purity when

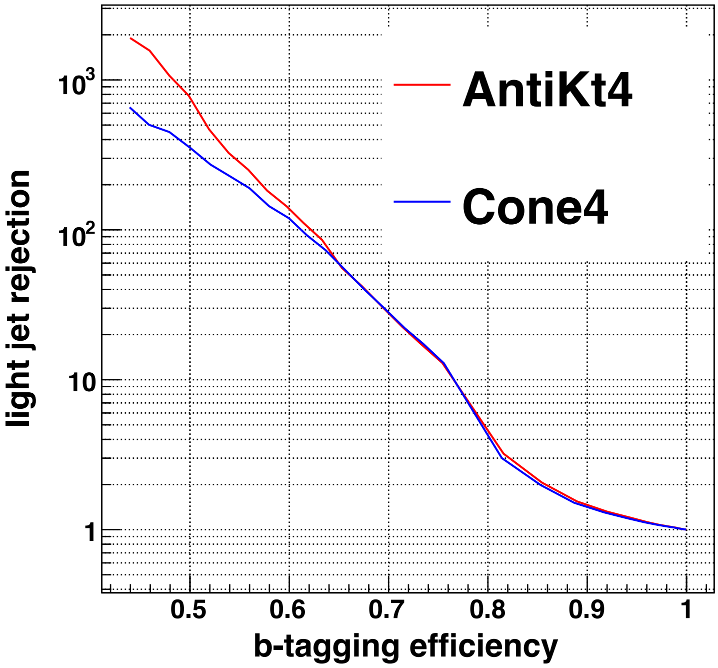

Figure 5.9: Light jet rejection versus B-tagging efficiency for $t\bar{t}H^0$ for jets made with the AntiKt and Cone algorithms.

moving to the AntiKt algorithm is a feature of the truth-matching procedure. Jets are labeled as light jets if they are not within $\Delta R \leq 0.3$ of a b, c or τ particle. Because Cone jets are a little larger than AntiKt jets for the same value of R (see Chapter (7) for an explanation of this), and also have slightly worse directional reconstruction, there is more chance that one may label a light jet as something else, thereby affecting the rejection as is observed here and in Fig. 5.12. What this means is that the actual b-tagging performance is not expected to differ much for the different algorithms in real data.

Fig. 5.10 shows the preselection efficiency as a function of b-weight cut for the signal and $t\bar{t}X$ background samples. The efficiency for the $t\bar{t}X$ background drops much more steeply than for the signal, even in the case of the two b-jets with the highest b-weights, which is somewhat surprising considering the $t\bar{t}X$ sample will always contain at least two b-jets from the top quark decays. The reason for this is that the b-jets from the tops are not always the jets with the highest b-weight. This is true for the $\mathrm{t\bar{t}H^0}$ sample too, but in those cases the events have four b-jets, so the two with the highest b-weight are much more likely to actually be true b-jets. The probability of the b-weight ordered jets being $\Delta\mathrm{R} \leq 0.3$ to a true b quark are shown in Table. 5.1 for the signal and the $\mathrm{t\bar{t}X}$ background.

Order in b-weight	% true b ($\mathrm{t\bar{t}X}$)	% true b ($\mathrm{t\bar{t}H^0}$)
1^{st}	89.8	97.7
2^{nd}	58.1	89.8
3^{rd}	14.8	67.9
4^{th}	6.6	36.8

Table 5.1: The probability for each jet to be matched to a true b quark for the b-weight ordered jets.

As the cross-section for $\mathrm{t\bar{t}X}$ exceeds that for $\mathrm{t\bar{t}H^0}$ by a factor three orders of magnitude, it is useful to look at the preselection efficiencies scaled by the realtive cross-section. Fig. 5.11 shows the (efficiency $\times$ scale factor) as a function of the b-weight cut applied to the jet with the 4^{th} highest b-weight, where the scale factor is 1 for $\mathrm{t\bar{t}H^0}$ and 888 for $\mathrm{t\bar{t}X}$. A b-weight cut of 2.5 is chosen to be optimal for this analysis. This cut reduces the large $\mathrm{t\bar{t}X}$ background by a factor ≥ 100 while retaining enough signal to be able to work with.

5.4.3 Systematic uncertainties on flavour tagging

There are two important systematics to be considered when using b-tagging in an analysis: the uncertainties on the b-tagging efficiency and on the mis-tag rate.

The recommended systematic uncertainty on the b-tagging efficiency as provided by the ATLAS flavour-tagging experts is estimated to be 5%[1]. There has as yet been no ATLAS study to determine the systematic error on the mistag rate. The current recommendation is 10%, based on experience with the Tevatron.

In order to determine the systematic uncertainty on the significance of this channel due to the systematic errors on the mistag rate and b-tagging efficiency,

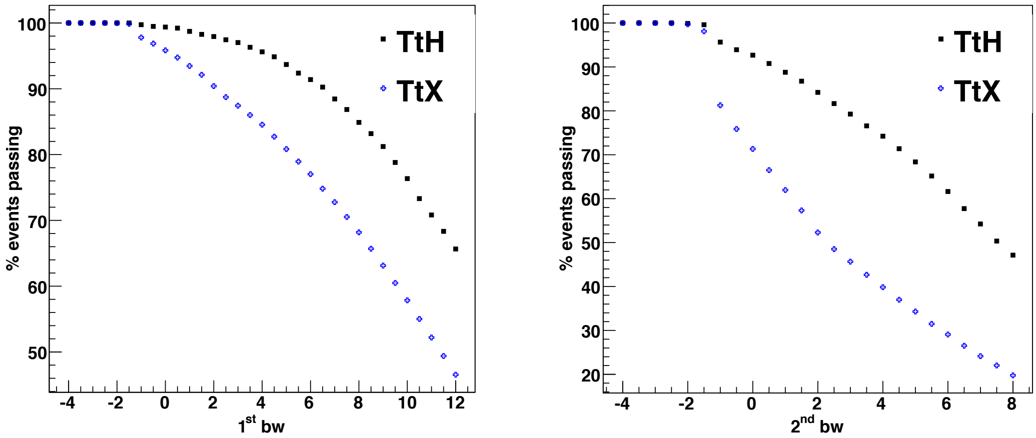

(a) highest b-weight jet (b) 2^{nd} highest b-weight jet

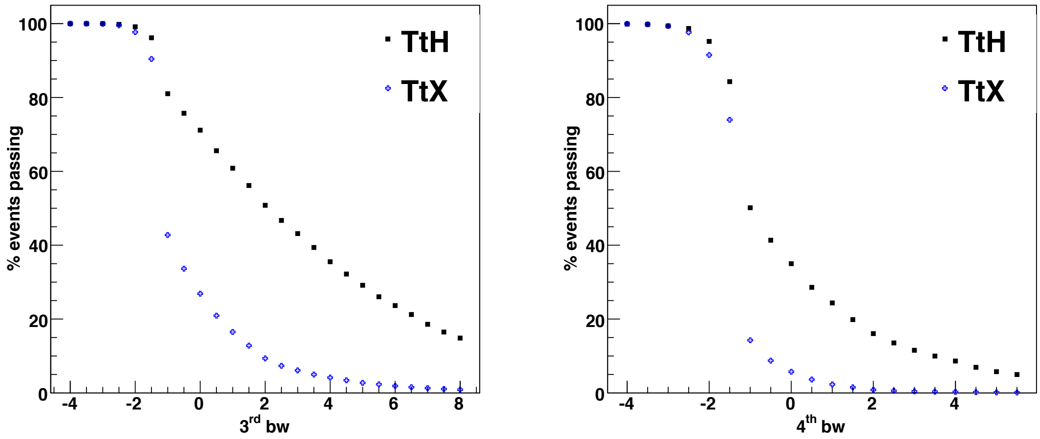

(c) 3^{rd} highest b-weight jet (d) 4^{th} highest b-weight jet

Figure 5.10: Percentage of events passing individual jet b-weight cuts for the highest b-weight jet and each subsequent jet in signal and $\mathrm{t\bar{t}X}$ background.

the b-weight is varied separately such that it produces a $\pm 5\%$ change in efficiency and a $\pm 10\%$ change in mistag rate. Fig. 5.12 shows the b-tagging efficiency as a function of the b-weight cut applied in $\mathrm{t\bar{t}H^0}$ signal events. This is shown for two jet definitions: AntiKt and ATLAS Cone, both with R=0.4. The uncertainties shown are with respect to AntiKt4 jets.

The variation in b-weight needed to produce a 5% change in the b-tagging

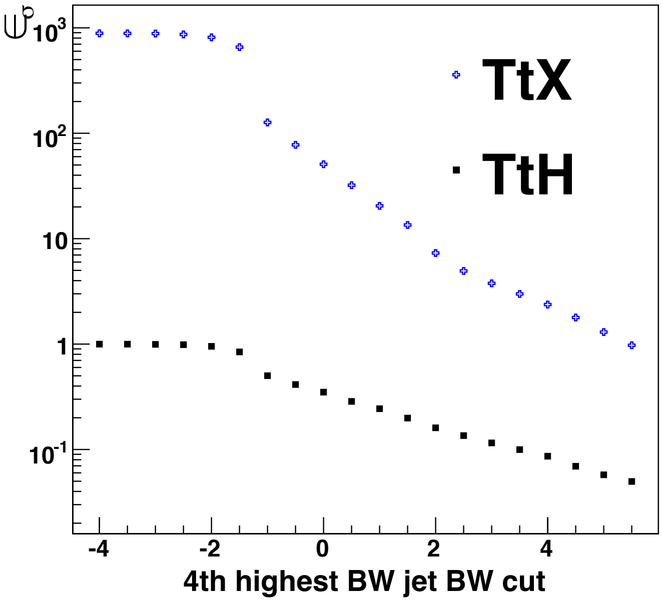

Figure 5.11: Preselection efficiency ϵ multiplied by cross-section scale factor $_\sigma$ as a function of the b-weight cut applied to the jet with the 4^{th} highest b-weight.

efficiency is a function of the jet's b-weight. The values chosen for Fig. 5.12 are shown in Table. 5.2. Around the cut region of 2.5 a variation of b-weight ± 0.8 produces the 5% variation in efficiency.

b-weight range	+ variation	- variation
$bw < -3.$	0.8	0.8
$-3. < bw < -2.$	0.5	0.5
$< -2. < bw < -1.$	0.3	0.3
$bw > -1.$	**0.8**	**0.8**

Table 5.2: b-weight adjustments for $\Delta\epsilon_B$ of 5%.

The variation in b-weight needed to produce a 10% change in the light jet rejection is also a function of the jet's b-weight. The values chosen for Fig. 5.13 are shown in Table. 5.3. Around the b-weight cut of 2.5 a b-weight variation of ± 0.3 gives the recommended 10% variation in light jet rejection.

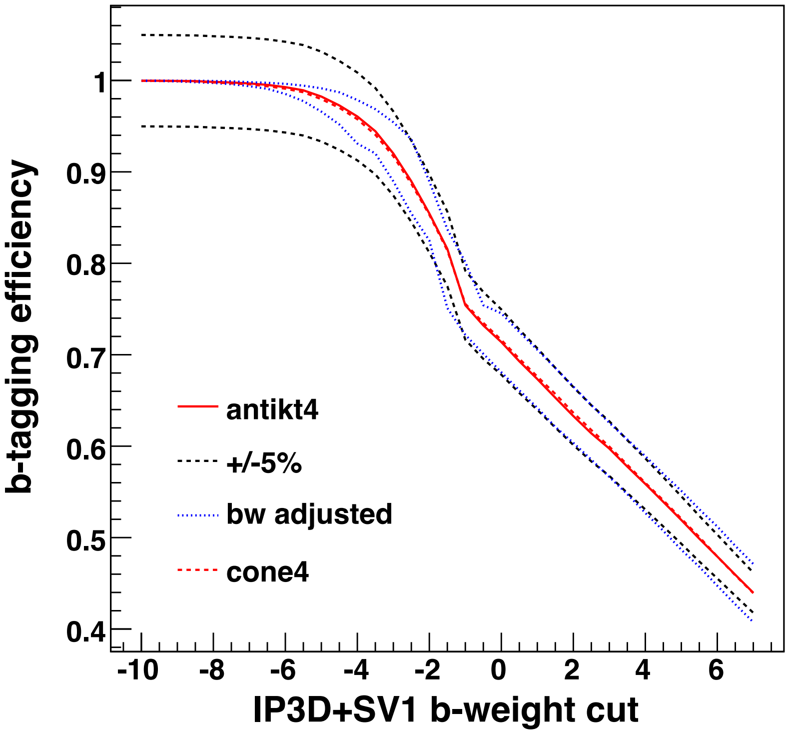

Figure 5.12: B-tagging efficiency for $t\bar{t}H^0$ as a function of the b-weight cut for $t\bar{t}H^0$ for jets made with the AntiKt and Cone algorithms. The black dashed lines show the efficiency varied by 5%. The dotted blue lines show the efficiency when the b-weight is varied by ± 0.8.

These variations also give the same recommended b-weight efficiency and light jet rejection variations for b-weight cuts between -1 and 6.

b-weight range	+ variation	- variation
$bw < -2.5.$	0.3	0.3
$-2.5 < bw < -2.$	0.2	0.3
$< -2. < bw < -1.5$	0.1	0.3
$-1.5 < bw < 1 - .$	0.1	0.1
$-1. < bw < 0.5$	0.3	0.1
$bw > 0.5$	**0.3**	**0.3**

Table 5.3: b-weight adjustments for ΔR_{lj} of 10%.

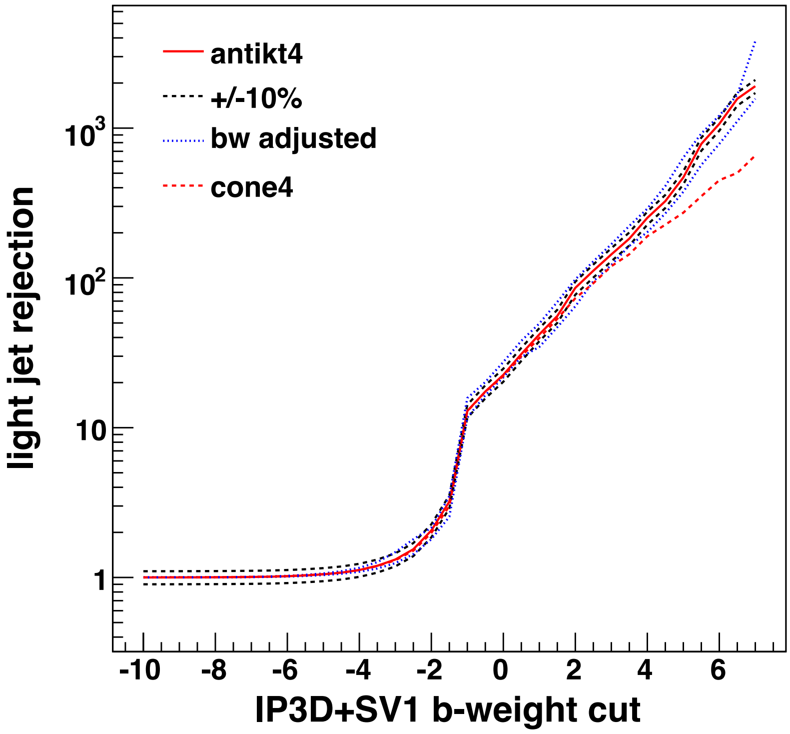

Figure 5.13: Light jet rejection as a function of the b-weight cut for $t\bar{t}H^0$ for jets made with the AntiKt and Cone algorithms.

5.5 Jet Combinatorics

Due to the busy and complex final state of a $t\bar{t}H^0$ event, there is a strong possibility that the event will be incorrectly reconstructed.

An event passing the $t\bar{t}H^0$ preselection will contain at least 6 jets, and may contain up to ~ 20. The jet multiplicities for the signal and background processes passing preselection are shown in Fig. 5.14. Many of the jets are the result of initial and final state radiation (ISR/FSR) and are therefore quite soft compared to the hard process jets. Fig. 5.15 shows the number of soft jets for the signal and background processes. This is of interest as it provides a possible method of discriminating between the jets needed for final state reconstruction and those from ISR/FSR, which contribute to the combinatorial background.

For an event containing n jets, the number of possible ways one can combine

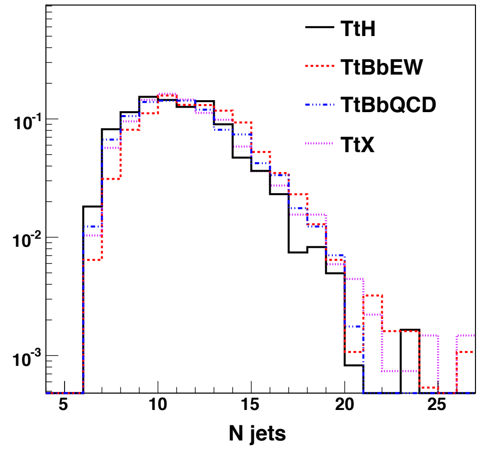

Figure 5.14: Number of jets in events passing preselection cuts.

k jets is given by the binomial theorem for combinations Eq. 5.8.

$$C_k^n = \frac{n!}{k!(n-k)!} \tag{5.8}$$

The combinatorics can be very large for these events ($\hat{n} \sim 12$, k=2 for W_{jj} reconstruction). This can result in a high probability of reconstructing the final state incorrectly. The requirement that the W_{jj} must lie within a window around the nominal W mass (80.4 GeV) is beneficial in removing some of the candidates, but it is dangerous to cut too hard on the mass of the W because this leaves us heavily reliant on the jet energy scale (see Eq. 5.2). The same argument applies for the reconstruction of the $t\bar{t}$ system. For this reason, other techniques besides mass cuts are considered for reducing the number of W_{jj} and $t\bar{t}$ candidates.

5.5.1 Jet Charge

One possible method for reducing the combinatorial background associated with W_{jj} and $t\bar{t}$ reconstruction is the use of jet charge. The charge of the trigger lepton in an event passing $t\bar{t}H^0$ event selection is known, so this information can be used to determine whether the top or anti-top quark decays semi-leptonically. Fig. 5.16 shows the charge conservation in a $t\bar{t}H^0$ event.

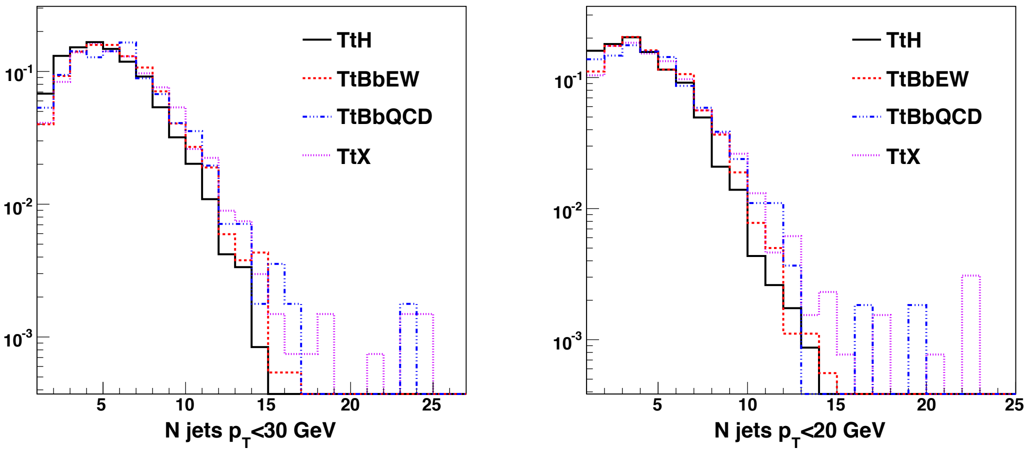

(a) Number of jets with $p_T \leq 30GeV$ (b) Number of jets with $p_T \leq 20GeV$

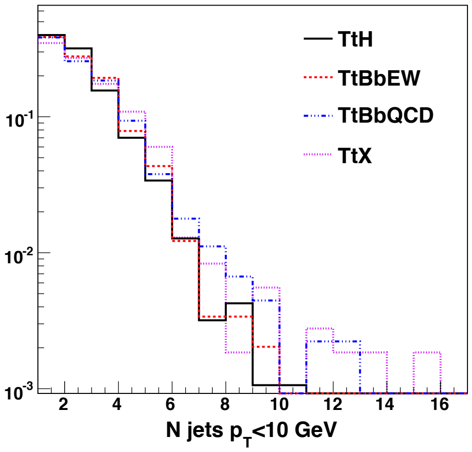

(c) Number of jets with $p_T \leq 10GeV$

Figure 5.15: Soft jet multiplicity in events passing preselection, in different $\mathrm{p_T}$ regions.

A jet is expected to carry the charge of the associated B-hadron rather than the fractional charge of the quark, as illustrated in Fig. 5.17. The summed charge of all the tracks in b-jets should however give a negative or zero charge while the charge of a $\bar{\mathrm{b}}$-jet should be positive.

The method of using the weighted charge of all tracks associated within a jet has been used previously at theTevatron experiment[37] in efforts to determine

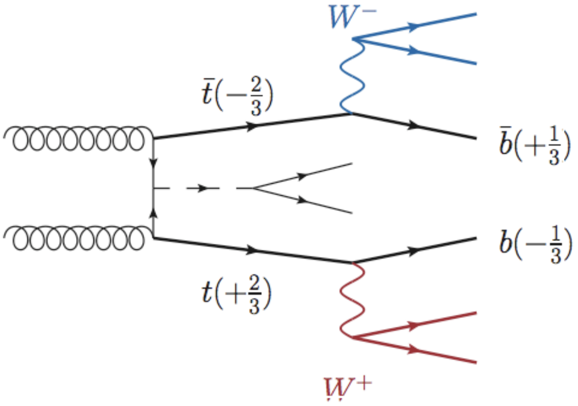

Figure 5.16: Charge conservation in $\mathrm{t\bar{t}H^0}$.

the charge of the top quark. Eq. 5.9 shows how the jet charge is calculated using the weighted sum of the charge of all tracks associated with the jet. $|p_i \cdot \hat{n}|$ is the component of track i's momentum along the direction of the jet axis, q_i is the charge of track i and κ is a variable weight. Higher values of κ give more weight to harder tracks.

$$Q_\kappa = \frac{\sum_i q_i |p_i \cdot \hat{n}|^\kappa}{\sum_i |p_i \cdot \hat{n}|^\kappa} \tag{5.9}$$

There are two separate ways in which one might use jet charge to reduce combinatorics in a $\mathrm{t\bar{t}H^0}$ event. One way is to calculate the charge of the $\mathrm{W_{jj}}$ candidates by summing the charge of the pair of jets used in its reconstruction and to compare this with the actual $\mathrm{W_{jj}}$ charge, which is established from the charge of the trigger lepton.

The other way to utilise jet charge information is in the reconstruction of the $\mathrm{t\bar{t}}$ system; the charge of the b-jet used for the reconstruction of the $\mathrm{t_{bjj}}$ multiplied by the sign of the trigger lepton should always be positive, whereas the oppposite is true for the b-jet used to reconstruct the $\mathrm{t_{bl\nu}}$. The charge of the $\mathrm{W_{jj}}$ multiplied by the lepton sign should always be negative. Fig. 5.18 shows the charge distributions for correct and incorrect reconstruction for the three

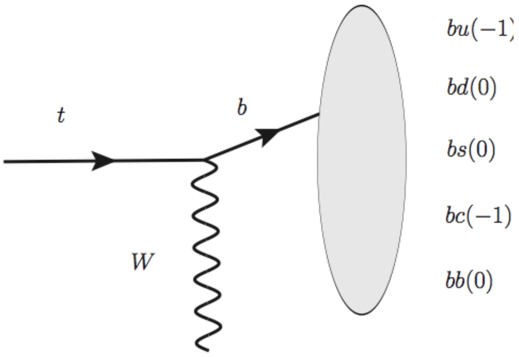

Figure 5.17: B-hadron production.

composite objects with a κ value of 0.5.

Another possible method for calculating the charge of semi-leptonically decaying b-jets is using the charge of a muon identified as being within the jet. There are some difficulties associated with this method due to the possibility of cascade decays producing a muon with the opposite sign charge to that of the b-jet Fig. 5.19(a) as well as the chance of the same occurrance due to the apparent oscillation between b and $\bar{\mathrm{b}}$ illustrated in Fig. 5.19(b). Despite these issues muons with high $\mathrm{p}_{\mathrm{T}}^{\mathrm{rel}}$ often reproduce the jet charge accurately and muons are not prolifically faked (which is unfortunately the case for electrons, thus making them unhelpful in this calculation). Fig. 5.20 shows the true and fake constituent lepton multiplicity in b-jets.

The probability of a muon having the right sign charge as a function of its $\mathrm{p}_{\mathrm{T}}^{\mathrm{rel}}$ is shown in Fig. 5.21(a). The clear correlation between a muon having high $\mathrm{p}_{\mathrm{T}}^{\mathrm{rel}}$ and carrying the correct sign charge is used as a weight for the muon charge, such that a much improved weighted muon charge can be used to calculate the charge of the b-jet. The muon charge before and after weighting is shown in Fig. 5.21(b). The weighted muon charge is very successful in reproducing a b-jet charge of the right sign, but it should be remembered that this method can only be used for semi-leptonically decaying b-jets where the decay is via $b \to c\mu\nu_\mu$. Around 18% of b decays proceed via this mode, leaving the majority of

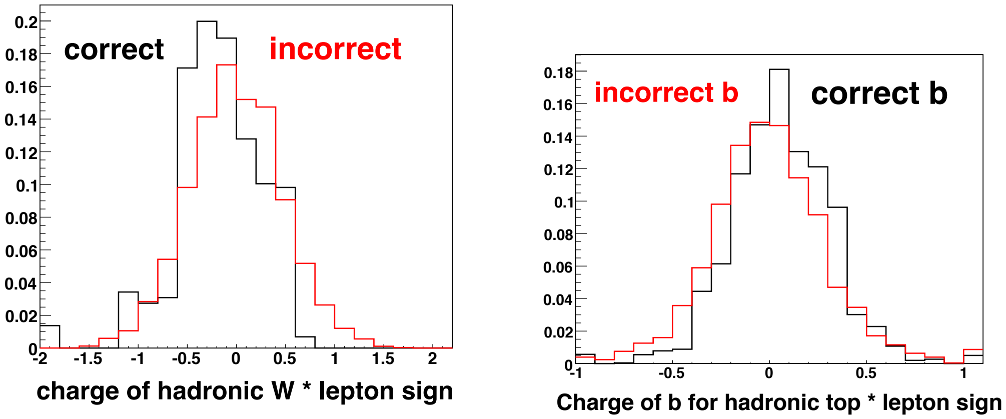

(a) W_{jj} charge * lepton charge (b) t_{bjj} charge * lepton charge

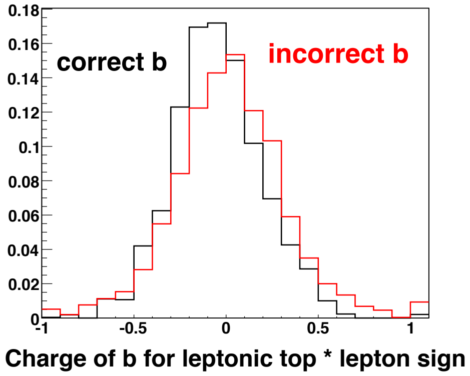

(c) $t_{bl\nu}$ charge * lepton charge

Figure 5.18: Weighted jet charge multiplied by trigger lepton charge for the reconstructed W_{jj} and top quarks

b-jet charge calculations to be dealt with using the weighted jet charge method discussed previously.

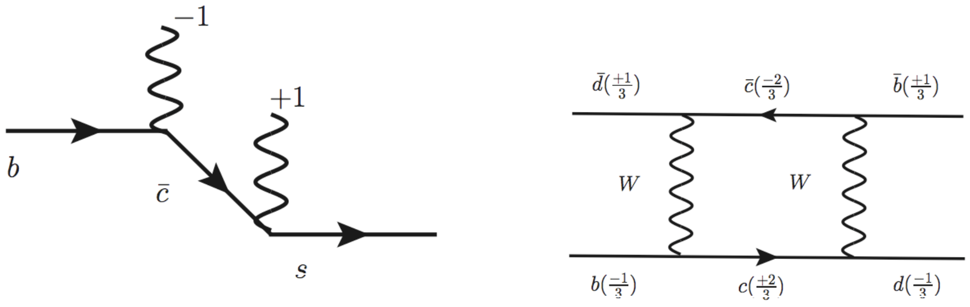

(a) A b-quark undergoing a semi-leptonic 'cascade' decay.

(b) Apparent charge oscillation of a b-jet.

Figure 5.19: The difficulties associated with calculating b-jet charge due to flavour-changing weak decays within the jet.

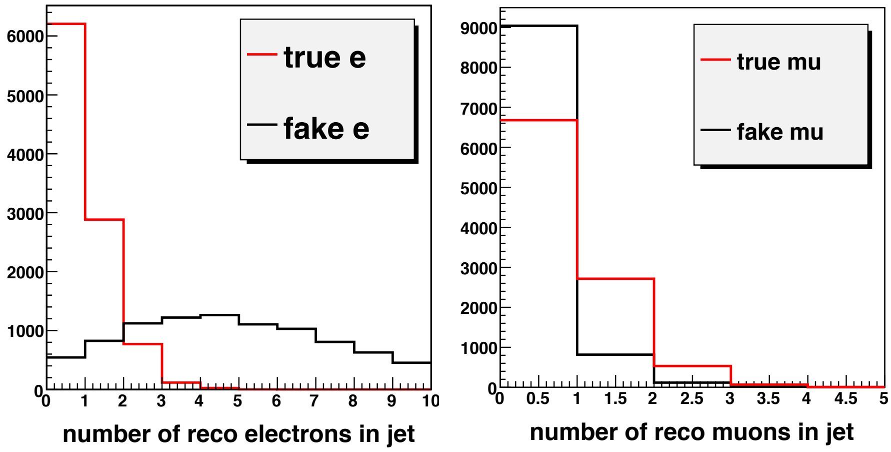

Figure 5.20: Constituent lepton multiplicity within b-jets. True leptons are ΔR matched within 0.1 of a lepton from the truth record.

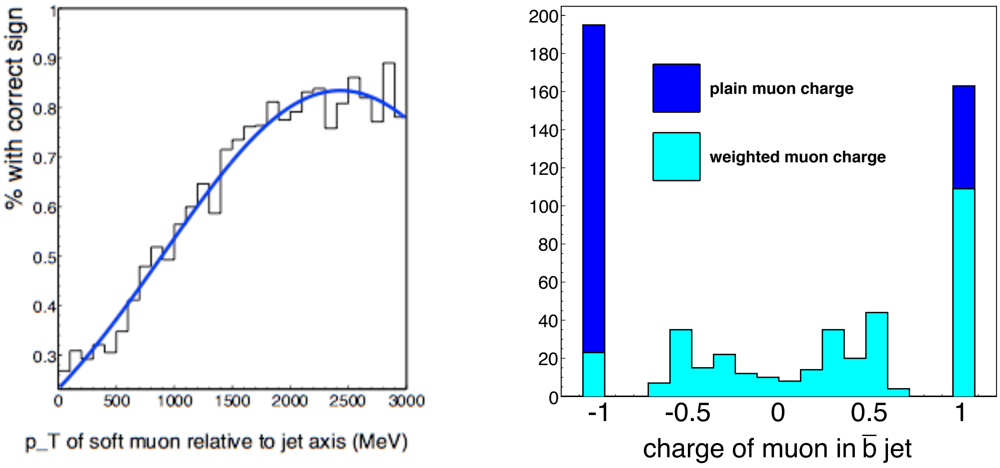

(a) Probability of correct muon charge as f(p_T^{rel}).

(b) Muon charge weighted by p_T^{rel}.

Figure 5.21: Soft muon charge method for b-jet charge determination.

Chapter 6

Jet Algorithms

At the LHC the energy scale will be $O(10\text{TeV})$. This means that there will be jets at energies and multiplicities not previously observed, and in addition many of the jets seen will be from the decay of particles with masses at the scale of electroweak symmetry breaking, such as the $\mathrm{W}^{\pm}$, Z^{0} and Higgs Bosons. Sometimes such highly boosted particles may have close to collinear decay products such that we see a single jet from one of these electroweak Bosons or from the top quark decay. There will also be events that include jets coming from several different hard scales, and large amounts of soft QCD radiation everywhere.

It is of utmost importance to have a stable and reproducible jet definition and to have jet algorithms that are excellent at picking out hard physics and can run fast even with very high occupancy.

6.1 Jet finding algorithms

A jet definition consists of an algorithm, its parameters (usually a distance parameter, R, used to determine whether objects belong in the same jet or not) and a recombination scheme which determines the calculation of the jet's momentum from its constituent objects. The recommended recombination scheme is the 'E-scheme' or 4-vector recombination scheme, and is used for all the jet algorithms in this study. This scheme simply adds the 4-vectors of all constituent objects in the jet. The fundamental requirements of a jet definition, agreed upon in 1990 and known as the *Snowmass accord*[38], are as follows:

1. Simple to implement in experimental analysis.
2. Simple to implement in theoretical calculations.
3. Defined at any order of perturbation theory.
4. Yields finite cross section at any order of perturbation theory.
5. Yields a cross section that is relatively insensitive to hadronisation.

6.1.1 Cone algorithms

The ATLAS Cone algorithm is an iterative cone (IC), meaning that it is initiated by a seed, along with most of the cone algorithms currently in use. The procedure is as follows:

- A seed particle i sets a direction $\hat{i}$.
- A circle of radius R is drawn around the direction $\hat{i}$ in the y, ϕ plane, where y is the rapidity and ϕ is the azimuthal angle perpendicular to the beam.
- The momenta of all particles j that satisfy $\Delta\mathrm{R}_{\mathrm{ij}}^2 = (\mathrm{y}_i - \mathrm{y}_j)^2 + (\phi_i - \phi_j)^2 < \mathrm{R}^2$ are summed.
- The direction of the summed momenta $\hat{p}$ is set as the new seed direction.
- The process continues until the cone is stable.

All particles, calorimeter towers or topoclusters (topological clusters) having energy above a certain threshold $\mathrm{E}_{\mathrm{seed}}$ (typically 1-2 GeV) are taken as seeds, meaning that there can be many overlapping ‘protojets’ as a result of this procedure. The ATLAS cone algorithm uses a split-merge approach (SM) to separate the overlapping protojets. A pair of protojets is merged if the softer protojet in the pair shares more than a fraction f of its transverse momentum with the harder protojet of the pair. If the softer protojet shares less than f of its

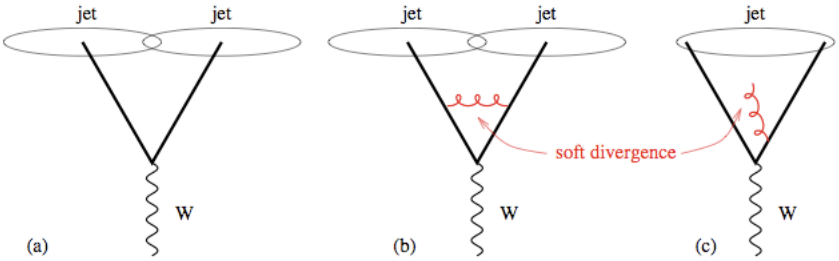

Figure 6.1: Infrared safety. In the case of a W_{jj} decay the addition of an infinitely soft gluon results in the two jets being merged into one. Figure taken from[39].

transverse momentum with the harder protojet then the particles are simply assigned to their nearest protojet. The fraction f is typically 0.75.

A major problem with split-merge seeded cone algorithms such as the ATLAS cone is that they are not infrared safe. The concept of infrared safety is illustrated in Fig. 6.1. The presence of soft ('infrared') radiation between two stable cones can cause them to be merged into a single jet.

Experimental results found using a jet algorithm that is vulnerable to these divergences makes it difficult to test theoretical predictions past leading order. For an event such as $t\bar{t}H^0$ or $t\bar{t}$, there is no meaningful order with which one make measurements using an infrared or collinear unsafe jet algorithm.

The recent development of the SIS (Seedless Infrared-Safe) cone algorithm removes the issues of soft and collinear divergences by finding all stable cones without the use of seeds. The procedure is of defining distinct cones based on their particle content. With SIScone it has been shown to be possible to find all possible stable cones while remaining infrared and collinear safe. The SIScone algorithm is described in detail in[40]. Like the ATLAS cone algorithm, SIScone relies on the split-merge procedure to separate overlapping cones into distinct jets.

6.1.2 Cluster Algorithms

Cluster algorithms (also known as sequential recombination algorithms) work by defining two distances associated to every object (particle/energy deposit) and finding the smaller of the two. The two distances are the distance between the object and its closest neighbour, defined in Eq. 6.1 and the distance between the object and the beam, defined in Eq. 6.2.

$$\delta_{ij} = min(k_{ti}^{2p}, k_{tj}^{2p})\left(\triangle y_{ij}^2 + \triangle\phi_{ij}^2\right) \tag{6.1}$$

$$\delta_{iB} = R^2 k_{ti}^{2p} \tag{6.2}$$

If $\delta_{iB} < \delta_{ij}$ then the object is closer to the beam than it is to any other energy deposit in the event, so it is defined as a jet and removed from the event.

If $\delta_{iB} > \delta_{ij}$ then the two objects i and j are combined into one. This procedure continues until there are no objects remaining in the event.

The p value in Eq. 6.1 and Eq. 6.2 (the exponent of the transverse momentum scale) can take on the values of $-1, 0, +1$, corresponding to AntiKt, Cambridge-Aachen and inclusive Kt algorithms respectively.

The jet algorithms considered in this study are the ATLAS cone[2], SIScone[40], AntiKt[41] and Kt[42]. A comprehensive introduction to jet finding algorithms can be found in[43] and[39].

6.2 Performance in $\mathrm{t\bar{t}H^0}$

A $\mathrm{t\bar{t}H^0(H^0 \rightarrow b\bar{b})}$ signal event is characterised by a final state with a high jet multiplicity, and the successful reconstruction of the $\mathrm{t\bar{t}H^0}$ system relies on being able to correctly identify all six final state jets, to b-tag them correctly, and to have good enough four-momenta reconstruction to be able to reconstruct the hadronically decaying W Boson and both top quarks within mass windows of ~ 25 GeV. It is difficult to imagine a channel more reliant on excellent jet reconstruction in a highly complex and busy environment. The study presented in this chapter shows how the $\mathrm{t\bar{t}H^0}$ signal reconstruction efficiency is affected by changing the jet algorithm used. Four different algorithms are studied; the ATLAS cone, which is the algorithm used as standard in most previous analyses [1], the Seedless Infrared-Safe SISCone, and the Kt and AntiKt algorithms.

The performance of each jet algorithm in the context of $\mathrm{t\bar{t}H^0(H^0 \to b\bar{b})}$ reconstruction is examined with 'TruthJets', where TruthJets are reconstructed directly from the four vectors of generated hadrons. The comparison between truth particle and TruthJet makes this study detector-independent, enabling a clear examination of the different jet algorithms' performance.

Each jet algorithm is run 16 times, each time with a different R parameter (cone radius for the cone-type algorithms) varying between 0.3 and 0.6. The jet algorithms' performances are assessed for every aspect of event reconstruction, first on the full signal sample (with no event selection applied) and then after the event selection as implemented in the CSC study.

6.2.1 Algorithm requirements

There are several jobs a jet finder must do well in order to be considered suitable for selecting and reconstructing $\mathrm{t\bar{t}H^0}$ events:

1. We would ideally like to reconstruct all six final state quarks as jets, with $\Delta R_{jet-quark} \leq 0.1$
2. We would like to reconstruct as few 'other' jets as possible (i.e. gluon jets, quark jets with $\Delta R_{jet-quark} \geq 0.1$)
3. We would like a good jet p_T resolution.
4. We would like efficient b-tagging.

The first part of this study (Sec. 6.3 to Sec. 6.5) is to qualify the jet algorithms' performance on the full signal sample, without applying any cuts relating to the $\mathrm{t\bar{t}H^0}$ analysis. The efficiencies obtained for jet preselection and final state reconstruction are discussed in Sec. 6.6.

6.3 Jet reconstruction efficiency

A first step to determining the efficiency of an algorithm is to look at how many of the final state quarks it reconstructs as jets. Fig. 6.2(a) shows the mean number of final state quarks matched to a reconstructed TruthJet, where the matching criteria is $\Delta R_{\text{jet}-\text{quark}} \leq 0.1$. The overall aim of the $\mathrm{t\bar{t}H^0}$ analysis is to reconstruct a Higgs Boson out of the correct pair of b-jets; thus one wishes at the very least to be able to find these jets in the first place. It is preferable, however, to find jets corresponding to all the final state quarks $(\mathrm{b_H,\bar{b}_H,b_t,\bar{b}_t,q_W,\bar{q}_W})$, as the $\mathrm{W_{jj}}$ and $\mathrm{t_{bjj}}$ must be reconstructed within their mass windows in order for the analysis to continue as far as attempting Higgs reconstruction. The k_T-type algorithms clearly perform better when it comes to finding all the jets needed for final state reconstruction, as can be seen in Fig. 6.2 and Fig. 6.3.

Another important factor in correctly reconstructing the Higgs is finding a way to deal with the combinatorial background that arises from having a large number of jets with which to choose from to reconstruct the final state objects. Fig. 6.2(b) shows the mean number of ‘other’ jets per event as a function of the jet algorithms’ R parameter. By ‘other’ jets we mean either quark jets reconstructed with $\mathrm{\Delta R_{jet-quark}} \geq 0.1$, or gluon jets. We would ideally like to minimise this number in order to reduce the combinatorial background that makes correct event reconstruction so difficult. The AntiKt algorithm achieves the lowest number of ‘other’ jets over the whole range of R. Fig. 6.3 shows the fraction of events in which the full set of $(\mathrm{b_H,\bar{b}_H,b_t,\bar{b}_t,q_W,\bar{q}_W})$ are matched to TruthJets. This plot indicates that the AntiKt algorithm with a small R-parameter is superior to the other algorithms at fully reconstructing the final state. The fraction of events fully matched is always $\leq 8\%$; with all of the jet algorithms studied there is a very low efficiency for matching reconstructing 6 jets and matching them within $\mathrm{\Delta R_{jet-quark}} \geq 0.1$ to generated particles (which can have very small angular separations).

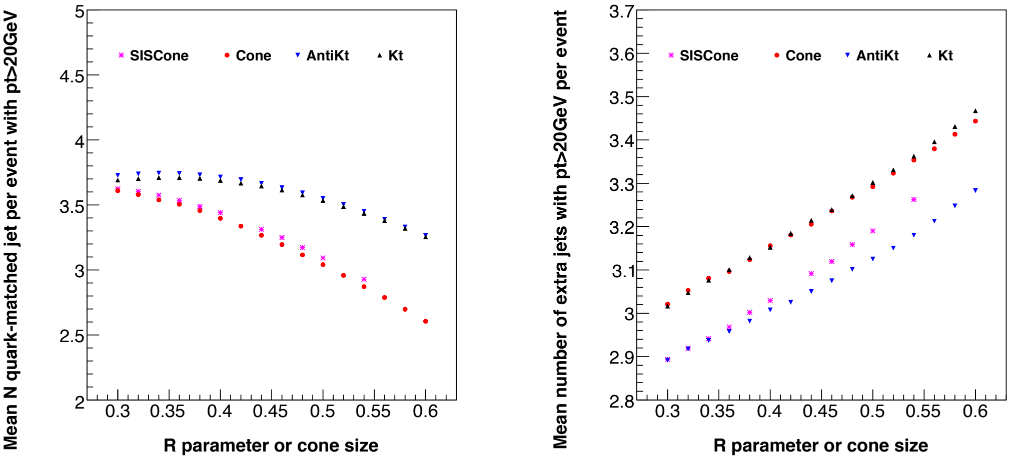

(a) Mean number of matched jets per event.
(b) Mean number of ‘other’ jets per event.

Figure 6.2: Efficiency for matching final state quarks to jets in full $\mathrm{t\bar{t}H^0}$ sample.

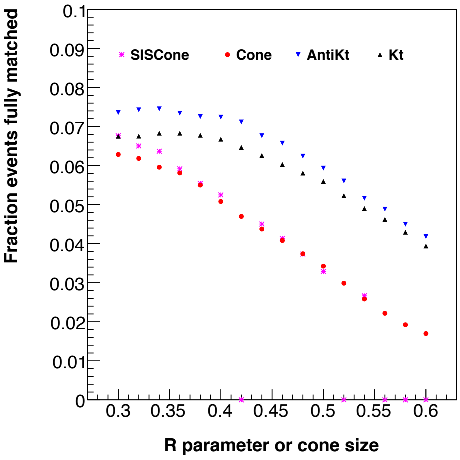

Figure 6.3: Fraction of events in which all 6 quarks are matched within $\Delta R \leq 0.1$ to jets in full $\mathrm{t\bar{t}H^0}$ sample.

6.4 $\mathrm{p_T}$ resolution

A TruthJet is the result of running a jet algorithm on truth particles rather than on calorimeter clusters/towers. The TruthJet resolution is therefore dependent on the hadronisation model used in the event generation.

The excellent $\mathrm{p_T}$ resolutions shown in Fig. 6.4 are a consequence of the requirement that all the jets are closely ($\Delta R \leq 0.1$) matched to quarks. A jet's directional resolution is of course correlated to its $\mathrm{p_T}$ resolution, meaning that these jets have a better resolution than one would normally expect with a sample of jets having a looser matching criteria.

The large tail in Fig. 6.4(a) is present for the whole range of R parameters, signifying that it is not caused by particles lost outside the jet area, but by particles not considered when making the TruthJet. The particles not used in the making of a TruthJet are neutrinos and muons, which may carry quite a large fraction of the jet's energy if the b-quark decays semi-leptonically, as discussed in Sec. 5.2. The tail is much less pronounced in the case of light jets, Fig. 6.4(b). This is expected because light quarks do not decay into muons.

The TruthJet $\mathrm{p_T}$ resolution as a function of R-parameter is shown in Fig. 6.5. There is clearly an improvement in jet $\mathrm{p_T}$ reconstruction with increasing R. This is expected, as a larger value of R will pull in more radiation, increasing the reconstructed $\mathrm{p_T}$.

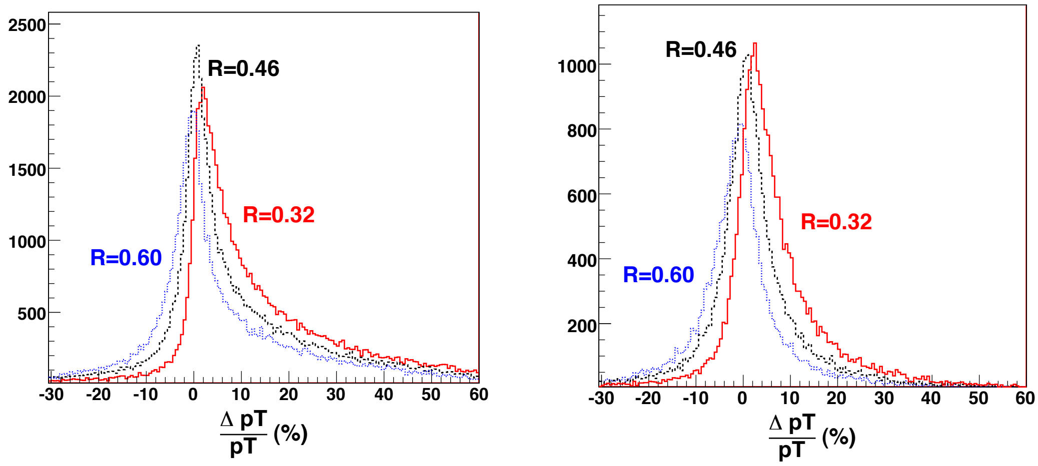

(a) b-matched jets.

(b) udsc-matched jets.

Figure 6.4: $\frac{\Delta \mathrm{p_T}}{\mathrm{p_T}}$ for AntiKt TruthJets with R=0.32, 0.46 and 0.60.

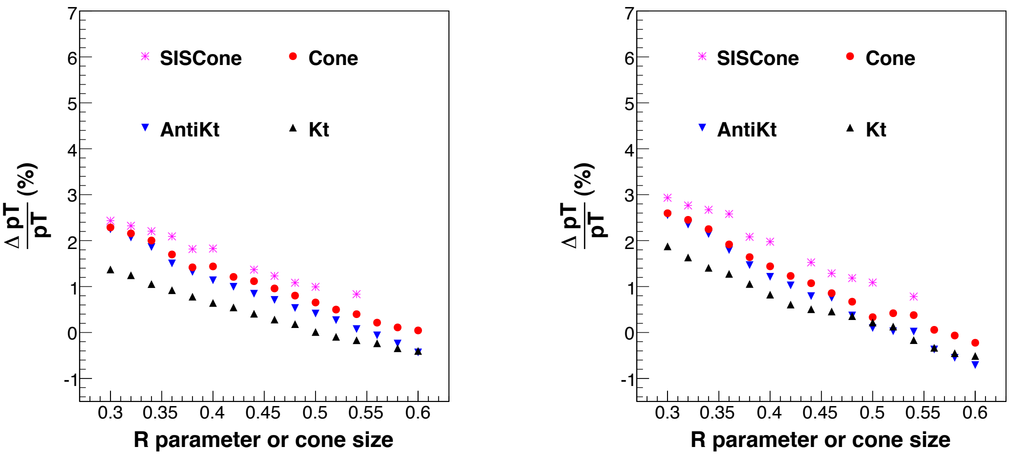

(a) b-matched jets.

(b) udsc-matched jets.

Figure 6.5: The mean $\frac{\Delta \mathrm{p_T}}{\mathrm{p_T}}$ versus R for quarks with $\mathrm{p_T} \geq 50$ GeV.

6.5 H_{bb} reconstruction

The last step in assessing the jet algorithms' performance before applying any event selection is to have a look at Higgs reconstruction. Fig. 6.6(a) shows the fraction of events in which the b-quarks from the Higgs decay are matched to jets, and $90 \leq \mathrm{m_{bb}} \leq 150$. The k_T-type algorithms perform better than the cone algorithms over the full range of R. This distribution is related to both matching efficiency (Fig. 6.7(a), better at smaller R) and b-jet $\mathrm{p_T}$ resolution (Fig. 6.4(a), better at larger R), which explains its shape. Fig. 6.6(b) shows the fraction of events where jets are found for the Higgs decay, but $\mathrm{m_{bb}}$ falls outside the mass window. The fairly large $(4-12\%)$ fraction of events where we lose the Higgs due to poor b-jet $\mathrm{p_T}$ resolution can be considered an important motivation for developing an excellent in-situ jet calibration for this channel.

The graphs in Fig. 6.7 show the efficiency for reconstructing the H_{bb} in mass window for the different Higgs $\mathrm{p_T}$ regions. The improvement in reconstruction efficiency with $\mathrm{p_T}$ is a consequence of the b-jets from the Higgs decay having higher $\mathrm{p_T}$, and therefore better $\mathrm{p_T}$ resolution. The increase in the difference between the performances of the k_T-type and cone algorithms in the case of a

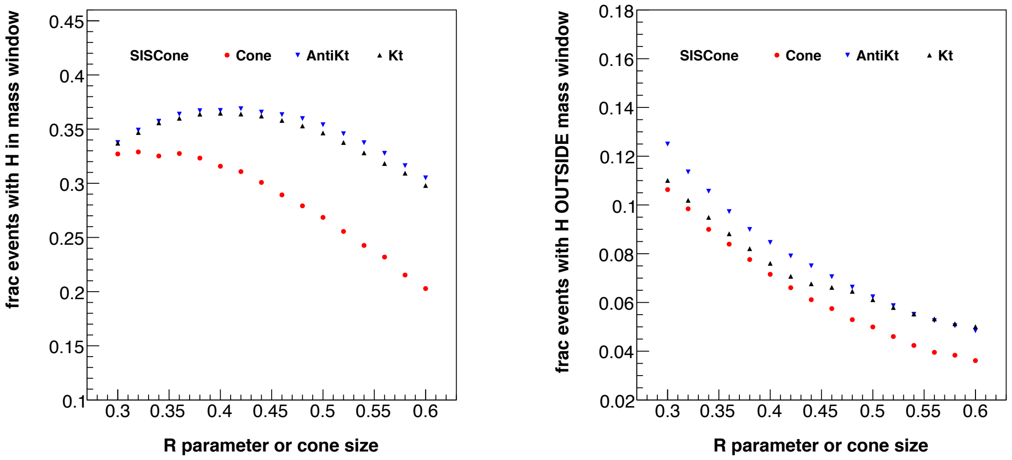

(a) Higgs reconstructed inside mass window. (b) Higgs reconstructed outside mass window.

Figure 6.6: Efficiency for reconstructing both b-jets from Higgs decay.

high p_T Higgs is due to cone algorithms' poor performance in reconstructing jets that are close together in space. A high p_T Higgs will decay to jets that are more collimated, meaning that the split-merge procedure implemented in the cone algorithms results in a failure when it comes to identifying two separate jets.

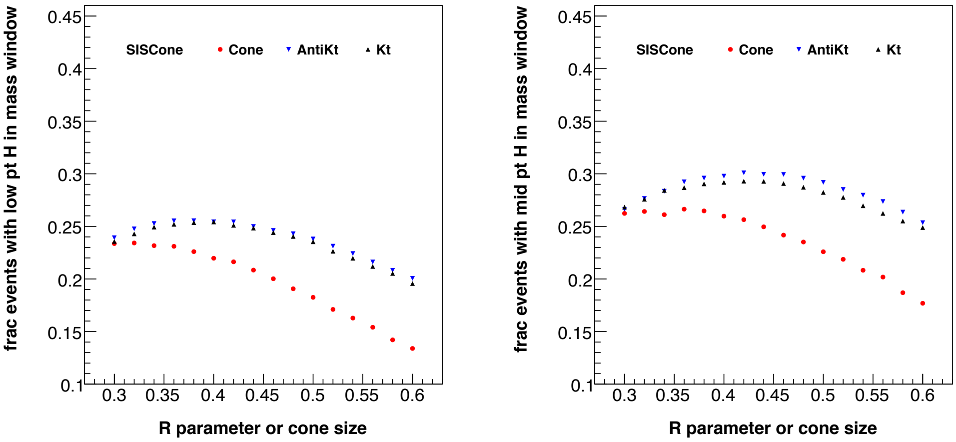

(a) Higgs $\mathrm{p_T} \leq 90$ GeV. (b) $90 \leq$ Higgs $\mathrm{p_T} \leq 180$ GeV.

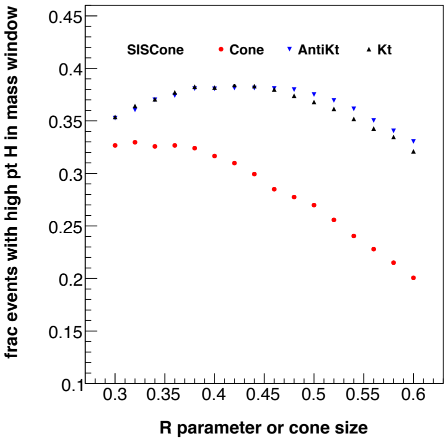

(c) Higgs $\mathrm{p_T} \geq 180$ GeV.

Figure 6.7: Efficiency for reconstructing both b-jets from Higgs decay: dependence on Higgs $\mathrm{p_T}$.

6.6 Performance in cut-based analysis

The cut-based analysis described in the $\mathrm{t\bar{t}H^0(H^0 \to b\bar{b})}$ CSC study[1] is implemented here without any changes in order that the results obtained can be compared. This analysis includes an out-of-cone jet energy correction, which is clearly not desirable for running on k_T-type jets, but is left in place for consistency.

Fig. 6.8(a) shows the fraction of events passing the jet preselection implemented in the CSC study (Sec. 5.1), with respect to the fraction passing lepton preselection. It is observed that the Cone algorithm with R= 0.4 gives a significantly lower preselection efficiency than that which is obtained with the k_T-type algorithms for R values ranging from 0.3 to 0.5.

For events passing preselection, the next job involving jets is to reconstruct the $\mathrm{W_{jj}}$. Jets are paired together and the invariant mass of the pair is calculated. If the mass of the $\mathrm{W_{jj}}$ candidate is between 55 GeV and 105 GeV then the $\mathrm{W_{jj}}$ candidate is stored. There may be several $\mathrm{W_{jj}}$ candidates stored per event. Fig. 6.8(b) shows the fraction of events where one of the stored $\mathrm{W_{jj}}$ candidates is reconstructed from the correct jets, i.e. those dr-matched to the light quarks from the W decay. As with the preselection efficiency, the efficiency for reconstructing the correct W in its mass window is greatly improved when using the k_T-type algorithms instead of the cone algorithms.

% of events	AntiKt34Truth	Cone4Truth	Relative improvement
Passing preselection	3.93%	3.24%	21.3%
$\mathrm{W_{jj}}$ in mass window	2.96%	2.24%	32.1%
Correct $\mathrm{W_{jj}}$ in mass window	1.13%	0.81%	45%
H_{bb} in mass window	1.04%	0.76%	36.8%
Correct H_{bb} in mass window	0.37%	0.23%	60.9%

Table 6.1: Efficiencies with TruthJets and for Cone4 and AntiKt34 algorithms

% of events	AntiKt34Topo	Cone4Topo	Relative improvement
Passing preselection	3.02%	2.57%	17.5%
$\mathrm{W_{jj}}$ in mass window	2.20%	1.73%	27%
Correct $\mathrm{W_{jj}}$ in mass window	0.76%	0.31%	45%
H_{bb} in mass window	0.93%	0.74%	26%
Correct H_{bb} in mass window	0.34%	0.25%	36%

Table 6.2: Efficiencies with LCTopoJets for Cone4 and AntiKt34 algorithms.

The $\mathrm{W_{jj}}$ candidates and the $W_{l\nu}$ are then combined with every possible permutation of b-jet pairs, creating a number of $\mathrm{t\bar{t}}$ candidates. The reconstructed

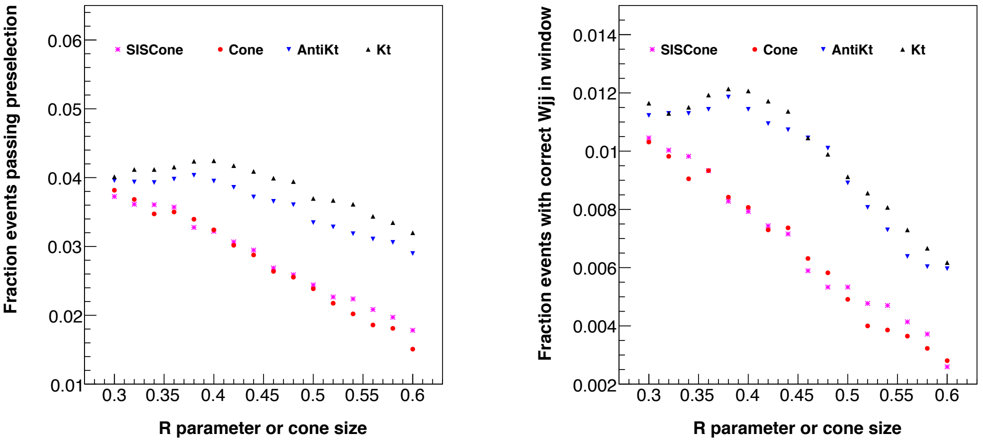

(a) Fraction of events passing jet preselection.

(b) Fraction of events where one of the $\mathrm{W_{jj}}$ candidates is correct and in window.

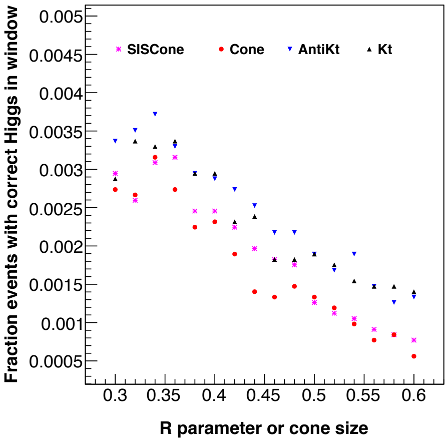

(c) Fraction of events where the reconstructed H_{bb} is correct and in mass window.

Figure 6.8: Efficiencies for various stages of the analysis.

$\mathrm{t\bar{t}}$ candidate-pair is chosen by minimising the χ^2 according to Eq. 7.1. Of the b-jets left over from reconstructing the $\mathrm{t\bar{t}}$ system, the two with the highest $\mathrm{p_T}$ are used for Higgs reconstruction. Fig. 6.8(c) shows the fraction of events in which the Higgs is made from the correct jets, and is in the mass window $90 - 150$ GeV. Clearly small R values are preferred, and use of the AntiKt algorithm with R=0.34 (as opposed to the Cone algorithm with R=0.4) results in 60% more

Higgs being reconstructed correctly and in window. The efficiencies at each stage of the event selection are summarised in Table. 6.1 and Table. 6.2.

The $\mathrm{m_{bb}}$ distribution is plotted with the Cone4 and AntiKt34 algorithms in Fig. 6.9(a) in order to show the effect on the mass peak that can be achieved by changing jet algorithm. Fig. 6.9(b) shows the same distributions obtained using jets from topological clusters rather than truth particles. The large difference in the normalisations of the Cone4 and AntiKt34 histograms is due to the much higher event selection efficiency (Table. 6.1 and Table. 6.2) when using the AntiKt34 algorithm.

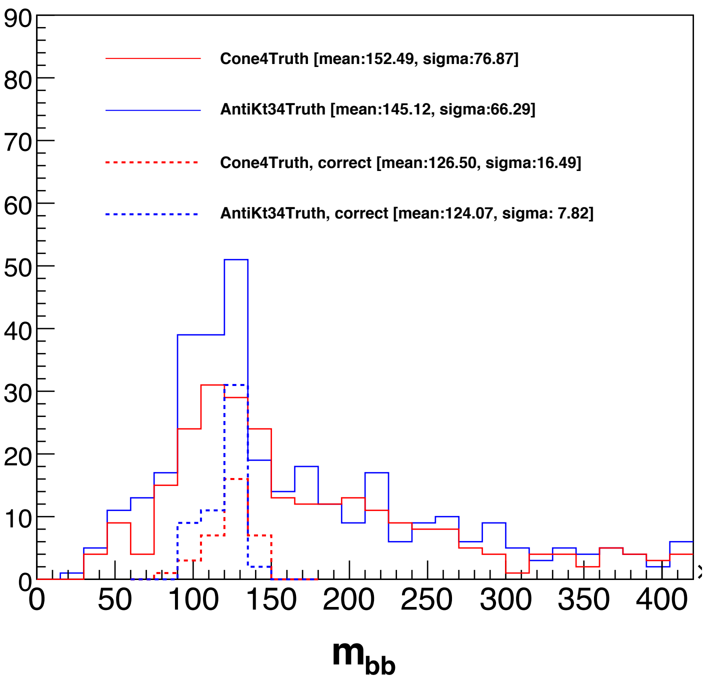

(a) Higgs mass with TruthJets.

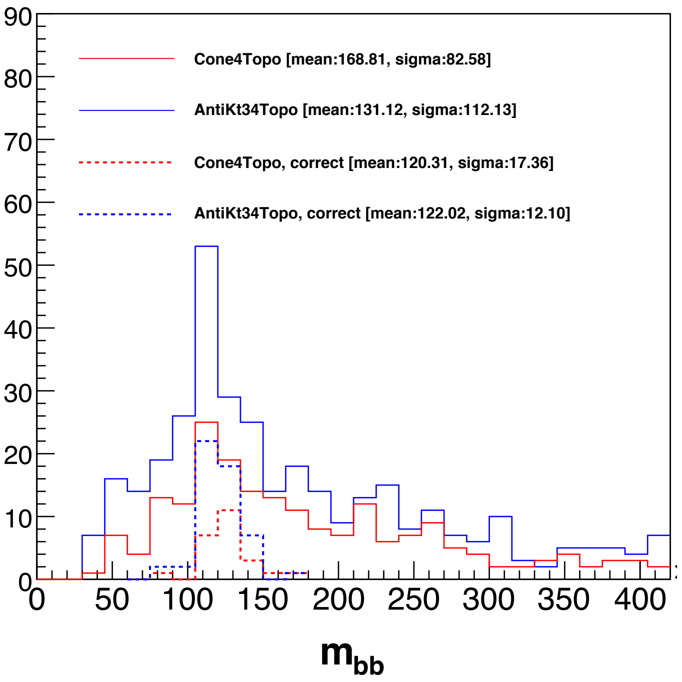

(b) Higgs mass with LCTopoJets.

Figure 6.9: Final selection: reconstructed H_{bb} mass with cone (R=0.4) and AntiKt (R=0.34) algorithms for all (solid) and correct(dashed) Higgs bosons.

Chapter 7

Final State Reconstruction: Analysis Techniques

The analysis presented here focuses on a simple cut-based analysis with the use of χ^2 and likelihood techniques to determine the best possible significance for $\mathrm{t\bar{t}H^0}$. The standard reconstruction procedure employed in the CSC study is as follows:

- The leptonically decaying W is reconstructed by combining the trigger lepton with the $\not\!\!E_\mathrm{T}$ in the event as described in Sec. 4.7.
- All possible pairs of jets are combined. If the invariant mass of a pair falls within a mass window defined as the nominal W mass (80.4 ± 25 GeV) then the pair is kept as a candidate $\mathrm{W_{jj}}$. Those jets tagged as b-jets are excluded from the $\mathrm{W_{jj}}$ reconstruction, as are jets with $\mathrm{p_T} < 20$ GeV.
- The hadronic and leptonic tops are reconstructed simultaneously by permuting and combining each ($\mathrm{W_{jj}}$, $\mathrm{W_{l\nu}}$, $\mathrm{b\bar{b}}$) triplet. The χ^2 minimisation or likelihood techniques are then used to select the best ($\mathrm{W_{jj}}$, $\mathrm{W_{l\nu}}$, $\mathrm{b\bar{b}}$) for reconstructing the $\mathrm{t\bar{t}}$ system. The $\mathrm{t\bar{t}}$ that minimises(maximises) the χ^2 (Likelihood) is selected and tested for quality. If the pair of reconstructed top quarks satisfy $\chi^2 < \chi^2_{max}(\mathcal{L} > \mathcal{L}_{min})$ then the event is passed on to Higgs reconstruction. Only those jets tagged as b-jets and having $\mathrm{p_T} > 20$ GeV are used as $\mathrm{b\bar{b}}$ candidates in the $\mathrm{t\bar{t}}$ reconstruction.

- If there are exactly two b-tagged jets left over after $\mathrm{t\bar{t}}$ reconstruction, then these are combined to make the candidate Higgs Boson. If more than two b-jets remain then the pair with the highest $\mathrm{p_T}$ are used.

7.1 Dealing with the overlap between $\mathrm{t\bar{t}b\bar{b}}$ and $\mathrm{t\bar{t}X}$ backgrounds

As described in Sec. 3.5.4, the $\mathrm{t\bar{t}X}$ background sample contains some overlap with the $\mathrm{t\bar{t}b\bar{b}}$ sample. To investigate the magnitude of this effect, the number of events with additional truth-matched jets is counted before and after preselection for the $\mathrm{t\bar{t}X}$ sample and also for the $\mathrm{t\bar{t}b\bar{b}}$ sample. This is done for the $\mathrm{t\bar{t}b\bar{b}}$ sample in order to get an idea of the amount of additional b-jets one can expect from the parton shower as implemented by Herwig in both samples. The percentage of events having more than two jets matched with $\Delta\mathrm{R} < 0.3$ to b-quarks are shown in Table. 7.1. Before preselection the percentage of events having additional b-jets is reasonably small, but when preselection cuts are applied it is evident that a large proportion of the $\mathrm{t\bar{t}X}$ background is passing preselection on the basis of these additional b-quarks.

Some of the additional b-jets in the $\mathrm{t\bar{t}X}$ sample are a result of b-jet pairs being produced in the parton showers and some of them are coming from the hard process as described in Sec. 3.5.4. It is this second category of additional b-jets that is classed as overlap, as the cross-section for processes that produce

	Before preselection		After preselection	
	xbj	≥ 20 GeV	xbj	≥ 20 GeV
tt3p	6.4%	1.4%	51.0%	41.9%
tt2p	4.7%	0.8%	45.0%	38.8%
tt1p	3.7%	0.4%	46.5%	39.5%
tt0p	3.0%	0.2%	33.3%	23.8%
$\mathrm{t\bar{t}b\bar{b}}$	6.2%	0.4%	11.0%	4.5%

Table 7.1: Overlap in $\mathrm{t\bar{t}X}$ sample before and after preselection.

additional b-jets as part of the hard scatter is already provided in the dedicated $\mathrm{t\bar{t}b\bar{b}}$ background sample. These events are removed from the $\mathrm{t\bar{t}X}$ background as described in[44]. The basic procedure is to look at the truth particles in the $\mathrm{t\bar{t}X}$ sample and remove all of the events containing an additional b-jet pair not produced in the parton shower. This procedure results in a removal of 5.6$\%$ of the $\mathrm{t\bar{t}X}$ cross-section. The analysis presented in this chapter is inclusive of this overlap removal.

7.2 Jet calibration and mass cuts

The jets used in this study are made by running the AntiKt algorithm on truth particles. These jets are not calibrated to the parton level; some of the parton energy is lost in jet reconstruction due to parton showering, which causes some fraction of the energy of the original parton to be excluded by the jet algorithm. This effect is reduced with larger R values, but use of larger R values in this channel is not optimal due to the high jet multiplicity of the final state, as discussed in Sec. 6. Jets can be calibrated for this effect by using the well known masses of the $\mathrm{W_{jj}}$ and $\mathrm{t_{bjj}}$ to scale the jet energy to parton-level. This calibration will be implemented based on real data taken with ATLAS.

The reconstruction of massive objects with uncalibrated jets, such as those used in this study will reflect the energy lost from the jets as a lower than nominal mass peak. The reconstructed $\mathrm{W_{jj}}$ mass is shown in Fig. 7.1(a) for the case where the correct jets are used for reconstruction. The adjustment in mass for uncalibrated jets must of course be carried forward to the Higgs itself. Fig. 7.1(b) shows the Higgs Boson mass reconstructed from jets matched to the b-quarks from the Higgs decay.

The correct jets are determined by asking that they are within $\Delta\mathrm{R} \leq 0.3$ of the truth particles from the $\mathrm{W_{jj}}$ decay. The mass distribution peaks at 74.56 GeV and has a width of 13.78 GeV. The shift between the mean mass of the $\mathrm{W_{jj}}$ reconstructed from the correct jets and the nominal W mass 80.4 GeV is attributed entirely to the loss of radiation outside the jet that is incurred when making jets with a small R parameter.

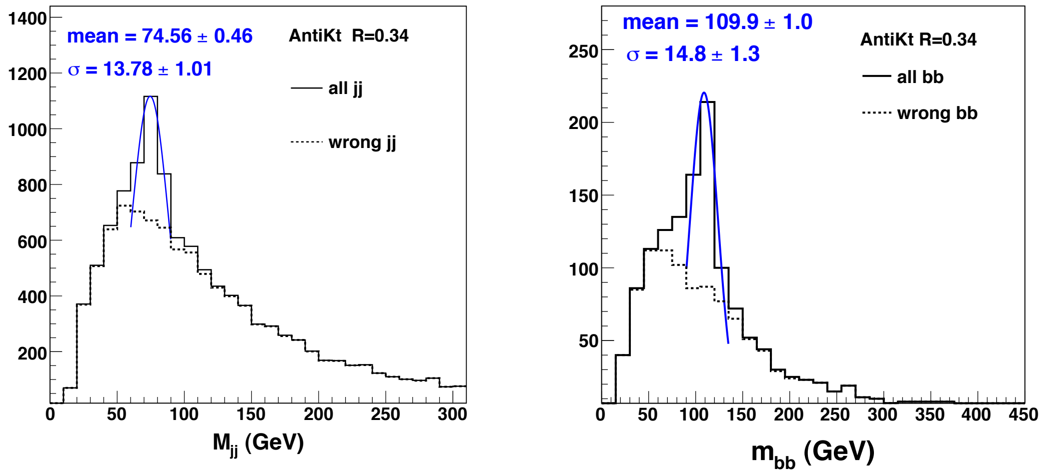

(a) Mass of the $\mathrm{W_{jj}}$ boson candidates.

(b) Mass of the $\mathrm{H_{bb}}$ boson candidates.

Figure 7.1: Mass of the $\mathrm{W_{jj}}$ and $\mathrm{H_{bb}}$ boson candidates. The dashed black histogram shows the reconstructed mass distributions for the cases where one or both of the jets are wrong. The solid black histogram shows the distribution obtained using both correct and incorrect jet pairings. The peak containing correct pairings is fitted with a Gaussian shown in blue.

In the context of this analysis the aim is to try and determine the best reconstruction procedure once all calibrations have been applied. Selecting uncalibrated jet pairs based on the nominal W mass results in the calibration effects being absorbed into the analysis, so the mean $\mathrm{W_{jj}}$ mass reconstructed from the correct pair of jets is used in place of the nominal mass in order to remove effects which will not be present with fully calibrated jets.

An appropriate $\mathrm{W_{jj}}$ mass window for uncalibrated jets is therefore taken to be 75 ± 28 GeV. Based on the Gaussian fit in Fig. 7.1(b) the Higgs mass window for uncalibrated jets is taken as 110 ± 30 GeV. The mass distributions for leptonic and hadronic top candidates are shown in Fig. 7.2 and Fig. 7.3. A Gaussian fit to the peak of the $\mathrm{t_{bjj}}$ mass distribution from the jets matched to the truth particles from the $\mathrm{t_{bjj}}$ decay has a mean value 162.9 GeV and a width of 10.13 GeV. An appropriate mass window for the $\mathrm{t_{bjj}}$ is therefore 163 ± 20 GeV. By the same reasoning the optimal $\mathrm{t_{bl\nu}}$ window for uncalibrated jets is 169 ± 38 GeV.

The mass windows defined by reconstructing the final state objects from

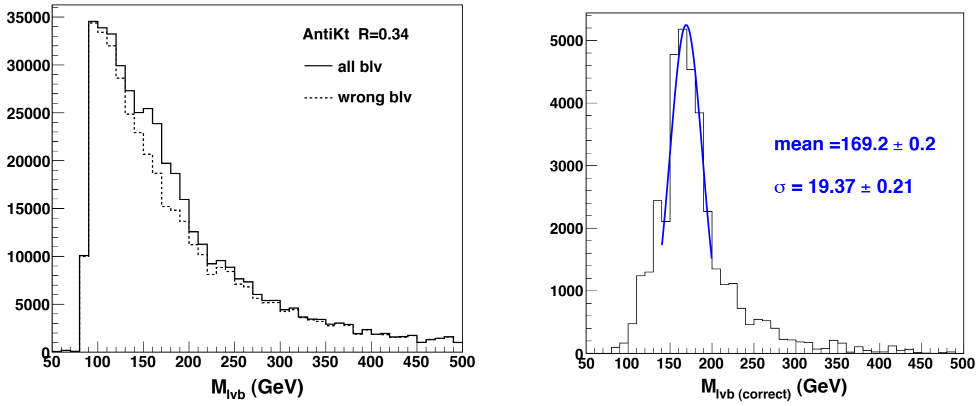

(a) All leptonic top candidates.

(b) Correct $l\nu b$ used in top reconstruction.

Figure 7.2: Invariant mass of the leptonic tops reconstructed from $bl\nu$

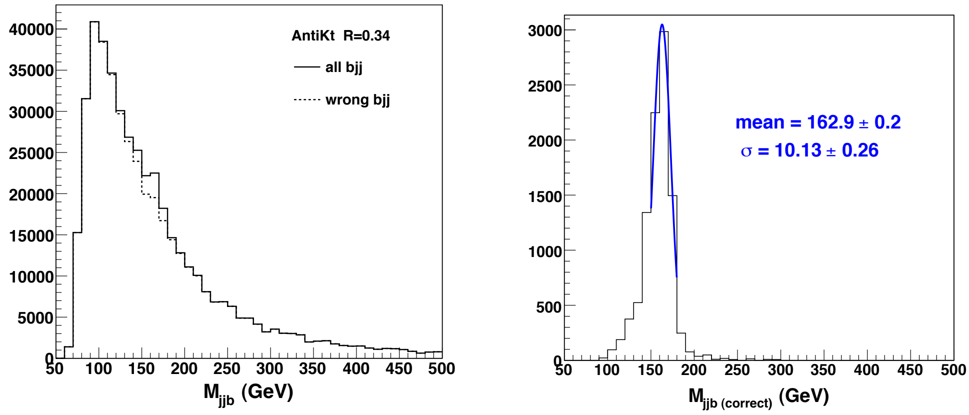

(a) All hadronic top candidates.

(b) Correct jjb used in top reconstruction.

Figure 7.3: Invariant mass of the hadronic tops reconstructed from bjj

the correct uncalibrated jets are listed in Table. 7.2 along with nominal masses. In the case of the Higgs the nominal mass is the mass at which the Higgs is generated.

	Nominal mass (GeV)	Uncalibrated Mass (GeV)
W_{jj}	80.4 ± 25	75 ± 28
t_{bjj}	175 ± 25	163 ± 20
$t_{bl\nu}$	175 ± 25	169 ± 38
H_{bb}	120 ± 30	110 ± 30

Table 7.2: Masses adjusted to reflect the uncalibrated jets used in reconstruction.

7.3 Reconstruction of Higgs Boson candidates

Before venturing into the reconstruction of the $t\bar{t}$ system it is interesting to look at a simple Higgs reconstruction procedure on those events passing preselection. The jets in these events are ordered by either b-weight or p_T and the two jets with the highest values of these criteria are combined to create Higgs candidates. Fig. 7.4 shows the mass distributions obtained by each of these selection methods, scaled to show the number of events expected in 30 fb^{-1} of data.

The mass distributions corresponding to selection of the two jets in the event with the highest p_T clearly peak away from the Higgs mass, suggesting that the highest p_T jets in a $t\bar{t}H^0$ event often come from the W_{jj} or top quark decays. It is interesting that there is very little overlap between those jets with the highest p_T and those with the highest b-weight, as historically the selection procedure for this channel has always been to choose the jets with highest p_T for Higgs reconstruction. The significance at this stage is found to be $\frac{s}{\sqrt{b}} = 1.35$ in a mass window 110 ± 30 GeV for jets selected by b-weight. For jets selected by p_T this figure is $\frac{s}{\sqrt{b}} = 0.84$.

7.3.1 Systematic uncertainty from JES

The systematic uncertainty coming from the JES is quantified by adding and subtracting 7% to the energy of all jets before the preselection cuts are made. The effects from JES at this stage of the analysis are summarised in Table. 7.3 for the signal and background for the methods of selecting jet paris by p_T and by b-weight. Selecting the hardest two jets for Higgs reconstruction results in a

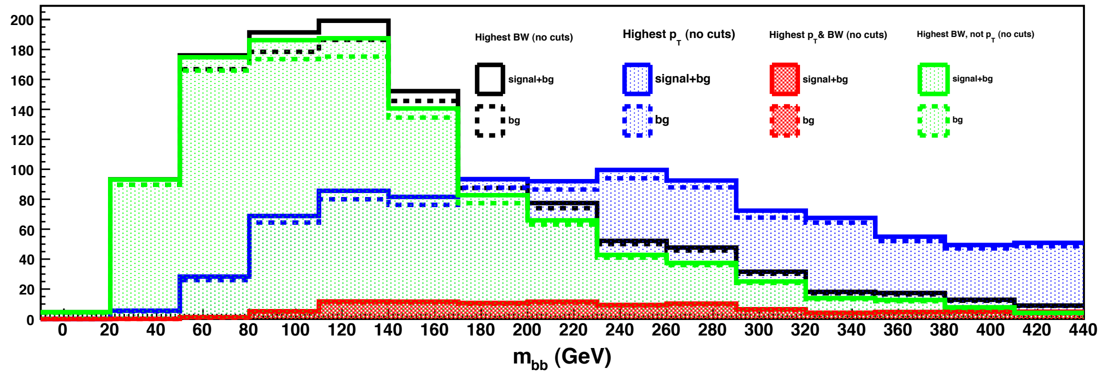

Figure 7.4: Mass of the Higgs in the case where the jets for reconstruction are selected by p_T (black) and by b-weight (blue). The dashed lhistograms contain the contribution from all backgrounds considered in this study and the solid histograms contain all background and signal events. The red histograms contain events in which the two jets with the highest p_T also have the highest b-weights. The green histograms are obtained by subtracting the red histogram from the black histogram.

significantly larger uncertainty on the number of $t\bar{t}H^0$ signal in the mass window when compared with the method of selecting the jets with the highest b-weight.

In Fig. 7.5 the m_{bb} distribution is plotted for the case where the two jets with the highest b-weights are used for Higgs reconstruction, for unadjusted jets and for jets that have had their energy adjusted by $\pm 7\%$. Although the uncertainty in the mass window region is not unmanageably large, the very low significance means that even an uncertainty of a few $\%$ makes it difficult to distinguish background from signal+background at this stage.

7.3.2 Systematic uncertainty from b-tagging

The uncertainty on the b-tagging efficiency has been found previously[1] to be the single largest contributer to the systematic uncertainty on this channel. In Fig. 7.6 the effect of increasing the b-tagging efficiency by 5% (which translates as adding 0.8 to the b-weight of every jet as discussed in Sec. 5.4.3 on the m_{bb} distributions is clearly visible. In particular the uncertainty on the $t\bar{t}X$ component of the background shown in Fig. 7.6(c) is larger than the background

Selection of highest p_T jets				
	N	$N_{+\sigma}$	$N_{-\sigma}$	$\Delta_{max}\%$
signal	10.05	8.71	9.99	13.3
background	144.35	150.72	135.81	5.9
significance	0.84	0.79	0.86	
Selection of highest b-weight jets				
	N	$N_{+\sigma}$	$N_{-\sigma}$	$\Delta_{max}\%$
signal	25.77	25.94	24.85	3.6
background	364.82	384.26	365.88	5.4
significance	1.35	1.32	1.30	

Table 7.3: Numbers of events with $80 \leq m_{bb} \leq 140$ GeV for 30 fb^{-1}. $N_{\pm\sigma}$ is the number obtained when varying the JES up and down by 7%.

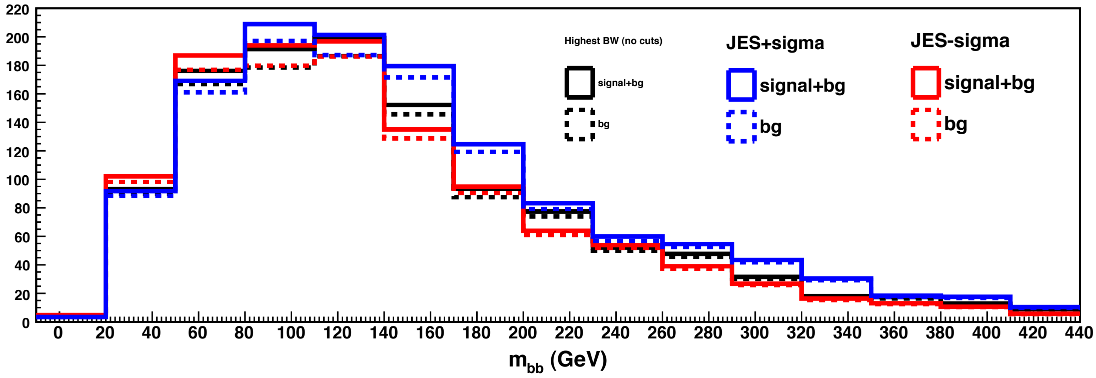

Figure 7.5: Effect of varying the JES up and down by 7%

itself. Variation of the b-weight also has an effect on the mis-tag rate (see Sec. 5.4.3) which contributes to the large change in normalistion apparent in Fig. 7.6.

Because the uncertainty is so large, it is considered interesting to see what happens to these distributions when applying the requirement that there are at least 4 jets with b-weight greater than 4.5 in each event.

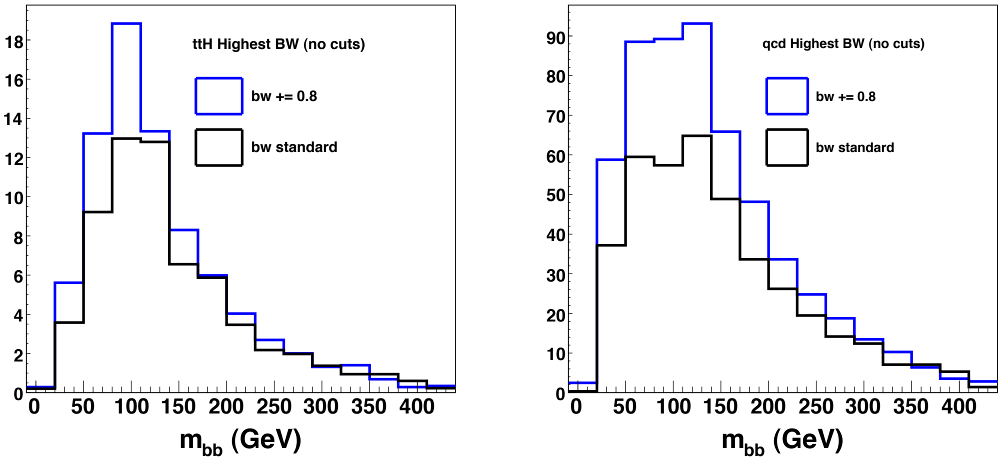

(a) $t\bar{t}H^0$ (b) $t\bar{t}b\bar{b}(qcd)$

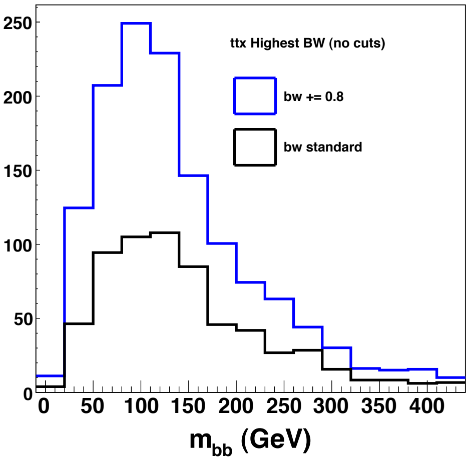

(c) $t\bar{t}X$

Figure 7.6: The effect on the shape of the m_{bb} distribution for signal and background when varying the systematic uncertainty on the b-tagging efficiency by 5%.

An additional b-weight cut of bw≥ 4.5 is applied to the jets used for Higgs reconstruction in order to determine the effect on the uncertainty from the b-tagging efficiency. The same $\mathrm{m_{bb}}$ are shown in Fig. 7.7 for this case. Unsurprisingly the $\mathrm{t\bar{t}H^0}$ and $\mathrm{t\bar{t}b\bar{b}}$ distributions are largely unchanged; the highest two b-weight jets in these samples generally have b-weight greater than the cut of 4.5. The uncertainty on the $\mathrm{t\bar{t}X}$ background is somewhat reduced, although it is still of the same order of size as the background itself.

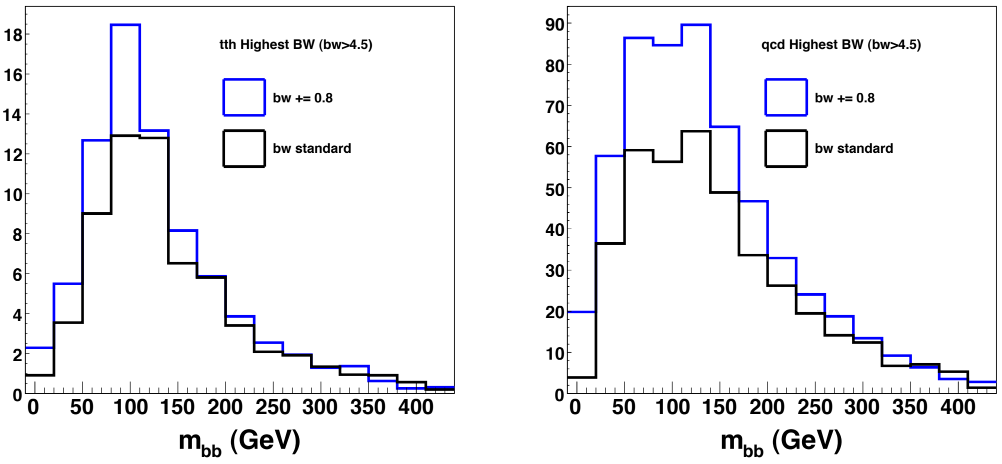

(a) $\mathrm{t\bar{t}H^0}$ (b) $\mathrm{t\bar{t}b\bar{b}(qcd)}$

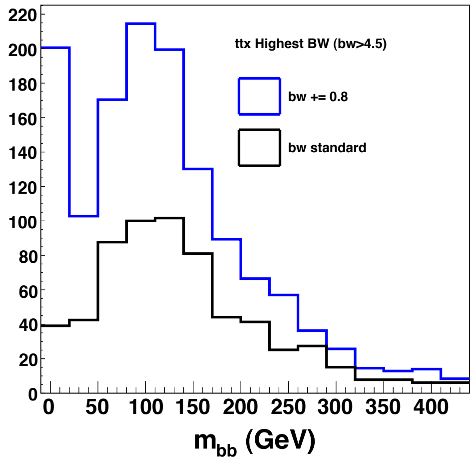

(c) $\mathrm{t\bar{t}X}$

Figure 7.7: The effect on the shape of the $\mathrm{m_{bb}}$ distribution for signal and background when varying the systematic uncertainty on the b-tagging efficiency by 5% for the case where the jets used for Higgs reconstruction have bw≥4.5.

7.4 Reconstruction of the $\mathrm{t\bar{t}H^0}$ system

The starting point for this analysis is to use a cut-based analysis as described above with cuts very similar to those implemented in[1]. All distributions are scaled to represent the number of expected events for 30 $\mathrm{fb^{-1}}$ of data.

The χ^2 minimisation method used in this first analysis is shown in Eq. 7.1.

This method minimises the difference between the nominal and reconstructed top masses divided by the resolution on the reconstructed top mass. Here, the σ_m are obtained from Fig. 7.2 and Fig. 7.3. The difference between the reconstructed and adjusted-nominal (see Table. 7.2) top mass is calculated for each candidate top, giving us a χ^2 value for every possible $\mathrm{t\bar{t}}$ combination on an event-by-event basis. The combination with the lowest value of χ^2 is then chosen as the best $\mathrm{t\bar{t}}$ candidate.

$$\chi^2 = \frac{\Delta M^2_{jjb}}{\sigma^2_{m_{jjb}}} + \frac{\Delta M^2_{l\nu b}}{\sigma^2_{m_{l\nu b}}} \tag{7.1}$$

Different selection criteria are tested to see the effect on signal and background distributions.

NOCUTS: the jets used in reconstruction of the $\mathrm{W_{jj}}$ are required to have $\mathrm{p_T}$ ≥20 GeV. There are no $\mathrm{p_T}$ cuts applied to the other jets used in final state reconstruction. Candidate $\mathrm{W_{jj}}$ are reconstructed from all jet pairs excluding the four jets with the highest b-weight. The $\mathrm{t\bar{t}}$ system is then reconstructed by combining all of the $\mathrm{W_{l\nu}}$ and $\mathrm{W_{jj}}$ candidates with pairs of jets, where any jets can be used providing they have not been used already in the reconstruction of the $\mathrm{W_{jj}}$ candidate in the current permutation. The $\mathrm{t\bar{t}}$ system that minimises Eq. 7.1 is chosen.

TOPFOUR: the same reconstruction procedure is followed as for NOCUTS but only the jets with highest four b-weights are combined with the $\mathrm{W_{l\nu}}$ and $\mathrm{W_{jj}}$ to form the $\mathrm{t\bar{t}}$ candidates. As the Higgs is reconstructed using only those jets left over from top reconstruction, it follows that the jets used for HIggs reconstruction will also be two of the top four b-weighted jets, thus will have b-weights ≥ 2.5 by default.

BW cuts: the jets used in Higgs reconstruction are required to have b-weights ≥ 2.5 or ≥4.5.

Fig. 7.8 shows the change in shape of the mass distributions from each component of the background and the signal when altering the selection criteria such that only the four jets with the highest b-weights are available for the reconstruction of the $\mathrm{t\bar{t}}$ system. There are no b-weight cuts on the jets used in Higgs reconstruction. Several differences in the shape of all the mass distributions are immediately apparent when the jets used for reconstructing the top quarks are subject to the b-weight requirement. With the method 'NOCUTS' the background distributions all peak roughly around the Higgs mass region. With the 'TOPFOUR' cut applied all of the Higgs mass distributions peak at lower mass values. There are more events in the window $80 \leq \mathrm{m_{bb}} \leq 140$ GeV for signal and for background when using the 'TOPFOUR' method. The electroweak component of the $\mathrm{t\bar{t}b\bar{b}}$ background becomes noticeably more peaked in the $80 - 110$ GeV bin, Fig. 7.8(a). This is the location of the $\mathrm{Z^0}$ mass, the nominal value of which is 90 GeV.

Fig. 7.9 shows the change in shape of the mass distributions from each component of background and the signal when requiring that the jets used for Higgs reconstruction have b-weight ≥4.5, in comparison with the 'TOP FOUR' selection cuts. The lower number of events in the histograms for all samples is due to the fairly sizable number of events in which two jets with b-weight ≥4.5 are not available following $\mathrm{t\bar{t}}$ reconstruction. This is particularly prominent effect in the $\mathrm{t\bar{t}X}$ sample, Fig. 7.9(c), which is unsurprising as the $\mathrm{t\bar{t}X}$ sample does not contain additional (non-$\mathrm{t\bar{t}}$) b-jets other than those from UE. The shapes of the $\mathrm{t\bar{t}b\bar{b}}$ and $\mathrm{t\bar{t}H^0}$ distributions do not change in the Higgs mass window region.

Fig. 7.10 shows the change in shape of the mass distributions from each component of background and the signal when requiring that the jets used for Higgs reconstruction have b-weight ≥4.5, in comparison with the NOCUTS selection cut.

The numbers of signal and background events with $80 \leq \mathrm{m_{bb}} \leq 110$ GeV using the various methods described above are shown in Table. 7.4.

There is a small increase in significance when one asks that only b-tagged jets be used as b-jets in the reconstruction of the top quarks.

The 'TOPFOUR' method results in a significance of 1.48, which is the highest significance available for this channel using these techniques. The $\mathrm{m_{bb}}$ distribution obtained using this method is shown in Fig. 7.11 with the background contributions stacked one on top of another such as to show the expected shape of all contributions to the $\mathrm{m_{bb}}$ distribution. The same distribution is shown

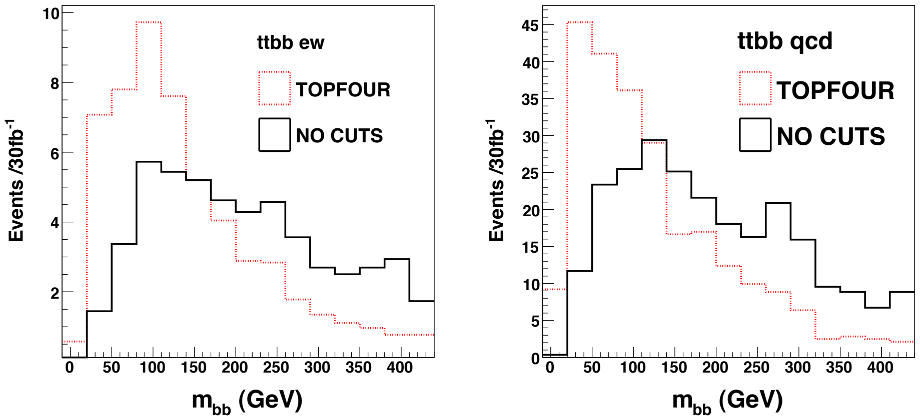

(a) $t\bar{t}b\bar{b}$(ew) (b) $t\bar{t}b\bar{b}$(qcd)

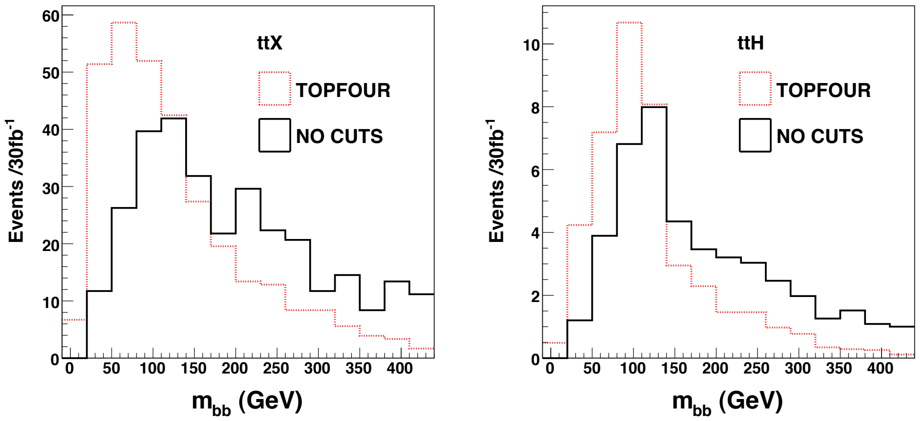

(c) $t\bar{t}X$ (d) $t\bar{t}H^0$

Figure 7.8: The change in shape of the m_{bb} distributions when selecting the $t\bar{t}$ system based on the NOCUTS and TOPFOUR methods (see text for description of methods).

using the ATLAS standard jet algorithm AntiKt with R=0.4 in Fig. 7.12. The significance obtained with the slightly larger R parameter of 0.4 in place of 0.34 results in a decrease in significance from 1.48 to 1.35.

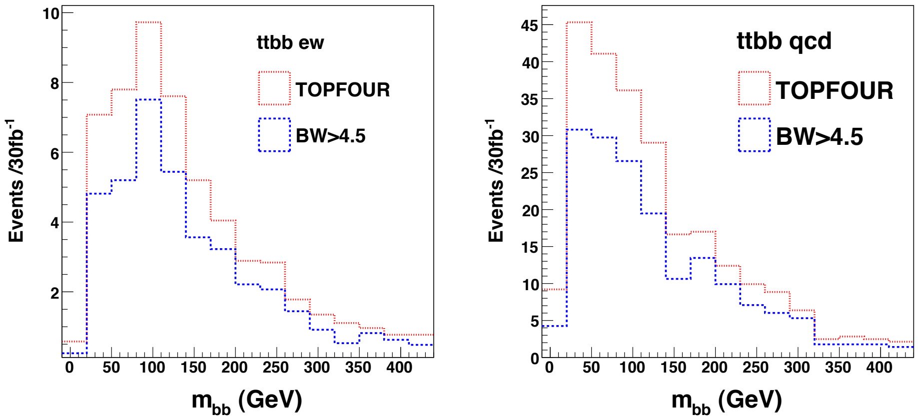

(a) $t\bar{t}b\bar{b}(ew)$ (b) $t\bar{t}b\bar{b}(qcd)$

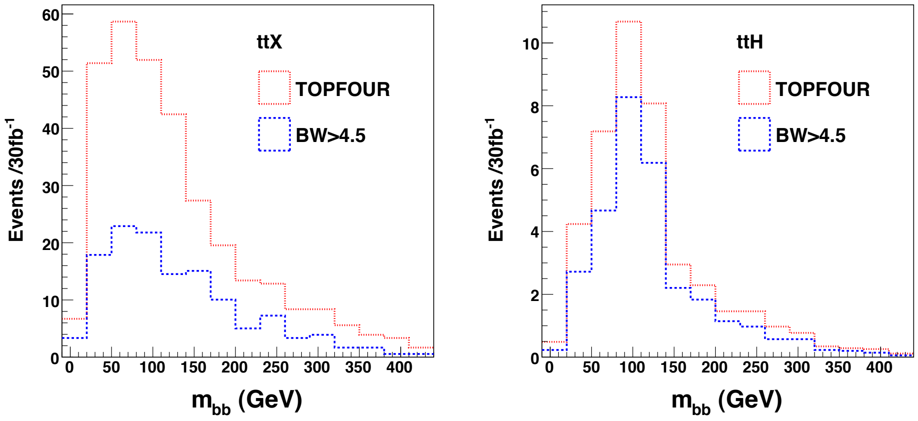

(c) $t\bar{t}X$ (d) $t\bar{t}H^0$

Figure 7.9: The change in shape of the m_{bb} distributions when the TOPFOUR method is used for $t\bar{t}$ selection and the b-weight cut on the jets used for Higgs reconstruction is increased from 2.5 to 4.5.

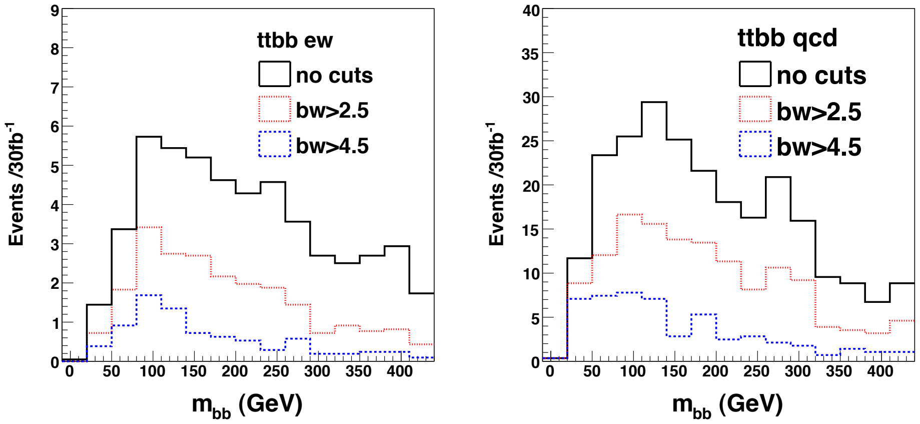

(a) $t\bar{t}b\bar{b}$(ew) (b) $t\bar{t}b\bar{b}$(qcd)

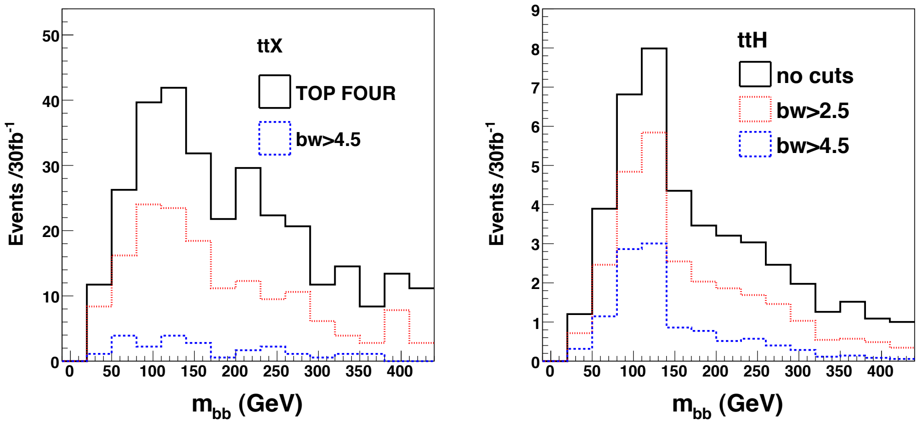

(c) $t\bar{t}X$ (d) $t\bar{t}H^0$

Figure 7.10: The change in shape of the m_{bb} distributions when the NOCUTS method is used for $t\bar{t}$ selection and the b-weight cut on the jets used for Higgs reconstruction is increased to 2.5 and to 4.5.

Method	Signal	Background	Significance
NOCUTS	14.8	147.6	1.22
bw>2.5	10.7	85.9	1.15
bw>4.5	5.9	24.1	1.20
TOPFOUR	18.8	176.9	1.41
bw>45	14.5	95.3	1.48

Table 7.4: Significances obtained with different requirements on the jets used for reconstructing the $\mathrm{t\bar{t}H^0}$ system.

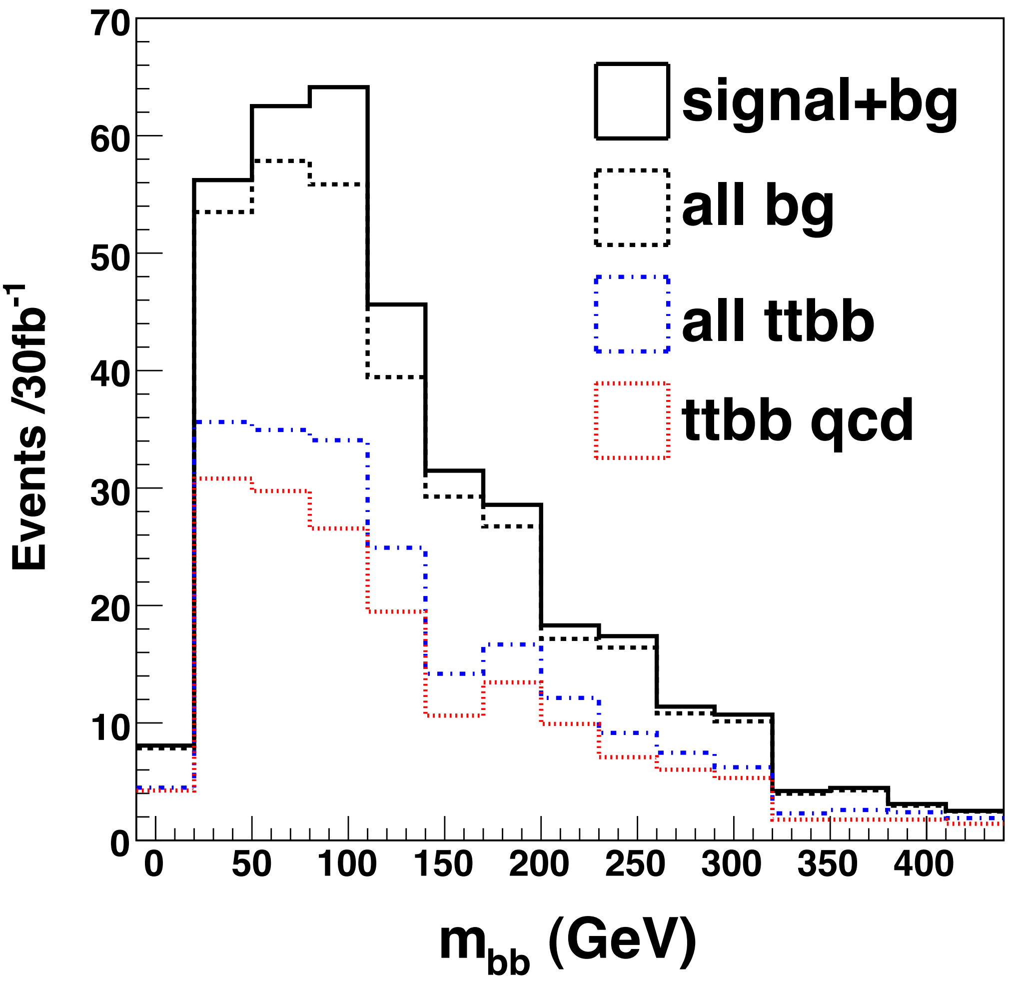

Figure 7.11: Higgs mass with AntiKt R=0.34, $\frac{s}{\sqrt{b}} = 1.48$.

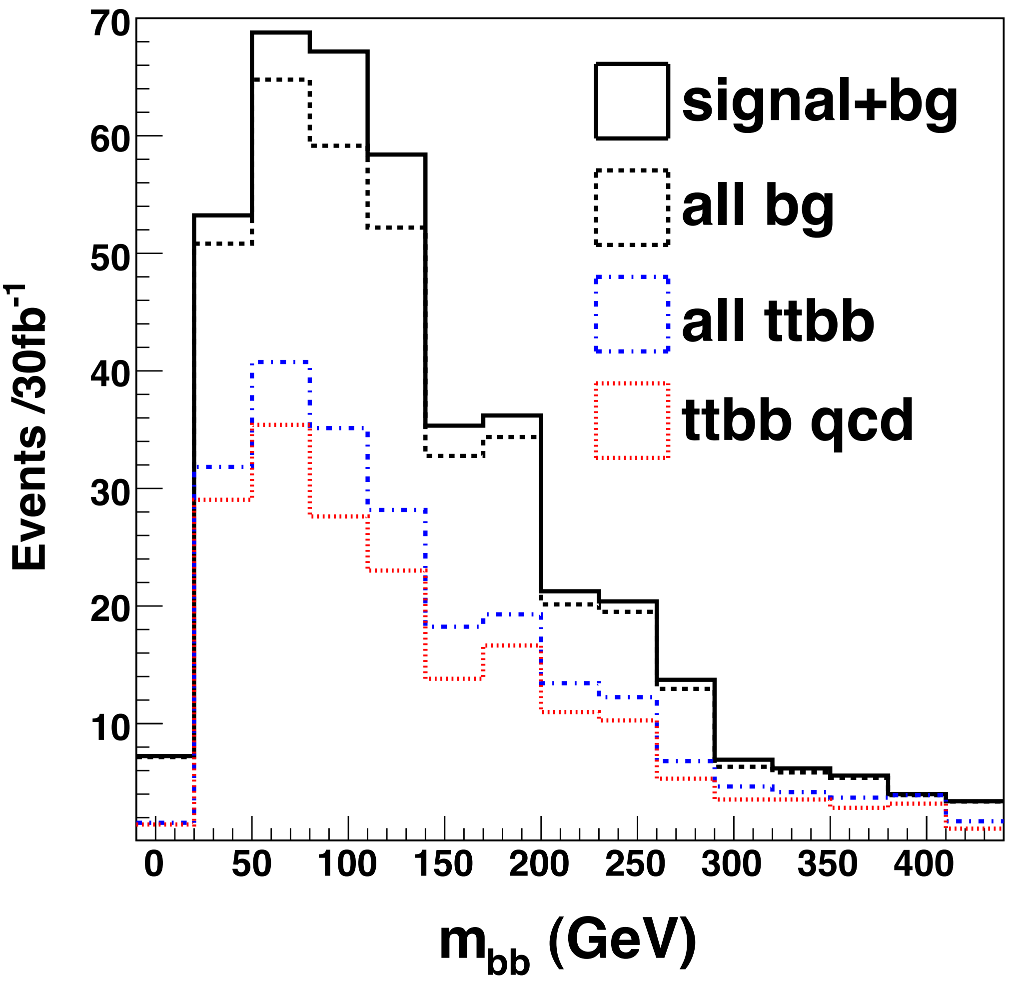

Figure 7.12: Higgs mass with AntiKt R=0.4, $\frac{s}{\sqrt{b}} = 1.35$.

7.5 The Likelihood method

The ultimate aim of this analysis is to reduce the reducible background with preselection cuts and to reduce the irreducible background in the Higgs mass region by using the correct jets for the Higgs reconstruction in the case of the signal. This is somewhat reliant on correctly reconstructing the $\mathrm{t\bar{t}}$ system in the signal sample.

This method makes use of much more information than just the masses of the composite objects. Template histograms are made containing the distributions of kinematic variables of the $\mathrm{t\bar{t}}$ system, shown in Fig. 7.13. Each variable has a pair of reference histograms corresponding to correct and incorrect object reconstruction. The histograms are normalised to unit area such that the probability of $\mathrm{t\bar{t}}$ candidate being correctly reconstructed can be expressed as a function of the value v of the variable in question according to Eq. 7.2:

$$p^{\mathrm{cor}}_{\mathrm{var}}(v) = \frac{N^{\mathrm{cor}}_{\mathrm{var}}(v)}{N^{\mathrm{cor}}_{\mathrm{var}}(v) + N^{\mathrm{incor}}_{\mathrm{var}}(v)} \tag{7.2}$$

$N^{\mathrm{cor}}_{\mathrm{var}}$ is the number of entries in the bin corresponding to the value v of variable var from the histogram containing the distribution corresponding to the correctly reconstructed $\mathrm{t\bar{t}}$ system.

In the general case where more than one variable is being considered, the product of the $\mathrm{p_{var}}(v)$ corresponding to all the considered var is then calculated according to Eq. 7.3:

$$\mathrm{P^{cor}} = \prod_{\mathrm{i=1}}^{\mathrm{Nvar}} \mathrm{p^{cor}_{var}(v_i)} \tag{7.3}$$

The likelihood $\mathcal{L}$ of an event being correctly reconstructed based on a chosen set of variables is then given by Eq. 7.4:

$$\mathcal{L} = \frac{\mathrm{P^{cor}}}{\mathrm{P^{cor}} + \mathrm{P^{incor}}} \tag{7.4}$$

The likelihood variables examined are shown in Fig. 7.13, Fig. 7.14 and Fig. 7.15.

A study is made using several different combinations of likelihood variables to select the jets and W bosons used for reconstructing the $\mathrm{t\bar{t}}$ system. All possible $\mathrm{t\bar{t}}$ systems are reconstructed and the one with the highest likelihood according to Eq. 7.4. The significances obtained for reconstructing a Higgs boson within the mass window are given in Table. 7.5.

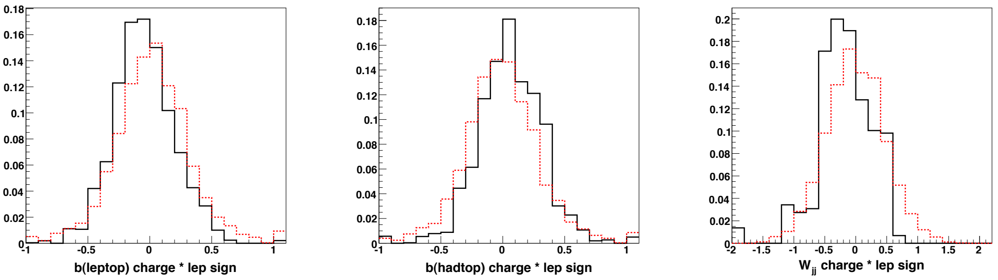

(a) Charge of b for $\mathrm{t_{bl\nu}}$ multiplied by lepton charge.

(b) Charge of b for $\mathrm{t_{bjj}}$ multiplied by lepton charge.

(c) Charge of $\mathrm{W_{jj}}$ multiplied by lepton charge.

Figure 7.13: Charge-related likelihood variables.

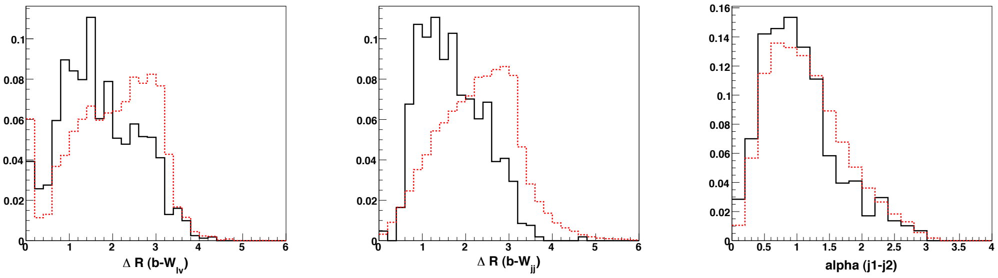

(a) Δ R between $\mathrm{W_{l\nu}}$ and b from $\mathrm{t_{bl\nu}}$.

(b) Δ R between $\mathrm{W_{jj}}$ and b from $\mathrm{t_{bjj}}$.

(c) α between jets used for $\mathrm{W_{jj}}$.

Figure 7.14: Angle-related likelihood variables.

It is clear that the correct reconstruction of a $\mathrm{t\bar{t}}$ pair does not in itself particularly help us with this channel, as all the backgrounds considered have a $\mathrm{t\bar{t}}$ in their final state. This can be seen if one compares the best significance obtained when reconstructing the $\mathrm{t\bar{t}}$ system using a likelihood method based on χ^2 and charge distributions (1.5) with the significance obtained when simply applying

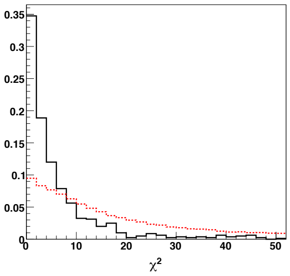

(a) χ^2 calculated according to Eq. 7.1.

Figure 7.15: χ^2 likelihood variable.

	variables	figure	$\frac{s}{\sqrt{b}}$
L9	χ^2 , angles, charge	Fig. 7.16(a)	1.35
L3	χ^2 , angles	Fig. 7.16(b)	1.35
L6	χ^2 and charge	Fig. 7.16(c)	1.5
L2	angles	Fig. 7.16(d)	1.35
L10	charge	Fig. 7.16(e)	1.22
L11	charge, angles	Fig. 7.16(f)	1.37

Table 7.5: Combinations of likelihood variables and the significances obtained with them.

preselection cuts and then choosing the two jets with the highest b-weight for Higgs reconstruction (1.48).

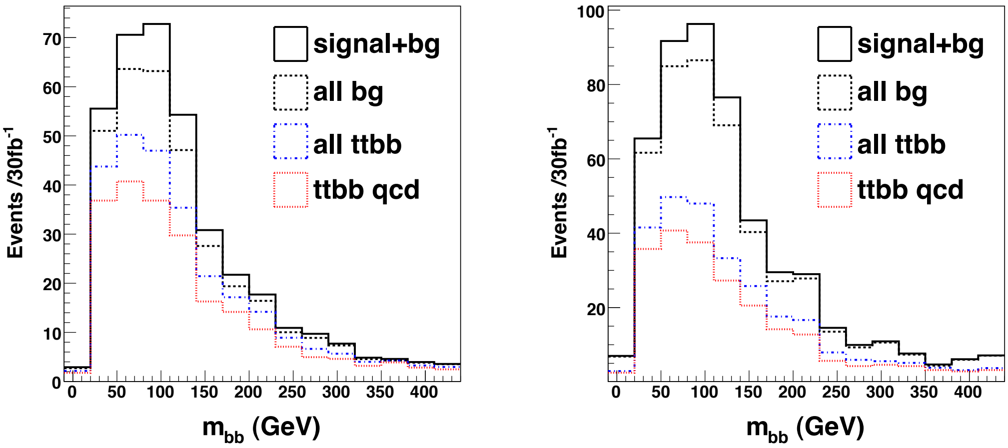

(a) L9: χ^2 , angles and charge (1.35) (b) L3: χ^2 and angles (1.35)

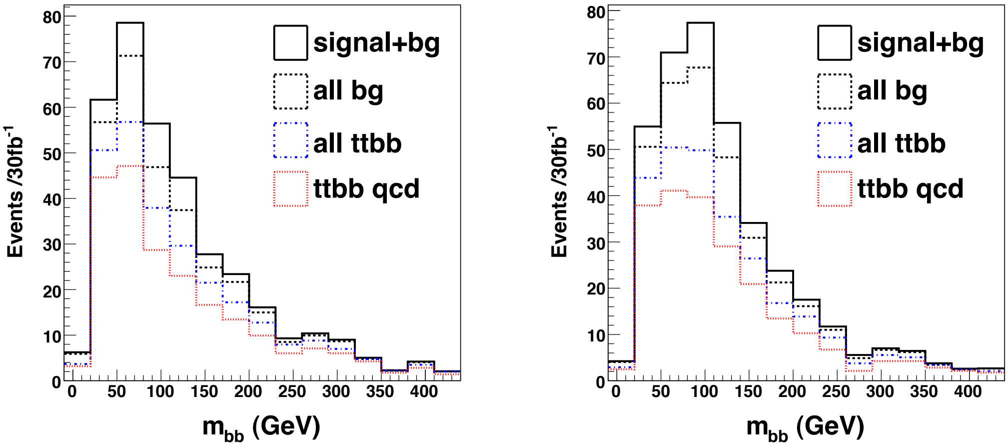

(c) L6: χ^2 and charge (1.5) (d) L2: angles only (1.35)

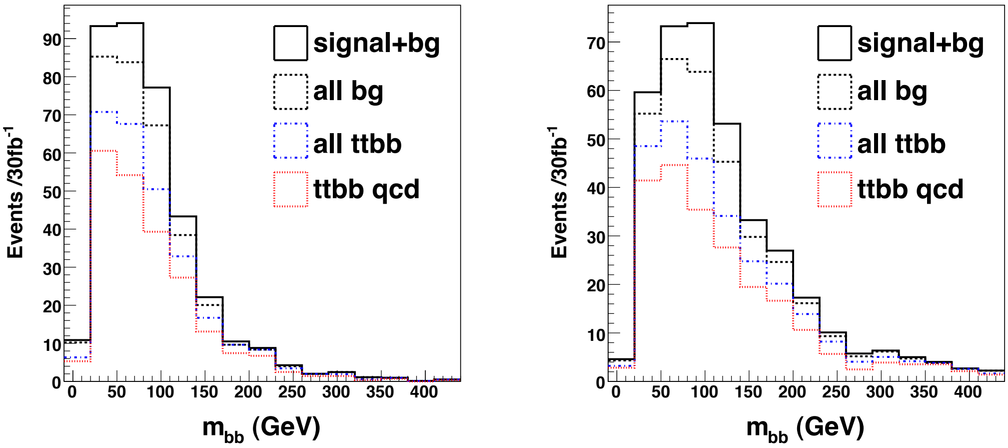

(e) L10: charge only (1.22) (f) L11: charge and angles (1.37)

Figure 7.16: Mass of the W_{jj} and H_{bb} boson candidates with different combinations of likelihood variables. The significances $\frac{s}{\sqrt{b}}$ are shown in brackets.

7.6 Systematic and Statistical Uncertainties

It has been shown previously[1] that the largest contributions to the systematic uncertainty on this channel are from the JES and the b-tagging efficiency. There are a number of other systematic uncertainties relevant to this channel that are not studied here, but were considered in the CSC study and are summarised in Table. 7.6.

In order to explore the effect of the JES and b-tagging systematics on the significance for this channel, the full analysis is repeated inclusive of the variations required to reproduce them. To reproduce the JES systematics all jets have their $\mathrm{p_T}$ varied up and down by $1\sigma(=7\%)$. The number of events with a $\mathrm{b\bar{b}}$ pair reconstructed in the mass window 80 GeV $\leq \mathrm{m_{bb}} \leq$ 140 GeV is counted for each case. Table. 7.7 shows the number of events in mass window for the case where there is no JES variation along with the maximum percentage fluctuation obtained when the JES is varied by 7%. Likewise the fluctuations in numbers of events in the mass window obtained when varying the b-weight of jets up and down by 5% are shown.

It is clear that the systematic uncertainties for this channel are very large, particularly on the background. It is, however, reasonable to expect that by the time the ATLAS experiment has collected 30 $\mathrm{fb^{-1}}$ of data the systematic uncertainties on b-tagging efficiency and JES will have improved considerably on the values of 7$\%$ (JES) and 5$\%$ (b-tagging efficiency) that are used in these calculations.

The systematics uncertainty on the JES in Table. 7.6 are significantly different from those obtained in this study for the method ‘TOPFOUR’, which most closely resembles the CSC analysis. There are a number of reasons for this, the most pertinent being that in this study the jet $\mathrm{p_T}$ cuts made at the preselection stage were in a region of very high jet mutliplicity as discussed in Sec. 5.3.1.

The uncertainty on the background from the JES is at its largest (34$\%$) when the ‘TOPFOUR’ method is used for $\mathrm{t\bar{t}}$ reconstruction. The L11 likelihood method does not use a χ^2 minimisation and the removal of the reliance on the top mass results in a reduced uncertainty from the JES, although this is still large at 19$\%$ on the combined background.

Source		$\Delta\epsilon(\%)$	
		Signal	Background
Electron	energy scale	$\pm0.5\%$	$\pm2\%$
	resolution	$\pm0.5\%$	$\pm0.6\%$
	efficiency	$\pm0.2\%$	$\pm2\%$
Muon	energy scale	$\pm0.7\%$	$\pm3\%$
	resolution	$\pm0.8\%$	$\pm0.6\%$
	efficiency	$\pm0.3\%$	$\pm0.1\%$
Jet	energy scale	$\pm9\%$	$\pm5\%$
	resolution	$\pm0.3\%$	$\pm7\%$
	b-tag	$\pm16\%$	$\pm20\%$
	miss-tag	$\pm0.8\%$	$\pm5\%$

Table 7.6: Systematic uncertainties from cut-based analysis in CSC study.[1]

It is clear from Table. 7.7 that the systematic uncertainties from both the JES and the b-tagging efficiency are highly dependent on the technique used in final state reconstruction.

The systematic uncertainty from the b-tagging efficiency is found to be lower in this study than in the CSC study for all of the methods summarised in Table. 7.7.

In any case, the significance for this channel with 30 fb^{-1} of data obtained at 10 TeV is very low, with a maximum of just 1.5 before any systematic uncertainty is taken into account.

TOPFOUR method			
	N	Δ_{JES}	Δ_{BW}
signal	14.46	1%	2%
background	95.30	34%	16%
Likelihood method L6			
	N	Δ_{JES}	Δ_{BW}
signal	16.7	17 %	7.8%
background	124.5	23 %	8.8%
Likelihood method L11			
	N	Δ_{JES}	Δ_{BW}
signal	17.4	4.8 %	4.9%
background	160.3	19.1 %	15.9%

Table 7.7: Numbers of events with $80 \leq \mathrm{m_{bb}} \leq 140$ GeV for 30 fb^{-1}. Δ_{JES} is the maximum percentage uncertainty on N when varying the JES up and down by 7%. Δ_{BW} is the maximum percentage uncertainty on N when varying the b-tagging efficiency up and down by 5%.

Chapter 8

Conclusions

The $\mathrm{t\bar{t}H^0}(\mathrm{H^0} \rightarrow \mathrm{b\bar{b}})$ channel has long been known to be extremely difficult in terms of extracting enough sensitivity to be considered a valid search channel, and this thesis confirms this difficulty whilst also emphasising the many interesting aspects of studying such a complex final state. It is considered the most promising candidate for measuring the top Yukawa coupling and this reason alone is enough to make it an essential area for study.

The expectation for ATLAS is that large amounts of data will be taken with a center of mass energy of 14 TeV rather than 10 TeV. A higher center of mass energy will have two consequences for this channel, both of which are positive in terms of significance.

1. The cross section for $\mathrm{t\bar{t}H^0}$ will increase by a factor $\sim$ 2.4
2. The majority of the background processes will have their cross sections increased by a smaller factor than 2.4. This is because the background processes to this channel have on average a lower final state mass than $\mathrm{t\bar{t}H^0}$. This can be understood in terms of the ratio of parton luminosities in Fig. 3.7 and [23].

In addition to the increased cross sections with 14 TeV, there will also be an increase in the amount of UE. The effect on the JES from UE has been studied elsewhere [45]. The general effect of UE is to increase the energy of jets, with the size of the increase being dependent on the size of the R parameter of the jet algorithm. A small R-parameter such as that used in this study will result in a reduced effect from UE compared with analyses using a larger R parameter. The opposite is true for hadronisation effects; a smaller R-parameter will result in the radiation (energy) lost outside the jets being more sizeable than one would expect with a larger R.

One of the possible areas for improvement on significance identified in the study preseneted here is the correction of b-jets containing semi-leptonic decays to muons and neutrinos (Sec. 5.2). These corrections clearly have room for improvement and it is likely that an improvement in the reconstruction of these jets would have a significant positive impact on the prospects for $\mathrm{t\bar{t}H^0}$.

Another important finding is that the selection of jets with highest b-weight results in a better significance than the selection by $\mathrm{p_T}$, as shown in Sec. 7.3. This is interesting, not least because previous studies for this channel have concentrated on the use of jets with the highest $\mathrm{p_T}$ for Higgs reconstruction.

A detailed study of the effect of the choice of jet definition on the reconstruction of the final state has emphasised the importance of the jet definition in this channel and shown that the AntiKt algorithm with a very small distance parameter of R=0.34 is the optimal jet definition for this very busy final state.

Recent studies have shown that there is promise for $\mathrm{t\bar{t}H^0}$ in a 'fat jet' analysis[46]. This analysis exploits the large number of $\mathrm{t\bar{t}H^0}$ events in which the Higgs is highly boosted, leaving a signature single fat jet in place of the $\mathrm{b\bar{b}}$ pair. A preliminary study has shown that events passing the 'fat jet' preselection cuts and events passing the preselection cuts presented in this thesis are largely orthogonal, with a maximum overlap of 46% between the samples, meaning that the two techniques will be complementary.

Perhaps the most important conclusion from this thesis work is that reconstruction of the $\mathrm{t\bar{t}}$ system is not particularly helpful in increasing the sensitivity of this channel, in fact an equivalent significance is obtained when simply applying preselection cuts discussed in Chapters 4 and 5 and then choosing the pair of jets with the highest b-weight for Higgs reconstruction. This procedure results in much lower systematic uncertainty from the JES than when one requires $\mathrm{t\bar{t}}$ reconstruction. Future work on this channel may benefit from a focus on methods of reducing the number of background events in the Higgs mass window by focusing on expected properties of the Higgs such as spin, rather than attempting to reconstruct the $t\bar{t}$ system via complex analysis techniques.

Appendix A

Precision measurements in the electroweak sector

The current estimation for the value of the Higgs mass is $\mathrm{m_H} = 116.3^{+15.6}_{-1.3}$ GeV. This estimate is based on the constraints from direct searches along with precision electroweak measurements. The determination of the Higgs mass estimate along with other predictions made based on these measurements is described in detail elsewhere[47],[6].

The top quark mass as a function of the Higgs boson mass is shown in Fig. A.1 and in Fig. A.2 as a function of the W boson mass.

The 'pull', shown in Fig. A.3, summarises the contributions from all the electroweak measurements.

The current values of the precision measurements on electroweak observables used in the calculation of the most likely value of the Higgs boson mass are summarised in Fig. A.4[6].

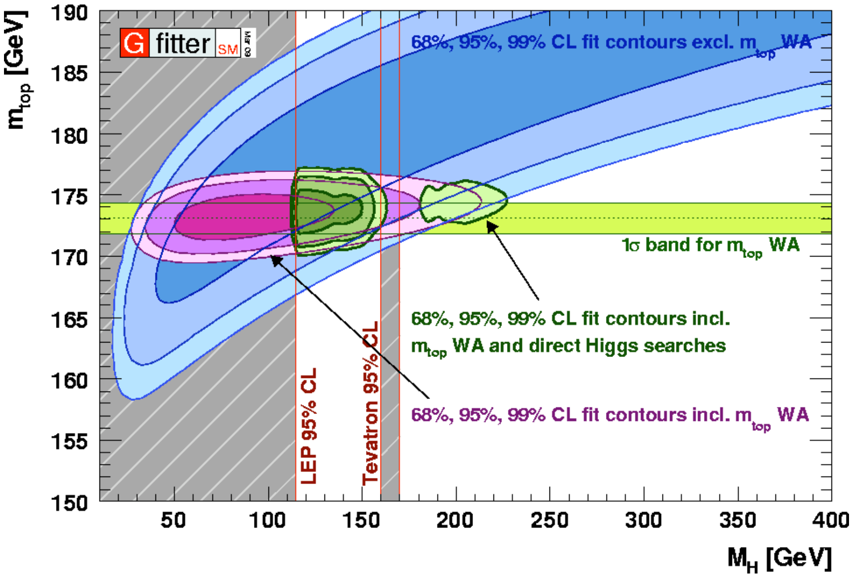

Figure A.1: Top quark mass versus Higgs mass.

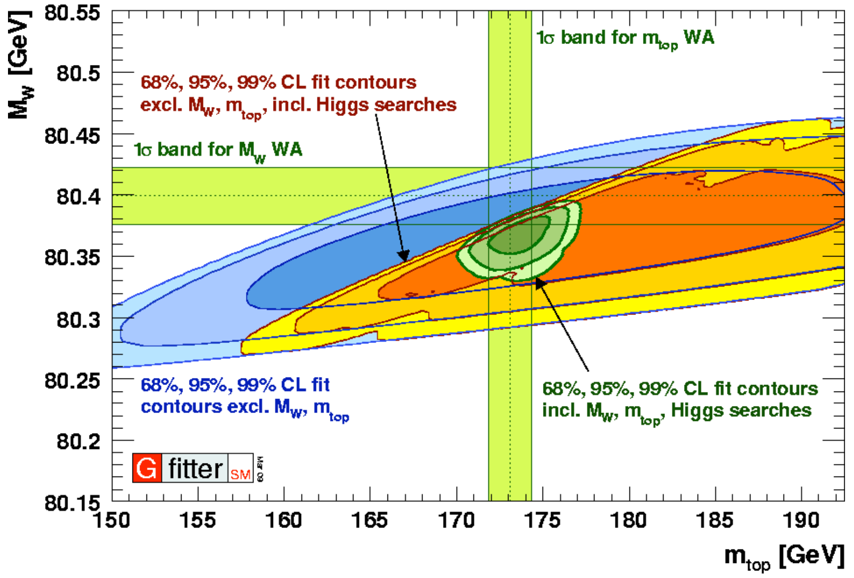

Figure A.2: W mass versus top quark mass

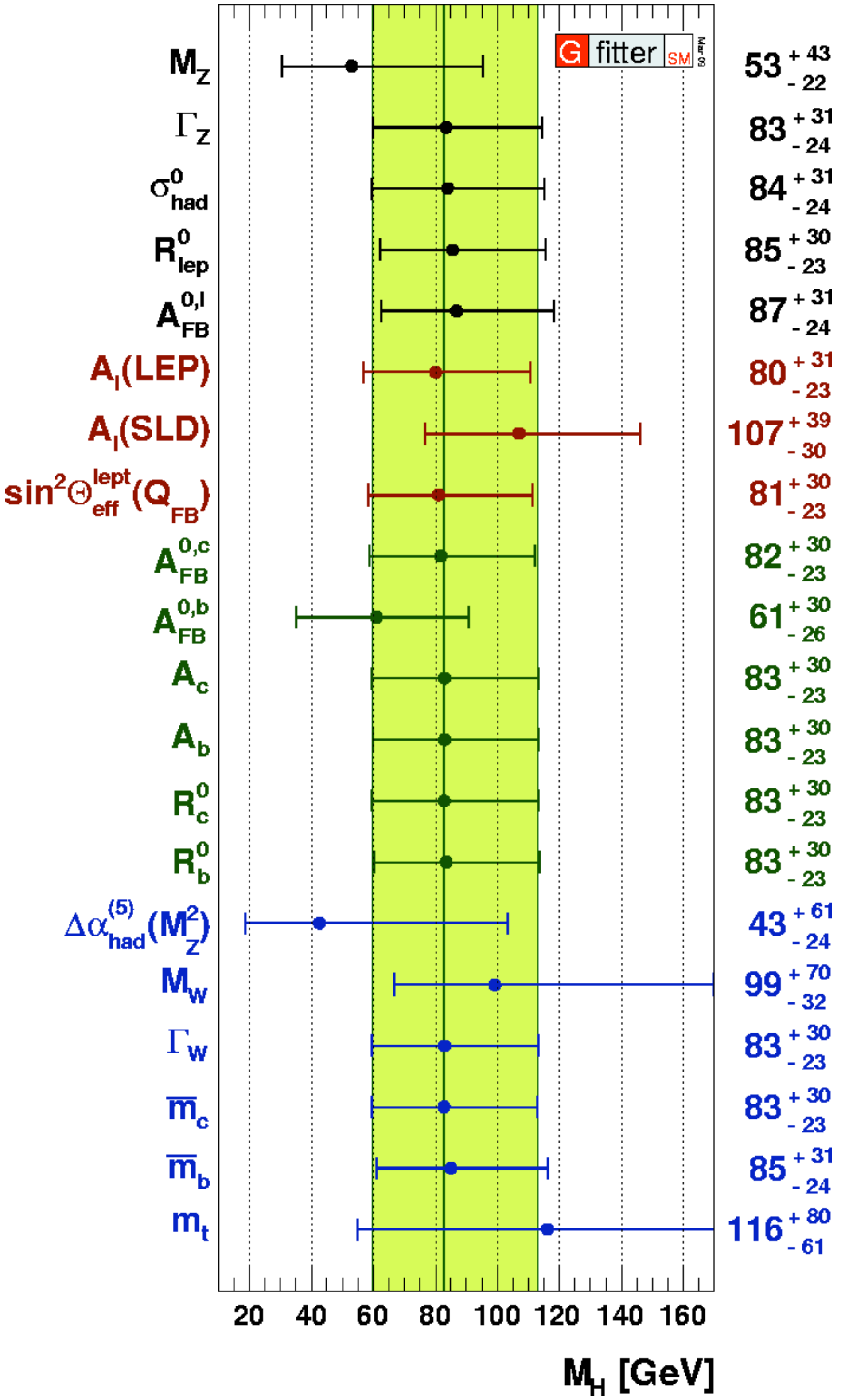

Figure A.3: Pull

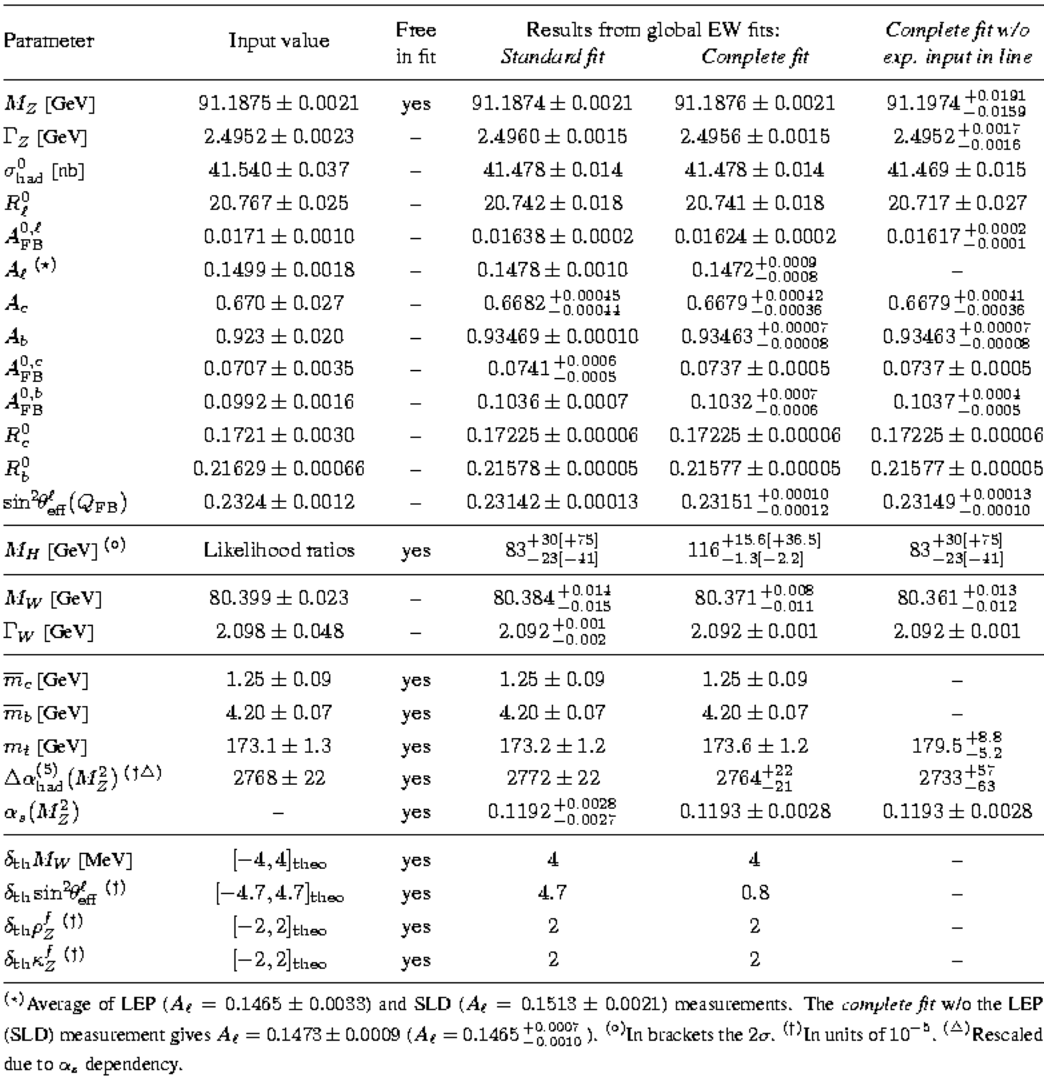

Parameter	Input value	Free in fit	Results from global EW fits:		*Complete fit w/o exp. input in line*
			Standard fit	*Complete fit*	
M_Z [GeV]	91.1875 ± 0.0021	yes	91.1874 ± 0.0021	91.1876 ± 0.0021	$91.1974^{+0.0191}_{-0.0159}$
Γ_Z [GeV]	2.4952 ± 0.0023	–	2.4960 ± 0.0015	2.4956 ± 0.0015	$2.4952^{+0.0017}_{-0.0016}$
$\sigma^0_{\rm had}$ [nb]	41.540 ± 0.037	–	41.478 ± 0.014	41.478 ± 0.014	41.469 ± 0.015
R^0_ℓ	20.767 ± 0.025	–	20.742 ± 0.018	20.741 ± 0.018	20.717 ± 0.027
$A^{0,\ell}_{\rm FB}$	0.0171 ± 0.0010	–	0.01638 ± 0.0002	0.01624 ± 0.0002	$0.01617^{+0.0002}_{-0.0001}$
A_ℓ $^{(\star)}$	0.1499 ± 0.0018	–	0.1478 ± 0.0010	$0.1472^{+0.0009}_{-0.0008}$	–
A_c	0.670 ± 0.027	–	$0.6682^{+0.00045}_{-0.00044}$	$0.6679^{+0.00042}_{-0.00036}$	$0.6679^{+0.00041}_{-0.00036}$
A_b	0.923 ± 0.020	–	0.93469 ± 0.00010	$0.93463^{+0.00007}_{-0.00008}$	$0.93463^{+0.00007}_{-0.00008}$
$A^{0,c}_{\rm FB}$	0.0707 ± 0.0035	–	$0.0741^{+0.0006}_{-0.0005}$	0.0737 ± 0.0005	0.0737 ± 0.0005
$A^{0,b}_{\rm FB}$	0.0992 ± 0.0016	–	0.1036 ± 0.0007	$0.1032^{+0.0007}_{-0.0006}$	$0.1037^{+0.0004}_{-0.0005}$
R^0_c	0.1721 ± 0.0030	–	0.17225 ± 0.00006	0.17225 ± 0.00006	0.17225 ± 0.00006
R^0_b	0.21629 ± 0.00066	–	0.21578 ± 0.00005	0.21577 ± 0.00005	0.21577 ± 0.00005
$\sin^2\theta^\ell_{\rm eff}(Q_{\rm FB})$	0.2324 ± 0.0012	–	0.23142 ± 0.00013	$0.23151^{+0.00010}_{-0.00012}$	$0.23149^{+0.00013}_{-0.00010}$
M_H [GeV] $^{(\circ)}$	Likelihood ratios	yes	$83^{+30[+75]}_{-23[-41]}$	$116^{+15.6[+36.5]}_{-1.3[-2.2]}$	$83^{+30[+75]}_{-23[-41]}$
M_W [GeV]	80.399 ± 0.023	–	$80.384^{+0.014}_{-0.015}$	$80.371^{+0.008}_{-0.011}$	$80.361^{+0.013}_{-0.012}$
Γ_W [GeV]	2.098 ± 0.048	–	$2.092^{+0.001}_{-0.002}$	2.092 ± 0.001	2.092 ± 0.001
$\overline{m}_c$ [GeV]	1.25 ± 0.09	yes	1.25 ± 0.09	1.25 ± 0.09	–
$\overline{m}_b$ [GeV]	4.20 ± 0.07	yes	4.20 ± 0.07	4.20 ± 0.07	–
m_t [GeV]	173.1 ± 1.3	yes	173.2 ± 1.2	173.6 ± 1.2	$179.5^{+8.8}_{-5.2}$
$\Delta\alpha^{(5)}_{\rm had}(M_Z^2)$ $^{(\dagger\triangle)}$	2768 ± 22	yes	2772 ± 22	2764^{+22}_{-21}	2733^{+57}_{-63}
$\alpha_s(M_Z^2)$	–	yes	$0.1192^{+0.0028}_{-0.0027}$	0.1193 ± 0.0028	0.1193 ± 0.0028
$\delta_{\rm th} M_W$ [MeV]	$[-4, 4]_{\rm theo}$	yes	4	4	–
$\delta_{\rm th} \sin^2\theta^\ell_{\rm eff}$ $^{(\dagger)}$	$[-4.7, 4.7]_{\rm theo}$	yes	4.7	0.8	–
$\delta_{\rm th} \rho^f_Z$ $^{(\dagger)}$	$[-2, 2]_{\rm theo}$	yes	2	2	–
$\delta_{\rm th} \kappa^f_Z$ $^{(\dagger)}$	$[-2, 2]_{\rm theo}$	yes	2	2	–

$^{(\star)}$Average of LEP ($A_\ell = 0.1465 \pm 0.0033$) and SLD ($A_\ell = 0.1513 \pm 0.0021$) measurements. The *complete fit* w/o the LEP (SLD) measurement gives $A_\ell = 0.1473 \pm 0.0009$ ($A_\ell = 0.1465^{+0.0007}_{-0.0010}$). $^{(\circ)}$In brackets the 2σ. $^{(\dagger)}$In units of 10^{-5}. $^{(\triangle)}$Rescaled due to α_s dependency.

Figure A.4: Precision measurements of electroweak observables.

References

[1] The ATLAS collaboration. Expected performance of atlas. *arXiv:hep-ph/0901.0512*, January 2009. xii, 8, 22, 23, 33, 44, 46, 51, 61, 62, 63, 64, 72, 73, 74, 75, 78, 94, 100, 111, 115, 128, 129

[2] The ATLAS collaboration. Atlas detector and physics performance, vol. ii. *CERN-LHCC-99-15*, May 1999. xiii, 93

[3] P.Sphicas D.Froidevaux. General-purpose detectors for the large hadron collider. *Annu. Rev. Nucl. Part. Sci. 2006.56:375-440*, August 2006. 3, 8

[4] T.Pauly M.Shapiro S.Ask, D.Malon. Report from the luminosity task force. *ATL-GEN-PUB-2006-002*, July 2006. 4

[5] LEP electroweak working group. 20

[6] J. Haller A. Hoecker K. Moenig J. Stelzer H. Flaecher, M. Goebel. Revisiting the global electroweak fit of the standard model and beyond with gfitter. *arXiv:0811.0009v3 [hep-ph]*, Feb 2009. 20, 21, 134

[7] E.Laenen K.Tollefson M.A.Dobbs, S.Frixione. Les houches guidebook to monte carlo generators for hadron collider physics. *arxiv:hep-ph/0403045v2*, March 2004. 24

[8] S.Moch. Hard qcd at hadron colliders. *arxiv:hep-ph/0803:0457v2*, February 2008. 24, 28, 29

[9] T.Ince. Early standard model measurements with atlas. *ATL-PHYS-PROC-2009-054*, May 2009. 25

[10] T.J.Stelzer M.L.Mangano. Tools for the simulation of hard hadronic collisions. *Annu. Rev. Nucl. Part. Sci.2005.55:555-88*, 2005. 26

[11] P.Skands T.Sjostrand, S.Mrenna. Pythia 6.4 physics and manual. *arxiv:0603175 [hep-ph]*, March 2006. 27, 30

[12] A.D.Polosa M.L.Mangano, F.Piccinini. Alpgen, a generator for hard multiparton processes in hadronic collisions. *arxiv:hep-ph/0206293*, December 2006. 27

[13] BP Kersevan E.Richter-Was. Acermc manual. *arxiv:hep-ph/0201302v2*, June 2002. 27

[14] M.A.Gigg D.Grellscheild K.Hamilton O.Latunde-Dada S.Platzer P.Richardson M.H.Seymour A.Sherstnev J.Tully B.R.Webber M.Bahr, S.Gieske. Herwig++ physics and manual. *arxiv:hep-ph/0803.0883v3*, December 2008. 27, 30

[15] M.H. Seymour J.M. Butterworth, J.R.Forshaw. Multiparton interactions in photoproduction at hera. *arxiv:hep-ph/9601371*. 27

[16] M.Kramer B.Plumper M.Spira P.M.Zerwas W.Beenakker, S.Dittmaier. Higgs radiation off top quarks at the tevatron and the lhc. *arxiv:hep-ph/0107081v1*, July 2001. 27, 28

[17] Particle Data Group. Particle listings. `http://pdg.lbl.gov`, 2009. 28, 47, 65

[18] M. Seymour. Parton shower monte carlo event generators. 29

[19] J.M.Butterworth P.Lenzi. A study on matrix element corrections in inclusive z/$\gamma *$ production at lhc as implemented in pythia, herwig, alpgen and sherpa. *arxiv:hep-ph/0903.3918v3*, March 2009. 30

[20] R.Vilar G.Gomez, T.Rodrigo. Comparison of w/z+jets and w/z+b$\bar{b}$+jets processes for different matrix-element mc generators. *CDF/PHYS/MONTECARLO/PUBLIC/6556*, July 2003. 30

[21] A.Shibata U.Husemann M.Bosman, R.Hawkings. Understanding monte carlo generators for top physics. *ATL-COM-PHYS-2009-334*, September 2009. 30

[22] The ATLAS collaboration A.Tricoli. Underlying event studies at atlas. *ATL-COM-PHYS-2009-149*. 31

[23] W.J.Stirling G.Watt R.S.Thorne, A.D.Martin. Parton distributions and qcd at lhcb. *arxiv:hep-ph/0808.1847v1*, August 2008. 33, 40, 131

[24] Geant 4. 43

[25] E.Richter-Was. Atlfast 2.0. *ATL-PHYS-98-131*, November 1998. 43

[26] The ATLAS Collaboration. Triggering top quark events. *CERN-OPEN-2008-020*, May 2009. 45

[27] The ATLAS Collaboration. Hlt b-tagging performance and strategies. *CERN-OPEN-2008-020*, March 2009. 45

[28] M.Schumacher K.Desch. Model independent determination of the top yukawa coupling from lhc and ilc. *arXiv:0407.159v1 [hep-ph]*, July. 45

[29] ATLAS Collaboration. Physics performance studies and strategy of the electron and photon trigger selection. *arxiv:hep-ph/0901.0512*, September 2008. 46

[30] ATLAS Collaboration. Performance of the muon trigger slice with simulated data. *arxiv:hep-ph/0901.0512*, September 2008. 46

[31] Adam Roe. Top mc: Weighted alpgen samples. `http://twiki.cern.ch/twiki/bin/view/AtlasProtected/WeightedAlpgenSamples`, 2009. 50

[32] ATLAS Collaboration. Cross sections, monte carlo simulations and systematic uncertainties. *arxiv:hep-ph/0901.0512*, September 2008. 63

[33] The CDF Collaboration. First measurements of inclusive w and z cross sections from run ii of the fermilab tevatron collider. *Phys. Rev. Lett. 94, 091803 (2005)*. 63

[34] K.Hatakeyama P.Loch M.Tonennesmann S.D.Ellis, J.Huston. Jet energy scale correction to semileptonic b-jets from missing neutrino energy. *ATLAS-COM-PHYS-2008-086*, June 2008. 66

[35] J. Leveque A.Rozanov J.B. de Vivie S.Correard, V.Kostioukhe. b-tagging with dc1 data. *ATL-PHYS-2004-006*, February 2004. 72, 73

[36] The ATLAS Collaboration. Soft muon tagging. *CERN-OPEN-2008-020*. 74

[37] The D0 Collaboration. Experimental discrimination between charge 2e=3 top quark and charge 4e=3 exotic quark production scenarios. *PRL 98, 041801*, January 2007. 84

[38] J. E. Huth et al. Toward a standardization of jet definitions. *FNAL-C-90-249-E*, July 1990. 91

[39] G. Salam. Towards jetography. *arxiv:0906.1833v1 [hep-ph]*, June 2009. 92, 93

[40] G.Soyez G.Salam. A practical seedless infrared-safe cone jet algorithm. *arXiv:0704.0292v2 [hep-ph]*, April. 92, 93

[41] G.Soyez M.Cacciari, G.P.Salam. The anti-kt jet clustering algorithm. *arxiv:0802.1189 [hep-ph]*, 2008. 93

[42] M.H.Seymour B.R.Weber S.Catani, Y.L.Dokshitzer. Longitudinally invariant k(t) clustering algorithms for hadron hadron collisions. *Nucl.Phys.B 406,187*, 1993. 93

[43] G. Salam M. Wobisch et al. C. Buttar, M. Kramer. Standard model handles and candles working group: Tools and jets summary report. *arxiv:0803.0678v1 [hep-ph]*, March 2008. 93

[44] S.Dean C.Bernius. Overlap removal between irreducible and reducible ttbar background monte carlo samples for the semileptonic ttbarh0(h0-¿bbbar) channel. 107

[45] A.Tricoli. Underlying event studies at atlas. *ATLAS-PHYS-PROC-2009-048*, May 2009. 131

[46] M.Spannowsky T.Plehn, G.Salam. Fat jets for a light higgs. *arxiv:0910.5472v1 [hep-ph]*. 132

[47] Martin Goebel. Global fits of the electroweak standard model and beyond with gfitter. *arXiv:0905.2488v2 [hep-ph]*, March. 134